CL-Windcon

Closed Loop Wind Farm Control

DELIVERABLE REPORT

Testing in the wind tunnel
of wind turbine controllers

Deliverable No.	D3.4	Work Package No.	WP3	Tasks No.	3.2
Work Package Title	Demonstration and Validation of Prototypes				
Linked Tasks Title	Demonstration by wind tunnel testing				
Status	**Final**				
Dissemination level	**public**				
Due date deliverable	2018-10-31	Submission date			2018-10-31
Deliverable version	1.0				

DOCUMENT CONTRIBUTORS

Deliverable responsible	POLIMI
Contributor	**Organization**
Stefano Cacciola	POLIMI
Paolo Schito	POLIMI
Alessandro Croce	POLIMI
Filippo Campagnolo	TUM
Marta Bertelé	TUM
Johannes Schreiber	TUM
Joeri Frederik	TU Delft
Jan-Willem van Wingerden	TU Delft

Reviewer	Organization
Stoyan Kanev	ECN
Iker Elorza	IK4

CONTENTS

LIST OF FIGURES

LIST OF TABLES

1   EXECUTIVE SUMMARY

This deliverable describes the first activities related to the wind tunnel testing campaigns executed in the Politecnico di Milano wind tunnel within the CL-Windcon project. In the first two years of experimentation, different tasks have been performed with the goal of providing the project partners, and the international wind energy community, valuable experimental data obtained while performing a variety of activities related to the testing of wind turbine controllers and their supporting technologies.

It is worth mentioning that the following tests were all accomplished in the first 27 days of wind tunnel experimentation:

- Characterization of the flow within the wake shed by a single wind turbine, as well as within the wake shed by a cluster of two wind turbines, under a wide range of environmental and wind turbine operational conditions. The goal of this activity was to provide valuable measurements to validate wake models characterized by different level of fidelity and complexity.

- Evaluation of the effectiveness of different wind turbine controls on the wake behavior and the evaluation of the performances of ancillary wind farm control techniques, like inflow observers and wake impingement detectors.

- An important set of testings was accomplished with the goal of accurately mapping the inflow within the empty test section of the wind tunnel, in order to improve the knowledge of the actual inflow conditions acting on the turbine models, to be used, for example, in CFD simulations.

This document reports a detailed description of the performed tests, whereas the measurement data are stored and updated in the CL-Windcon web-repositories *ftp://files.cener.com/Windtunnel/*. A selection of some prominent results achieved is also reported in this deliverable with the aim of demonstrating the goodness of the wind tunnel experimentation as a means for analyzing wind farm control related problems.

2   INTRODUCTION

The study of the flow within a wind farm necessitates the comprehension of complex physical phe-
nomena, which often depend on a large number of parameters, related to both atmospheric and
turbine quantities. When it come to considering wind farm control, such this need is even more
pronounced and requires the knowledge about the modifications of the flow as function of specific
wind turbine actions/controls.

Clearly, in the synthesis of wind farm controllers, engineers may rely on different mathematical mod-
els of different complexity and accuracy, which range from simplified wake models to more complex
Computational Fluid Dynamics (CFD) simulations. Such these models may serve as reference tools
to design the controllers and test them in different scenarios.

In this framework, however, there are many points in which the wind tunnel experimentation can
play an essential part. At first, no matter of the complexity, all mathematical models are based on
a set of parameters which should be calibrated so as to ensure the best possible fidelity between
simulation and reality. Such calibration requires an amount of repeatable data at turbine and flow
level, which is typically difficult to have from field experimentation. The quantity and the quality of
measurements achievable in a wind tunnel, along with the possibility to repeat a single experiment
in a controlled environment whose boundary conditions are well-known, renders the wind tunnel ex-
perimentation extremely valuable to generate data to be used for calibrating mathematical models.
Secondarily, in a preliminary stage, testing in a real environment a wind farm control algorithm may
be difficult due to the fact that simply the wind is not controllable nor repeatable, and, therefore,
one should have to wait for the desired atmospheric conditions to perform a test.

In this scenario, the wind tunnel experimentation offers the possibility to overcome such issues and
can be viewed as the perfect segue from simulation to real field environment.

Within the CL-Windcon project, the present deliverable is a part of WP3 "Demonstration and valida-
tion of prototypes" and, specifically, task 3.2 "Demonstration by wind tunnel testing", which deals
with wind tunnel experimentation. Task 3.2 is divided into three subtasks, 3.2.1 "Definition of testing
conditions and test preparation", 3.2.2 "Testing in the wind tunnel of wind turbine controller" and
3.2.3 "Testing in the wind tunnel of integrated wind turbine/wind farm controller". The present de-
liverable describes the activity performed within subtask 3.2.2. Figure 1 illustrates schematically the
connections within work package 3, among tasks, subtasks and deliverables.

Goal of this deliverable is to describe the wind tunnel testing activities of the first 27 days of experi-
mentation. The experimental data are available on the web-repository *ftp://files.cener.com/Windtunnel/*.

The deliverable is organizing according to the following plan.

Chapter 3 is devoted to the wind tunnel flow characterization. In particular, the measurements of
the actual flow within the wind tunnel without the turbines are presented, with special emphasis on
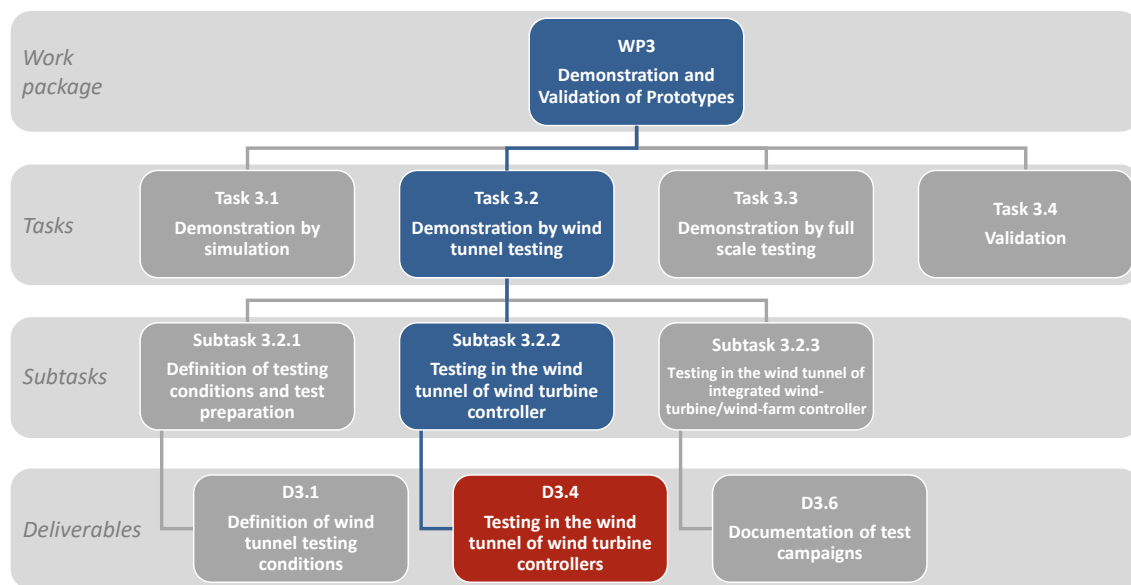
Figure 1. Map WP/Task/Subtask/Deliverable

three dimensional velocity and turbulence intensity measurements, in different locations within the wind tunnel test chamber.

Chapter 4 is devoted to the characterization of the wake of the wind turbine models. Different scenarios, in terms of wind speed, yaw misalignment and atmospheric boundary conditions are investigated. Additionally, the interaction between wakes shed by two different turbines are also studied.

In Chapter 5, the effects of individual pitch control (IPC) on loads and wake characteristics are evaluated.

In Chapter 6, the effectiveness of an inline wake state update method are considered. With "wake state update method" is meant an algorithm able to identify some parameters of a simplified wake model from experimental data. Such algorithm can be performed recursively, during a wind farm operative condition, or as a batch process, after the end of the experimentation, being the former of a paramount importance for wind farm control applications.

A testing activity on a fast wake recovery technique is presented in Chapter 7. With "fast wake recovery technique" is meant a particular turbine control aimed at increasing the energy level inside the wake with the main effect of reducing its speed loss and propagation length.

Chapter 8 deals with the validation of a wind state observer, able to estimate from blade loads the inflow conditions in terms of horizontal misalignment (or yaw misalignment), vertical misalignment (or upflow angle) and both vertical and horizontal shear layer.

Finally, Chapter 9 summarizes the main findings and completes the deliverable with remarks and outlook.

3   WIND TUNNEL FLOW CHARACTERISTICS

The reproduction of wind tunnel conditions for the numerical simulation of wind turbines relies on the correct reproduction of the wind tunnel flow conditions. An experimental campaign aiming at recording the wind tunnel flow has been extensively carried out at Politecnico di Milano wind tunnel. The information of the actual wind tunnel flow allows a better understanding of the interaction between the wind turbine and the wind, as well as the analysis of the wakes of the wind turbines. Possible non-uniformities of the flow are measured and may be used for the correction of the experimental data.

Flow measurement have been performed using two three-components hot wires, using a sampling frequency of 2kHz for 40 seconds. Spacing between the anemometers is fixed to $250mm$, and the complete wind tunnel section is mapped with a spacing of $250mm$ in both the horizontal and vertical direction. All wind tunnel information and experimental setup are reported in *Deliverable Report 3.1 - (Definition of wind tunnel testing conditions)*. A description of the position of the mapped sections is reported in Figure 2.

The flow is mapped at the wind tunnel inlet, and at some distance upwind the wind turbines (i.e. 4 diameter and 12 diameter upstream). This information may be used to correct the numerical simulation results or to postprocess the experimental wake data. In order to have also the information of the flow on the rotorplane the flow measurement has been performed following the rotor wake mapping, by measuring the wind speed on a horizontal and a vertical line passing through the hub on the rotorplane.

The data are recorded, postprocessed and made available to the partners according to what reported in *Deliverable Report 3.1 - (Definition of wind tunnel testing conditions)*. The data are formatted as Matlab files (*.mat extension) in the form of structure. The data are stored on the storage made available for CL-Windcon project at *ftp://files.cener.com*. The wind tunnel inflow data are available at: *.../Windtunnel/INFLOW Mapping/*. In this folder, 17 files contain the data and are named as follows:

- $INLET$ - stands for the mapping of the inlet section;

- $4D$ - stands for the mapping of the section 4 rotor diameter upwind the first turbine;

- $12D$ - stands for the mapping of the section 12 rotor diameter upwind the first turbine;

- LT - stands for the offshore / low turbulence wind condition;

- HT - stands for the onshore / high turbulence wind condition;

- $modelX$ - stands for the mapping of the flow on the rotor plane for turbine n. X.
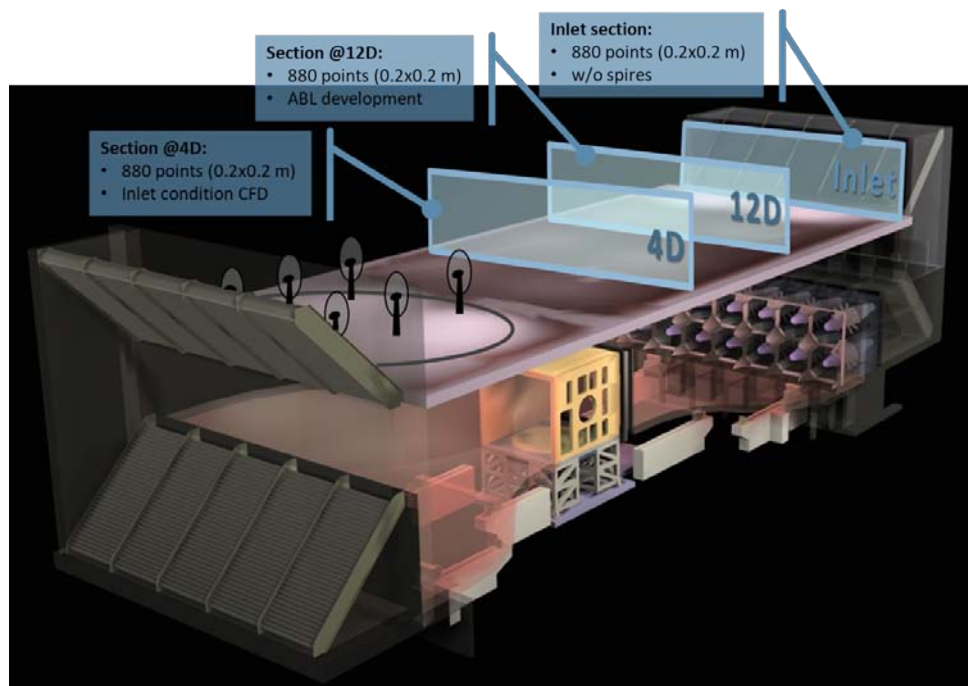
Figure 2. Wind tunnel setup for inflow mapping.

3.1   Inlet mapping

The inlet section of the wind tunnel has been mapped in order to describe possible flow non-uniformities. In Figure 4 the mean flow characteristics are reported.

The mean axial velocity shows some flow non-uniformity to be imputed to the wind tunnel structure: the map is done very close to the beginning of the test section, and it is possible to notice the presence of the wake of the heat exchanger supports. On the transversal and lateral wind component nothing significant is noticeable, unless some possible lateral and vertical components of wind speed mainly imputable to the positioning of the traversing system used for the measurement of the wind speed.

The same conclusion may be inferred in Figure 5, where the average flow presents a low turbulence intensity, that increases in the wake of the wind tunnel structure.

3.2   High Turbulence - Onshore conditions

Wind speed for the onshore - high turbulent wind condition is reported in the following figures. Looking to the section $12D$ upstream the first turbine, the axial mean flow shows the vertical velocity profile, while some differences in mean speed are visible along the transversal coordinates (Figure 6). This may be imputed to the presence of spires at the inlet of the tunnel section, which may affect the mean flow. The higher wind speed is present between above 1 and 3.5 m and decreases above. The boundary layer develops not only on the lower part of the wind tunnel, but also on the roof (but
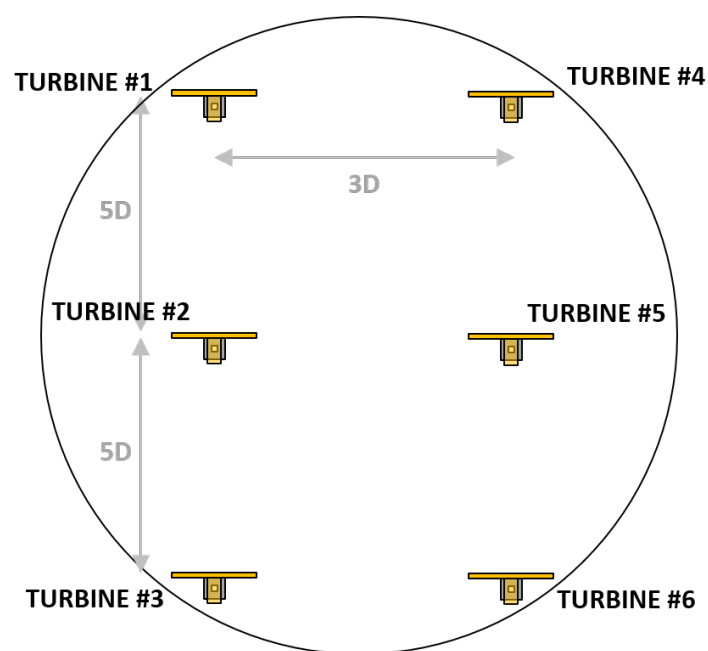
Figure 3. Wind turbine position during wind tunnel tests. The wind blows from the top.

with different gradient). The Turbulence intensity content is higher on the lower part of the section for all components of the velocity due to the presence of spires and floor roughness, while it reduces with height (Figure 7).

When approaching the wind turbines (i.e. looking to the maps performed $4D$ upstream the first wind turbine), the velocity gradient appear smoother and more even along the test section, even if some small differences still appear in both the mean components (Figure 8) and turbulent components (Figure 9).

The flow conditions on the turbine rotorplanes are reported from Figure 10 to Figure 15. Vertical mean wind profile (Figure 10(a)) and turbulence intensity (Figure 10(b)) on turbine n. 1 show very well the incoming flow conditions. Horizontal mean wind profiles show a small non uniformity along the transversal direction (Figure 10(c)) and on turbulence intensity (Figure 10(c)) that may be imputed to the presence of the spires at the inlet of the test section. Non-uniformity of the mean flow is in the order of 10%, while turbulence intensity values are between 11% and 13%.

Going downstream on turbine n. 2 (Figure 11) and turbine n. 3 (Figure 12) the same consideration may be found. The only major difference is in the turbulence intensity on turbine n. 3 that decays (Figure 12(b)-(d)), since the floor roughness is not present any more, and the turbulence content decays moving downstream.

For turbine n. 4 (Figure 13), turbine n. 5 (Figure 14), turbine n. 6 (Figure 15) the same considerations performed for the other row of rotorplanes are valid.

3.3   Low Turbulence - Offshore conditions

Wind speed for the offshore - low turbulent wind condition is reported in the following figures. Looking to the section $12D$ upstream the first turbine, the axial mean flow shows the vertical velocity profile, while some differences in mean speed are visible along the transversal coordinates (Figure 16). This may be imputed to the presence of spires at the inlet of the tunnel section which are clearly visible, which may affect the mean flow. The higher wind speed is present between between 1 and 3.5 m and decreases above. The boundary layer develops not only on the lower part of the wind tunnel, but also on the roof (but with different gradient). In the upper map it is still possible to see the wake of the wind tunnel heat exchanger structure, especially on the upper part, where lower turbulence intensity mixes the flow. The Turbulence intensity content is higher on the lower part of the section for all components of the velocity due to the presence of spires and floor roughness, while it reduces with height (Figure 17).

When approaching the wind turbines (i.e. looking to the maps performed $4D$ upstream the first wind turbine), the velocity gradient appear smoother and more even along the test section, even if some small differences still appear in both the mean components (Figure 18) and turbulent components (Figure 19). The wake of the heat exchanger structure is still visible.

The flow conditions on the turbine rotorplanes are reported from Figure 20 to Figure 25. Vertical mean wind profile (Figure 20(a)) and turbulence intensity (Figure 20(b)) on turbine n. 1 show very well the incoming flow conditions. Horizontal mean wind profiles show a small non uniformity along the transversal direction (Figure 20(c)) and on turbulence intensity (Figure 20(c)) that may be imputed to the presence of the spires at the inlet of the test section. Non-uniformity of the mean flow is in the order of 5%, while turbulence intensity values are between 6% and 4.5%.

Going downstream on turbine n. 2 (Figure 21) and turbine n. 3 (Figure 22) the same consideration may be found. In this case, there is no floor roughness along the tunnel, therefore the turbulence intensity decay between the rotorplanes is limited.

For turbine n. 4 (Figure 23), turbine n. 5 (Figure 24), turbine n. 6 (Figure 25) the same considerations performed for the other row of rotorplanes are valid.
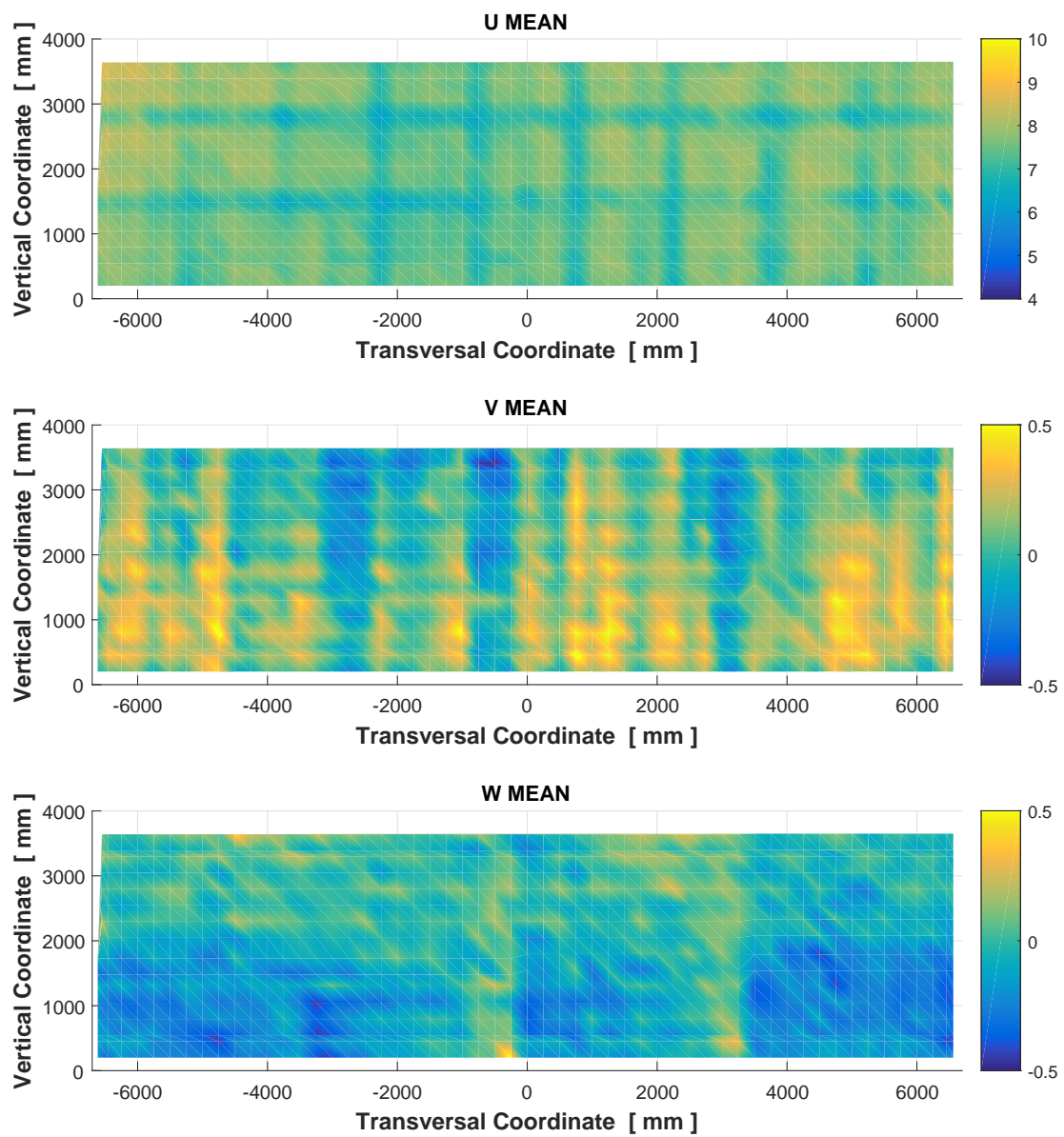
Figure 4. Mean flow velocity at wind tunnel test section inlet.
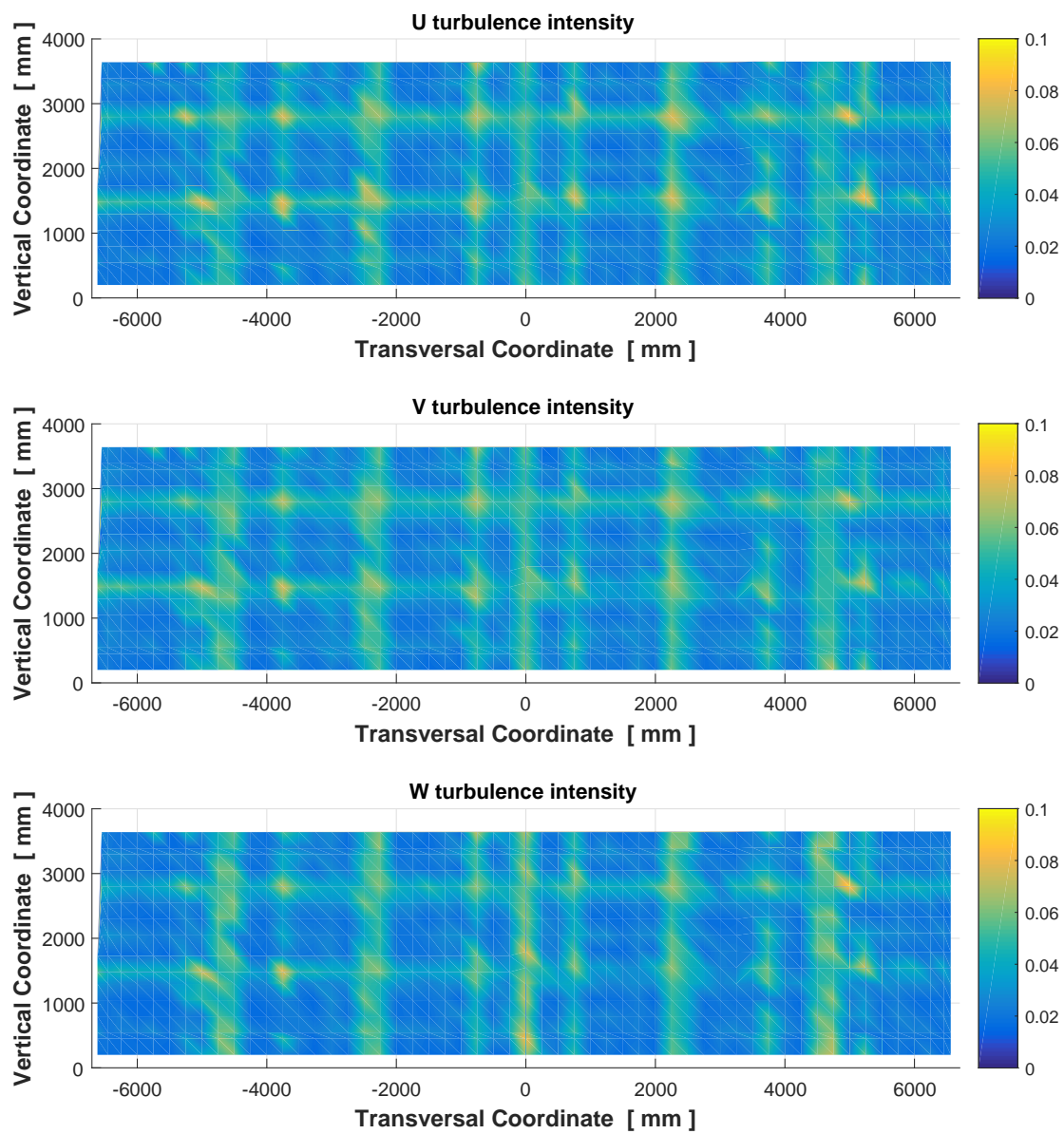
Figure 5. Turbulence intensity of the flow at wind tunnel test section inlet.
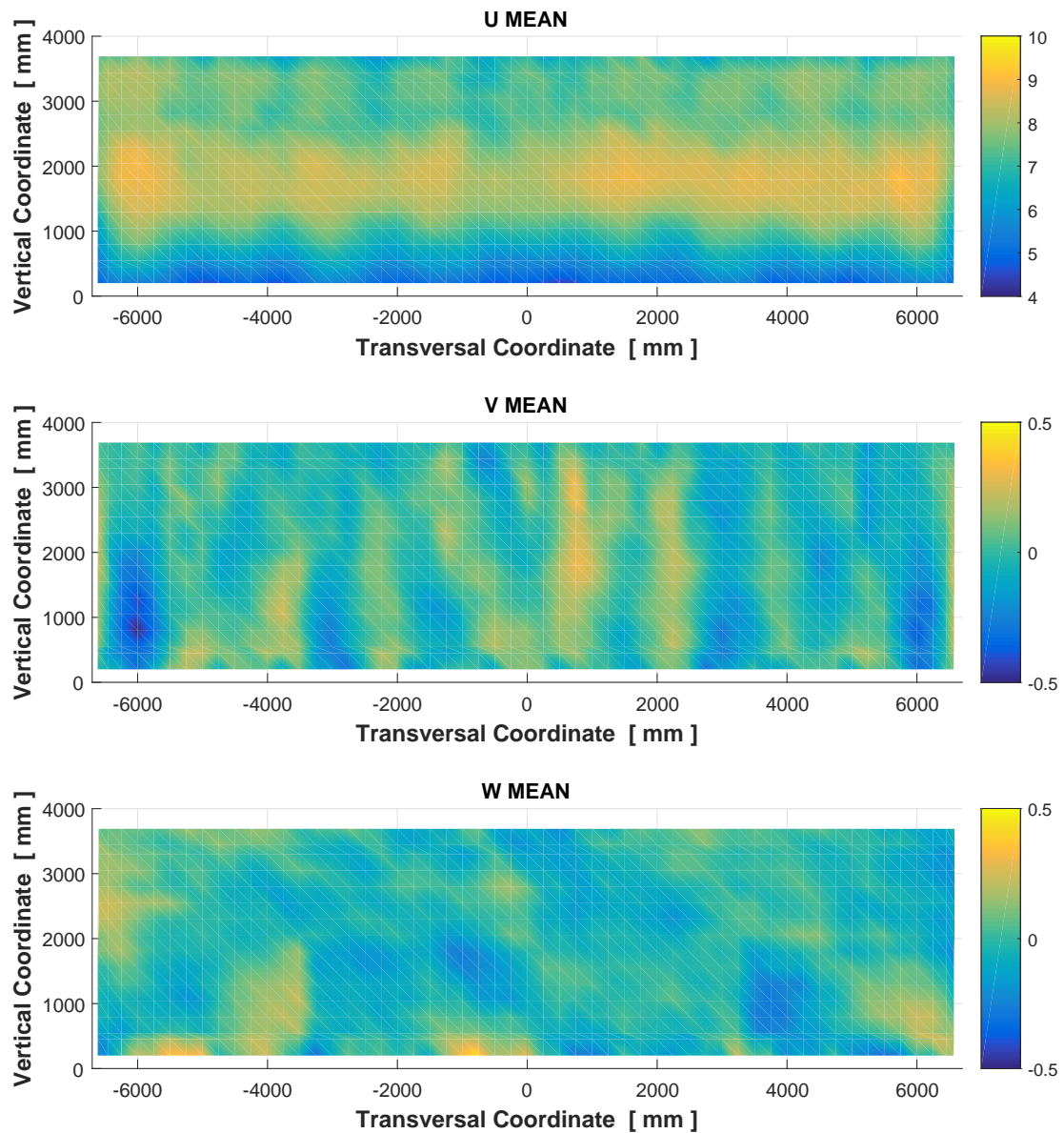
Figure 6. Mean flow velocity of wind tunnel test section for on-shore (high turbulence) condition at 12 diameters upstream.
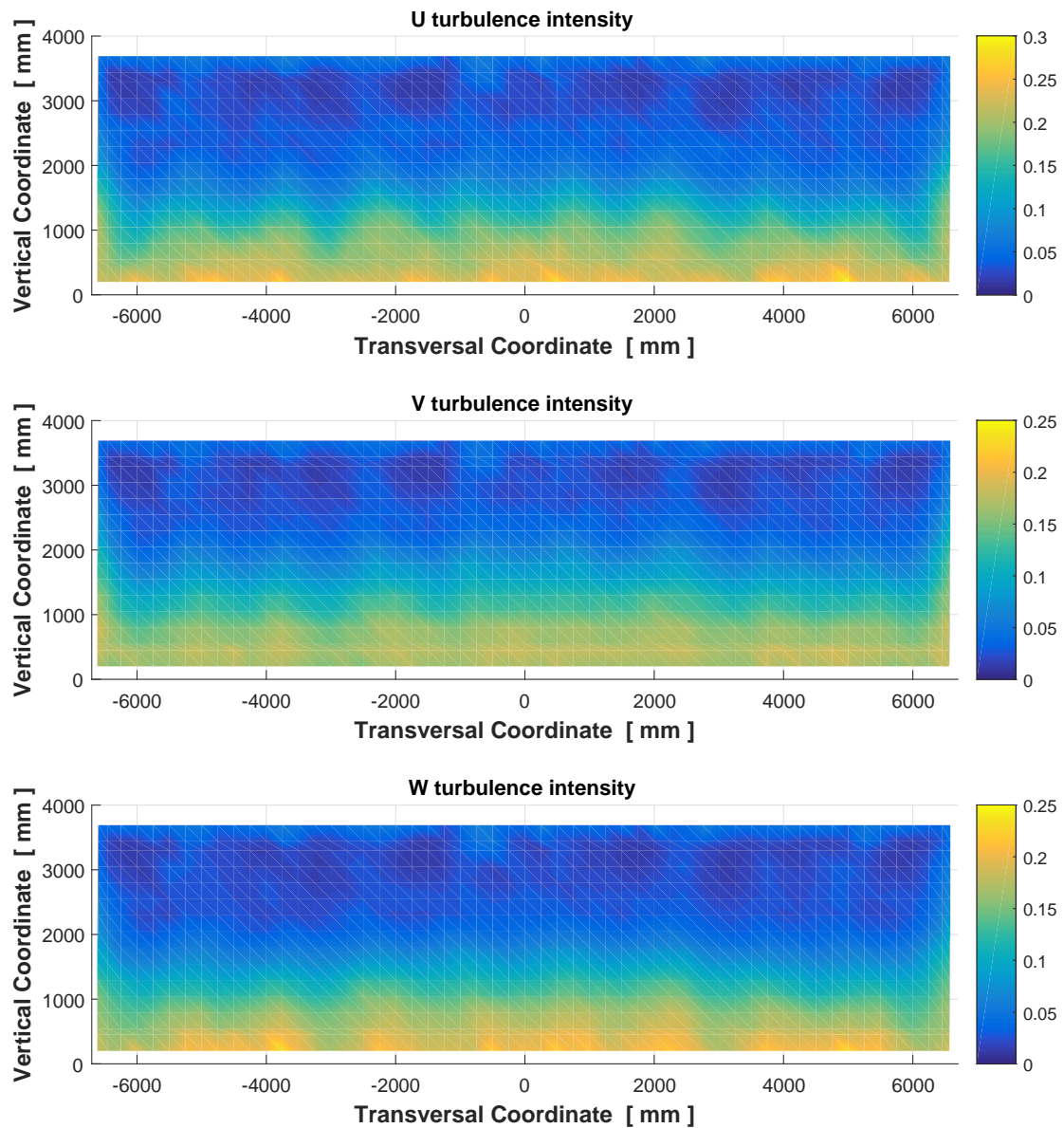
Figure 7. Turbulence intensity of the flow for onshore (high turbulence) condition at 12 diameters upstream.
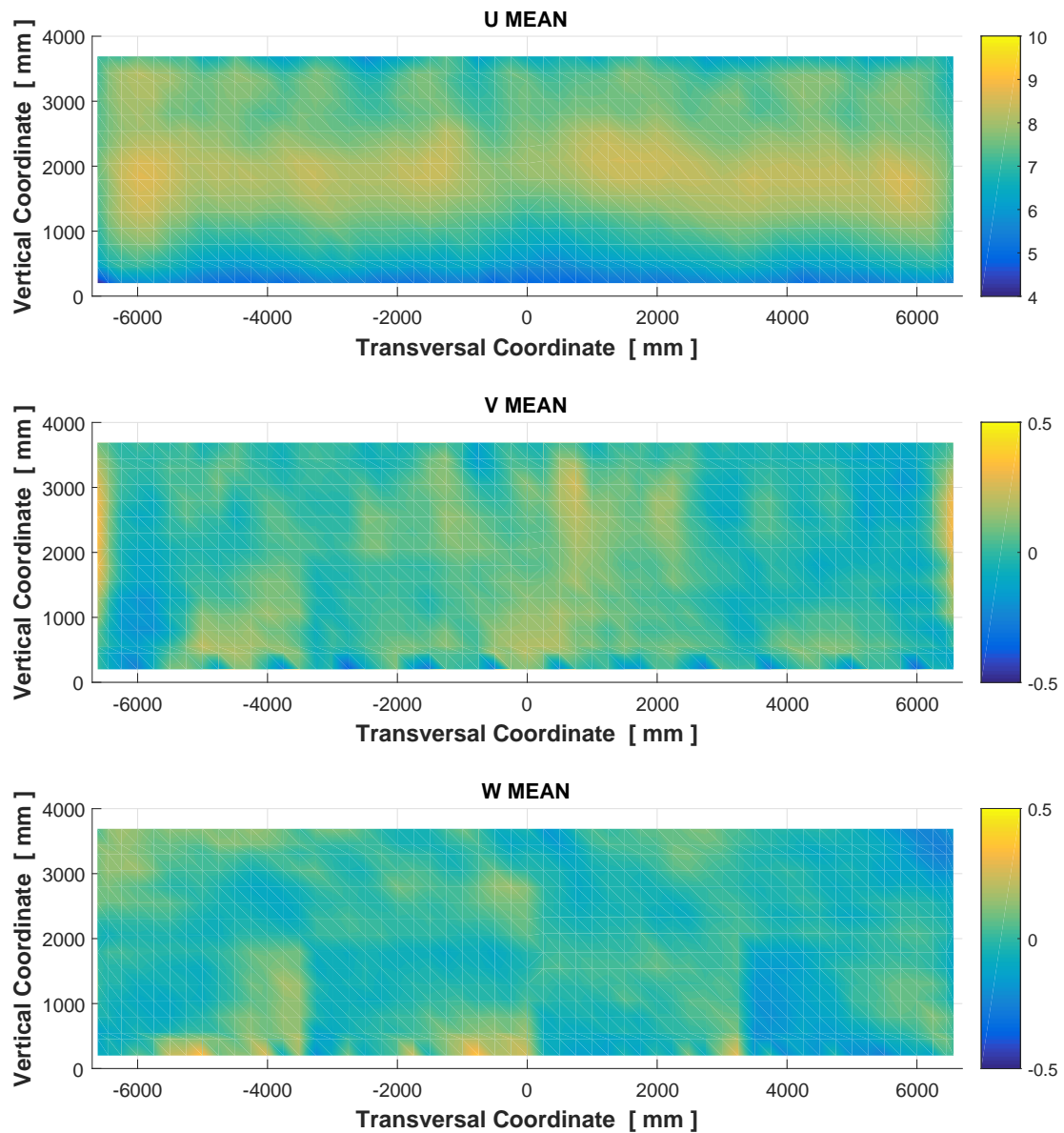
Figure 8. Mean flow velocity of wind tunnel test section for on-shore (high turbulence) condition at 4 diameters upstream.
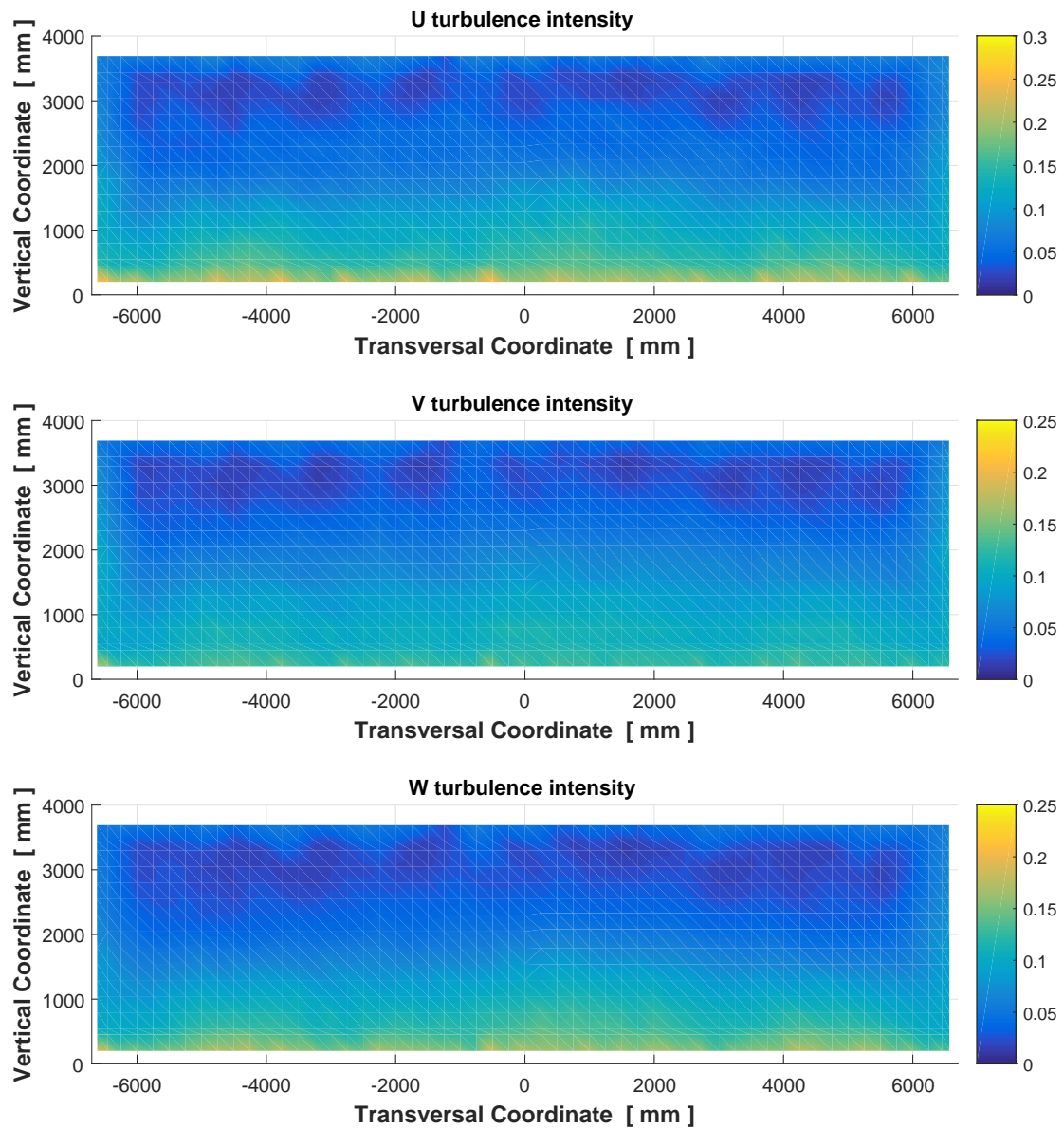
Figure 9. Turbulence intensity of the flow for onshore (high turbulence) condition at 4 diameters upstream.
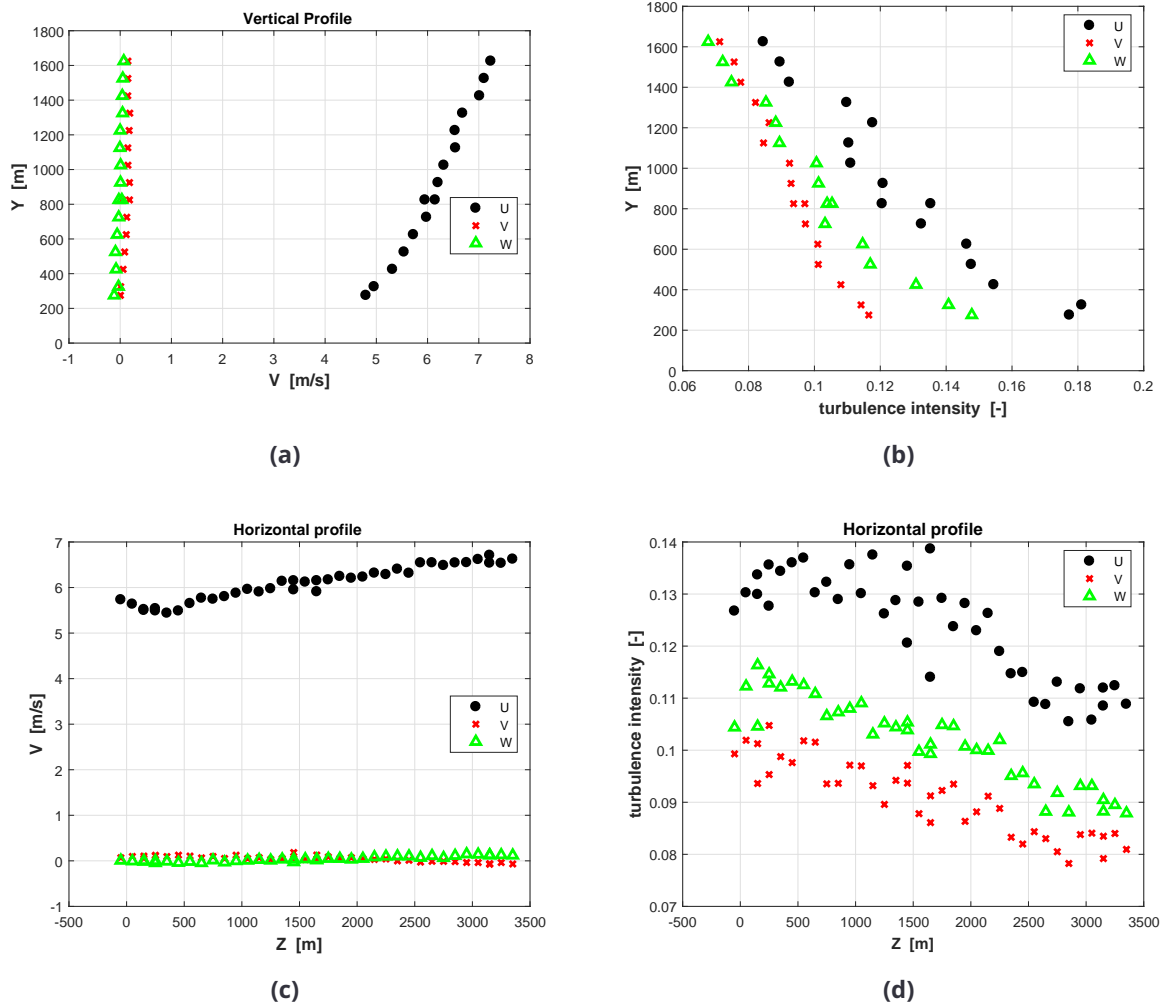
Figure 10. Mean flow characteristics for onshore (high turbulence) condition at wind turbine location nr 1. (a) vertical profile of mean wind, (b) vertical profile of turbulence intensity, (c) horizontal profile of mean wind at hub height, (d) horizontal profile of turbulence intensity at hub height.
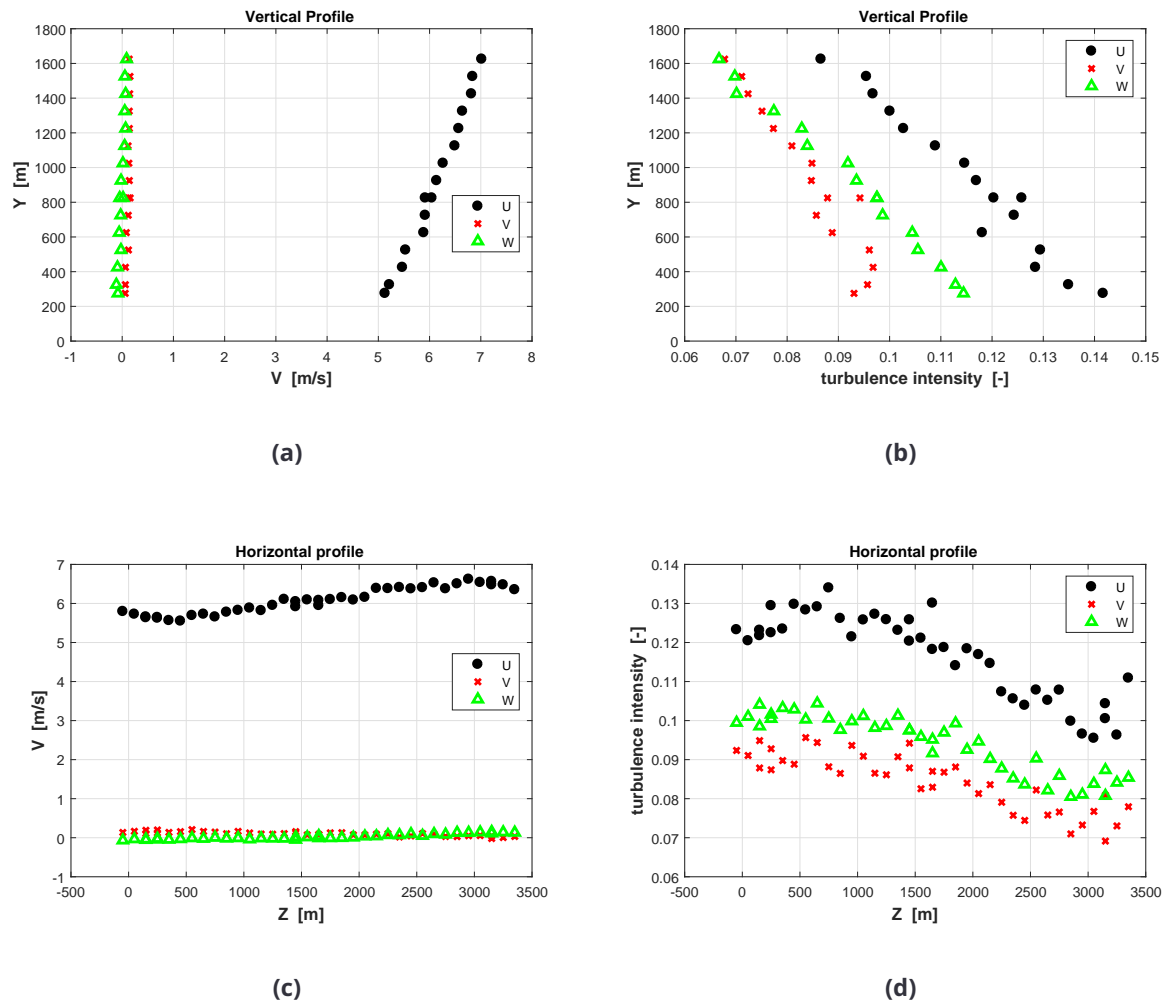
Figure 11. Mean flow characteristics for onshore (high turbulence) condition at wind turbine location nr 2. (a) vertical profile of mean wind, (b) vertical profile of turbulence intensity, (c) horizontal profile of mean wind at hub height, (d) horizontal profile of turbulence intensity at hub height.
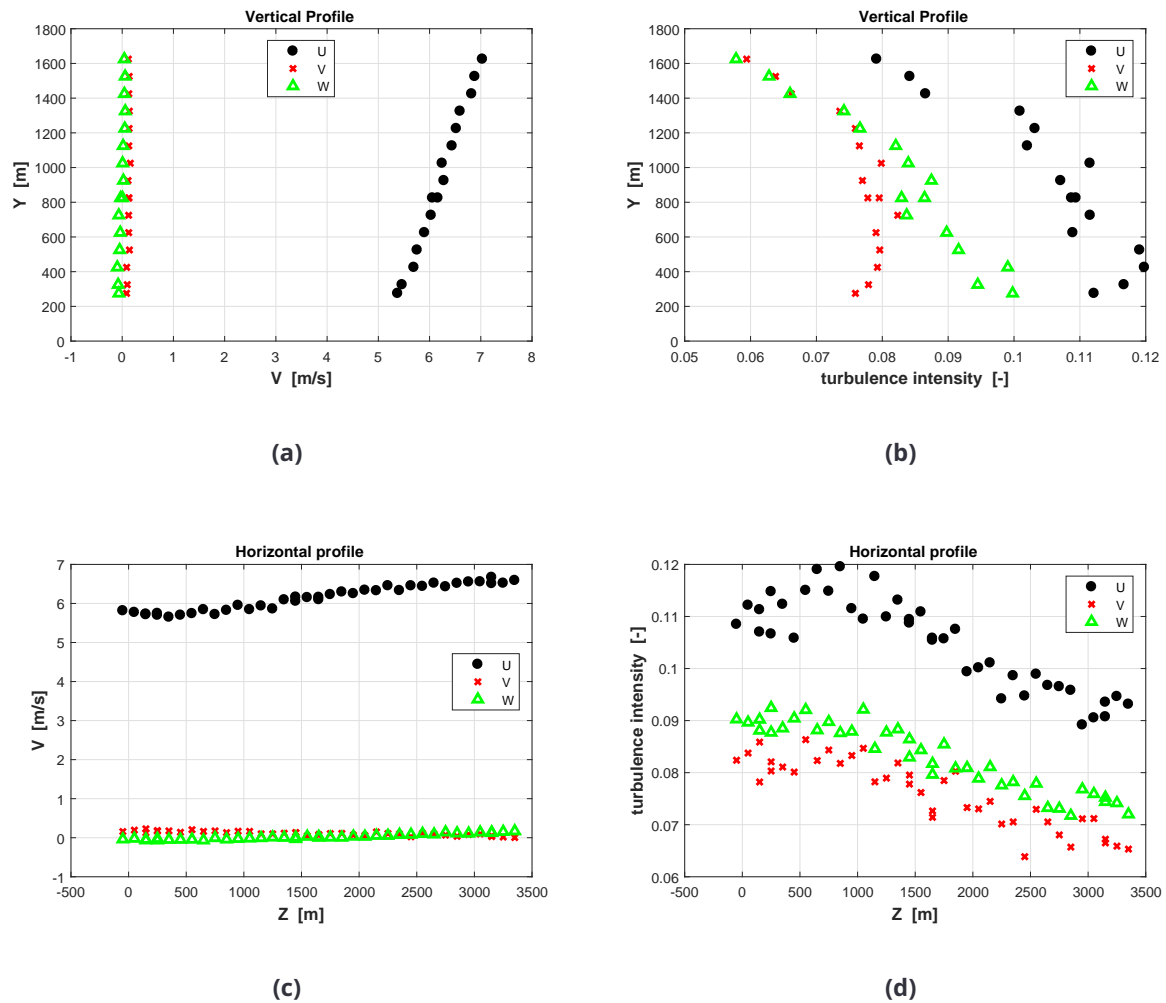
Figure 12. Mean flow characteristics for onshore (high turbulence) condition at wind turbine location nr 3. (a) vertical profile of mean wind, (b) vertical profile of turbulence intensity, (c) horizontal profile of mean wind at hub height, (d) horizontal profile of turbulence intensity at hub height.
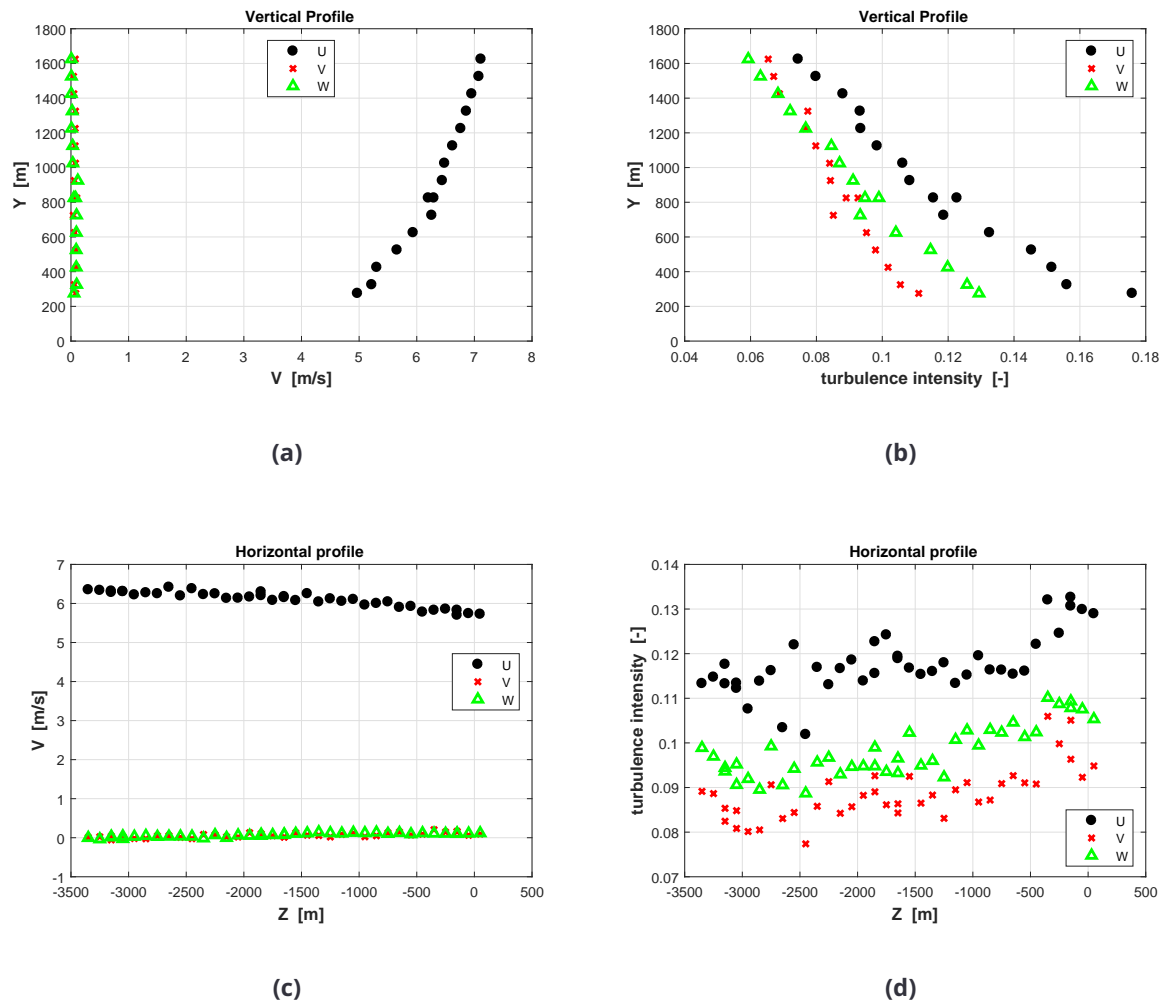
Figure 13. Mean flow characteristics for onshore (high turbulence) condition at wind turbine location nr 4. (a) vertical profile of mean wind, (b) vertical profile of turbulence intensity, (c) horizontal profile of mean wind at hub height, (d) horizontal profile of turbulence intensity at hub height.
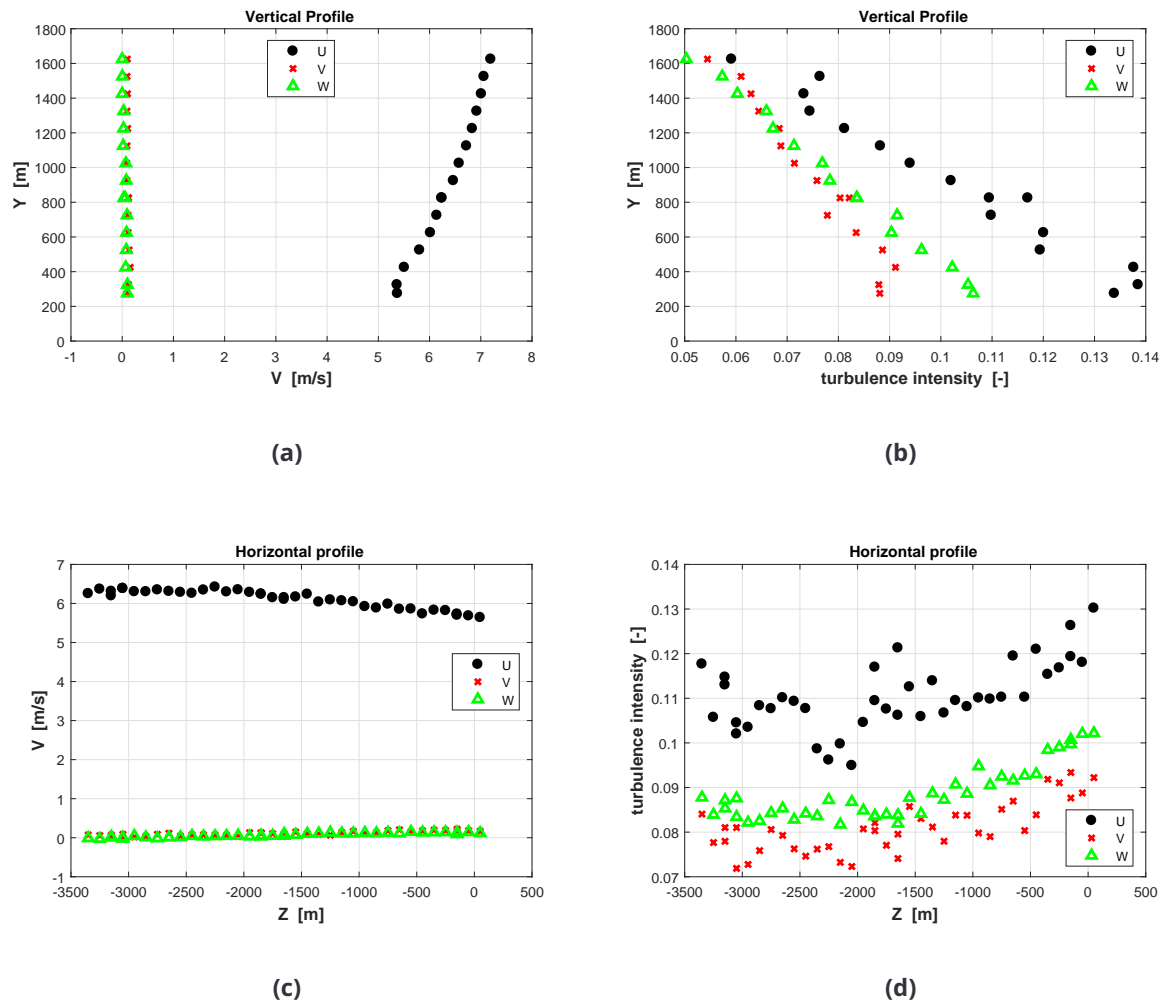
Figure 14. Mean flow characteristics for onshore (high turbulence) condition at wind turbine location nr 5. (a) vertical profile of mean wind, (b) vertical profile of turbulence intensity, (c) horizontal profile of mean wind at hub height, (d) horizontal profile of turbulence intensity at hub height.
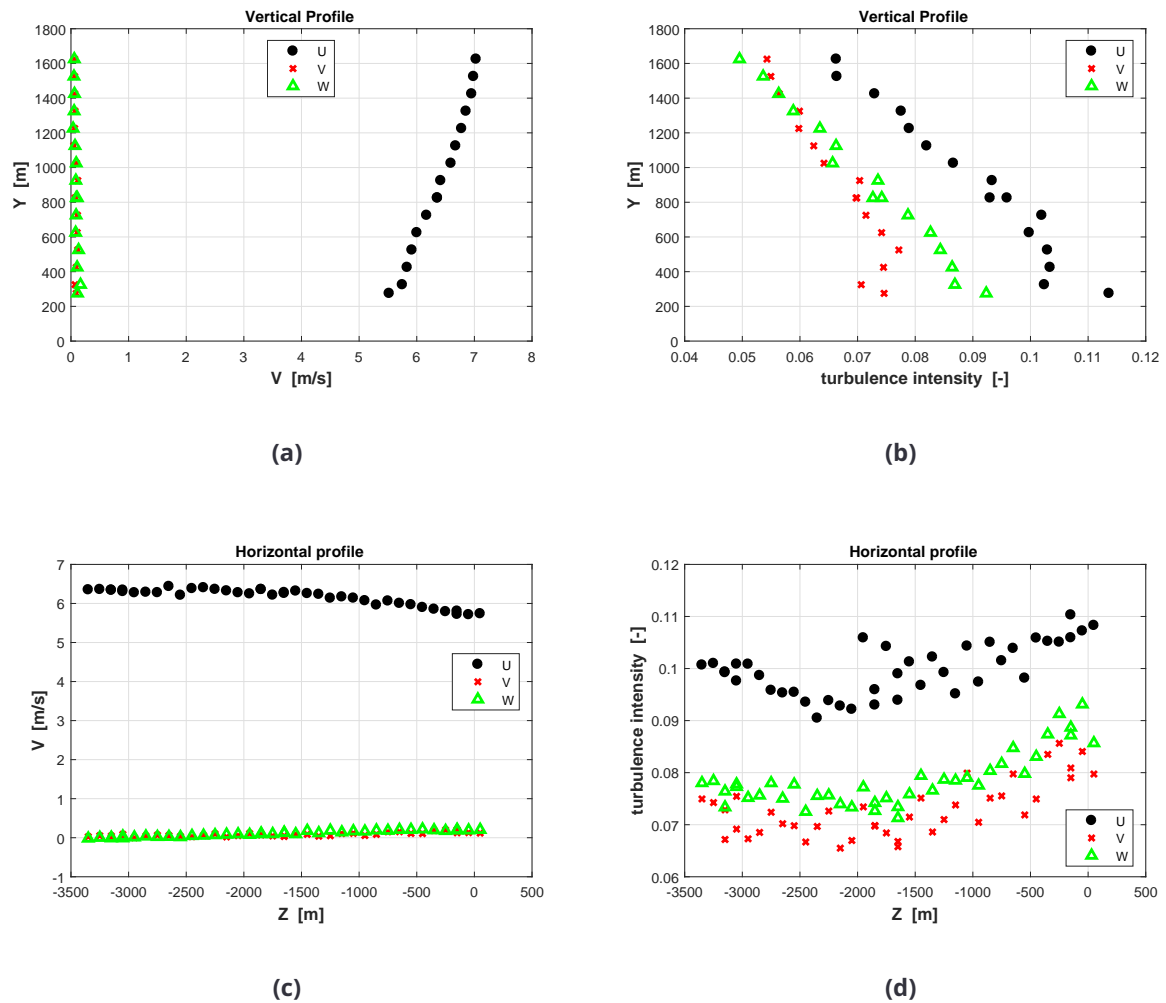
Figure 15. Mean flow characteristics for onshore (high turbulence) condition at wind turbine location nr 6. (a) vertical profile of mean wind, (b) vertical profile of turbulence intensity, (c) horizontal profile of mean wind at hub height, (d) horizontal profile of turbulence intensity at hub height.
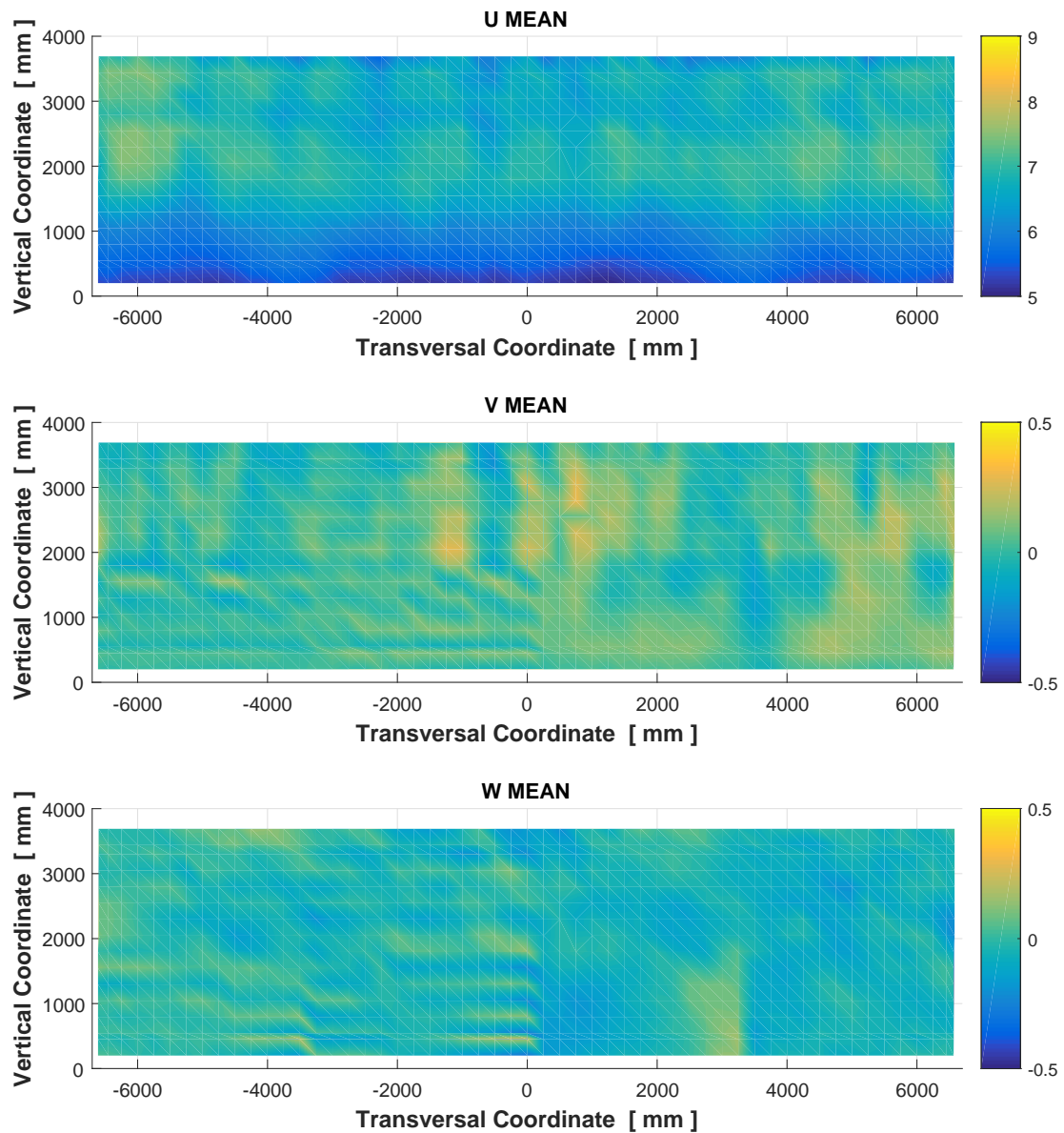
**Figure 16. Mean flow velocity of wind tunnel test section for off-
shore (low turbulence) condition at 12 diameters upstream.**
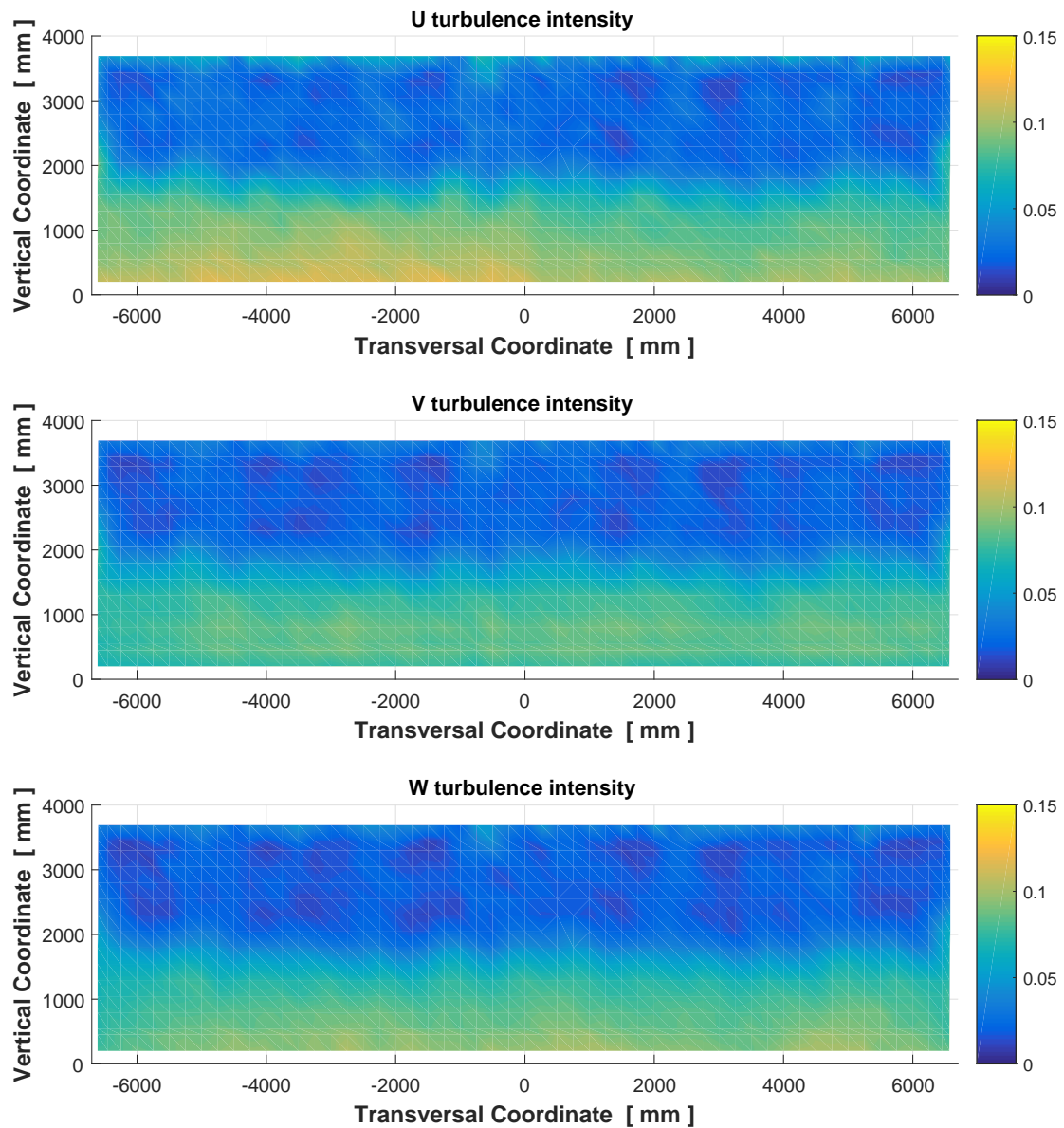
**Figure 17. Turbulence intensity of the flow for offshore
(low turbulence) condition at 12 diameters upstream.**
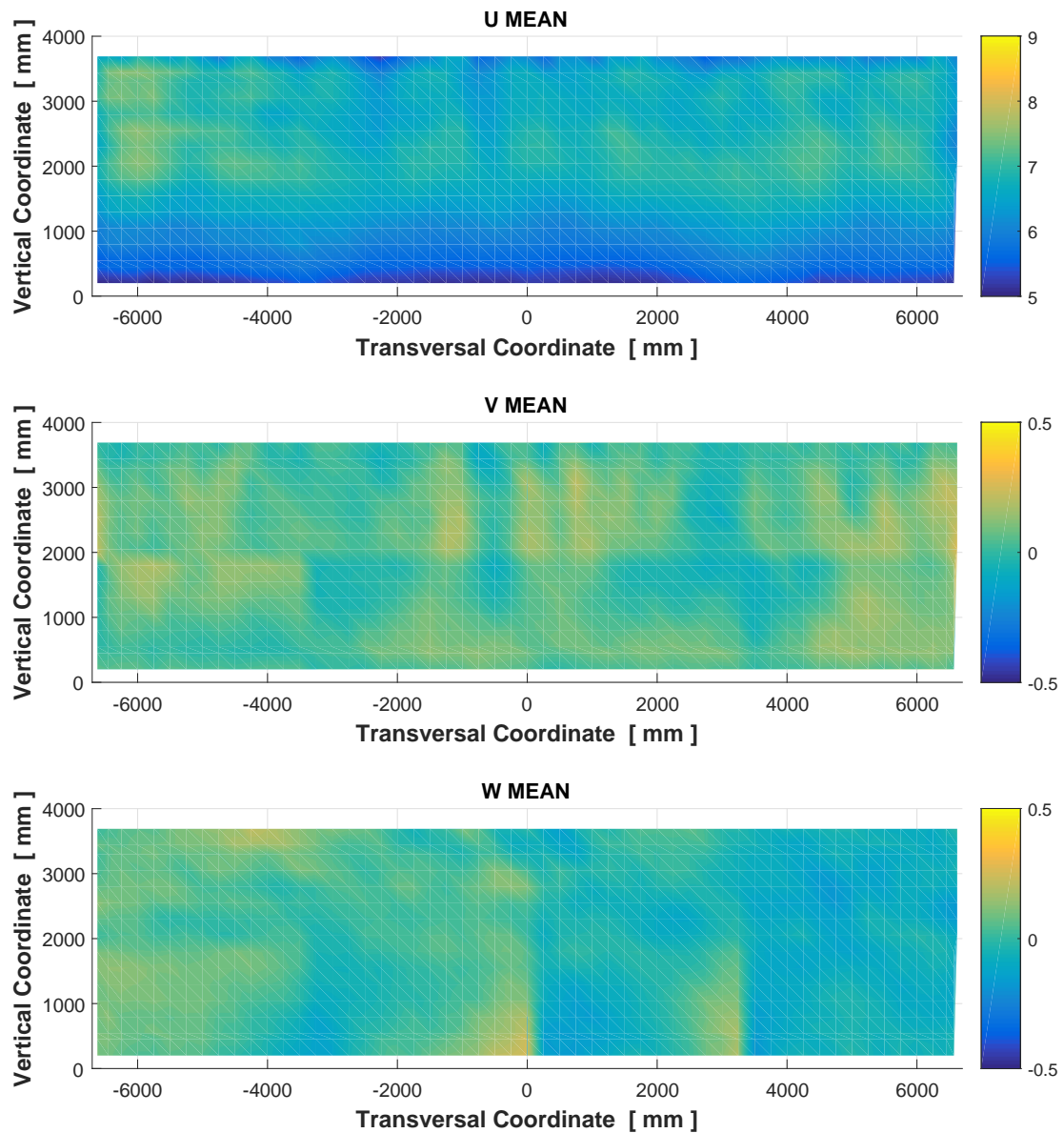
Figure 18. Mean flow velocity of wind tunnel test section for off-shore (low turbulence) condition at 4 diameters upstream.
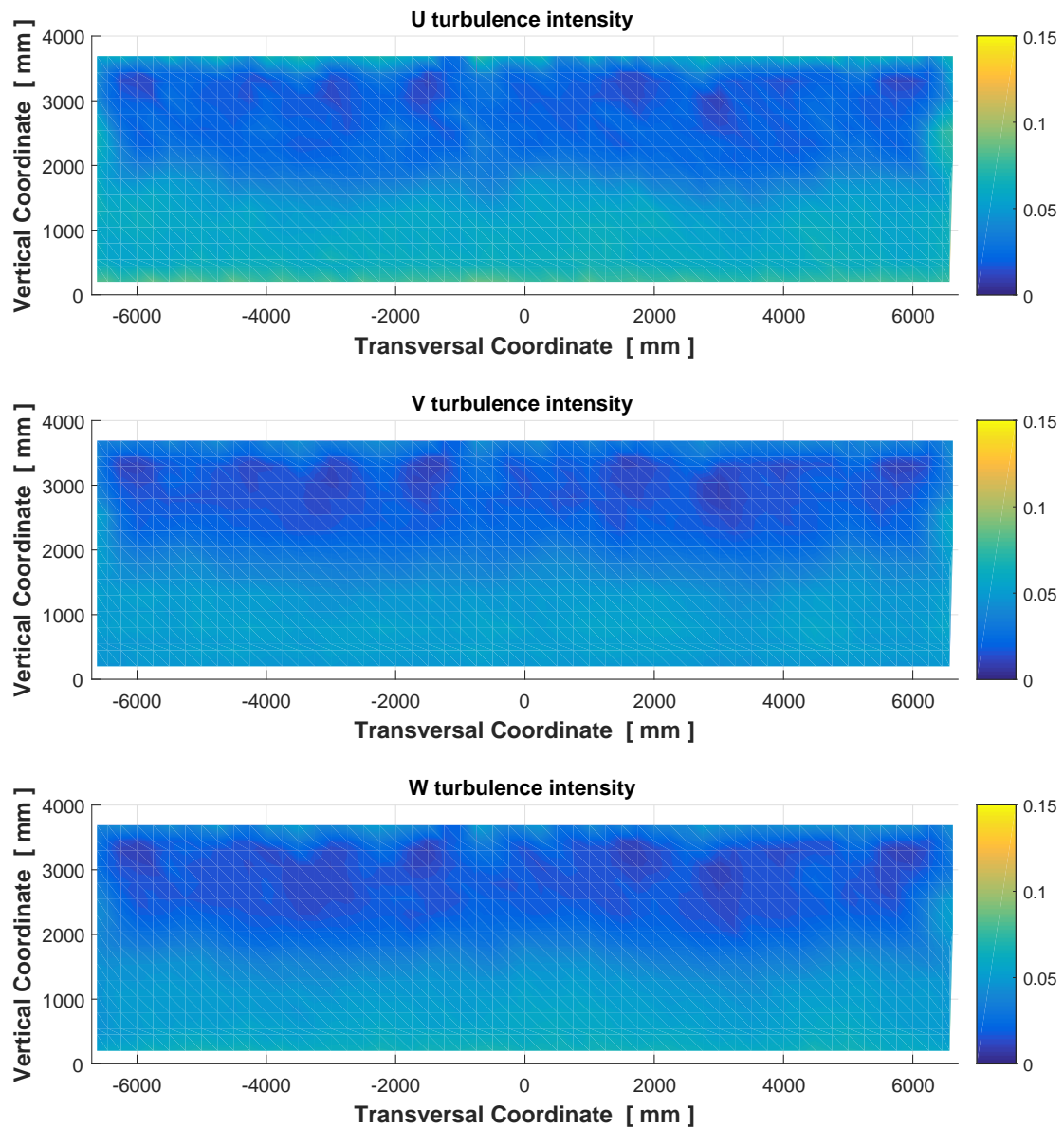
**Figure 19. Turbulence intensity of the flow for offshore
(low turbulence) condition at 4 diameters upstream.**
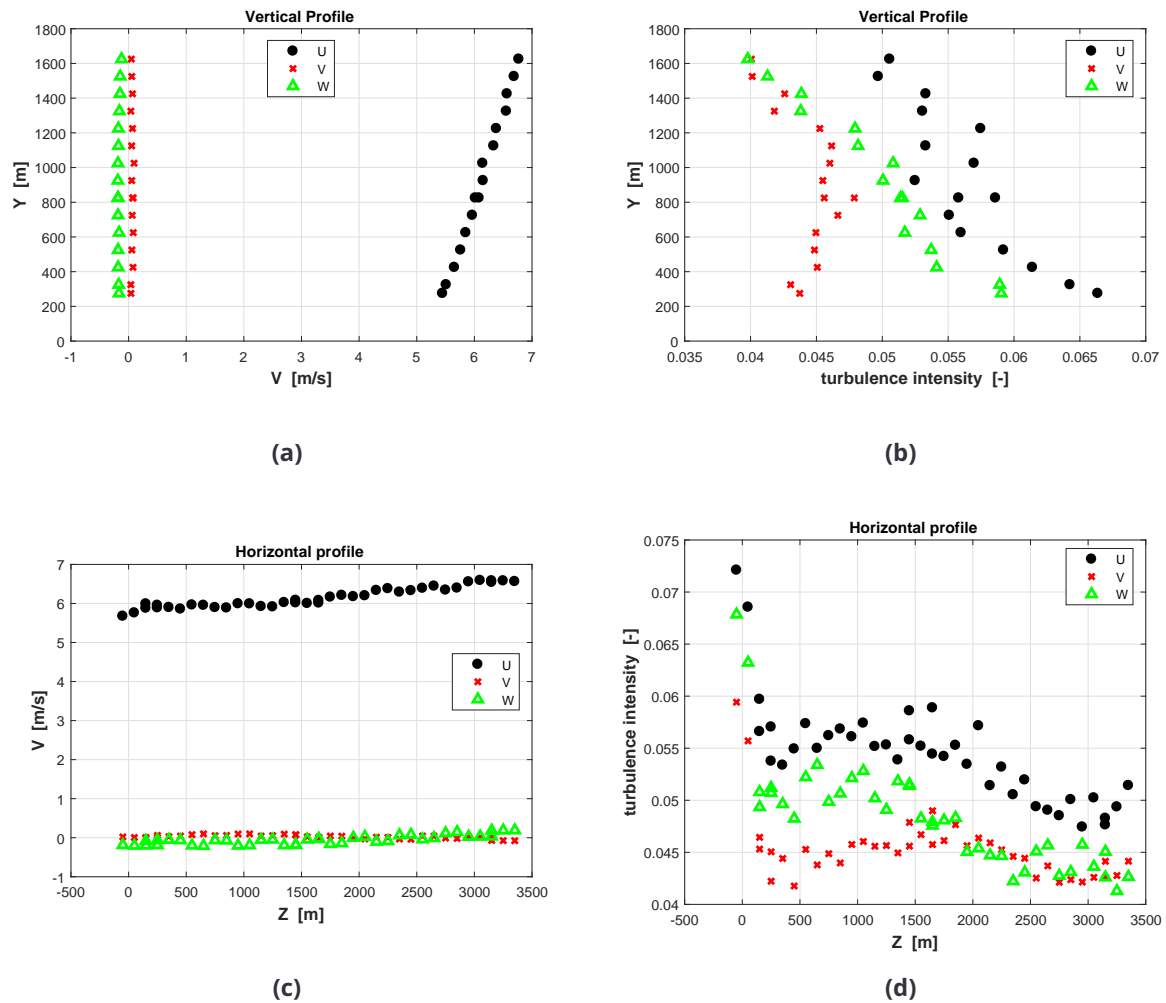
Figure 20. Mean flow characteristics for offshore (low turbulence) condition at wind turbine location nr 1. (a) vertical profile of mean wind, (b) vertical profile of turbulence intensity, (c) horizontal profile of mean wind at hub height, (d) horizontal profile of turbulence intensity at hub height.
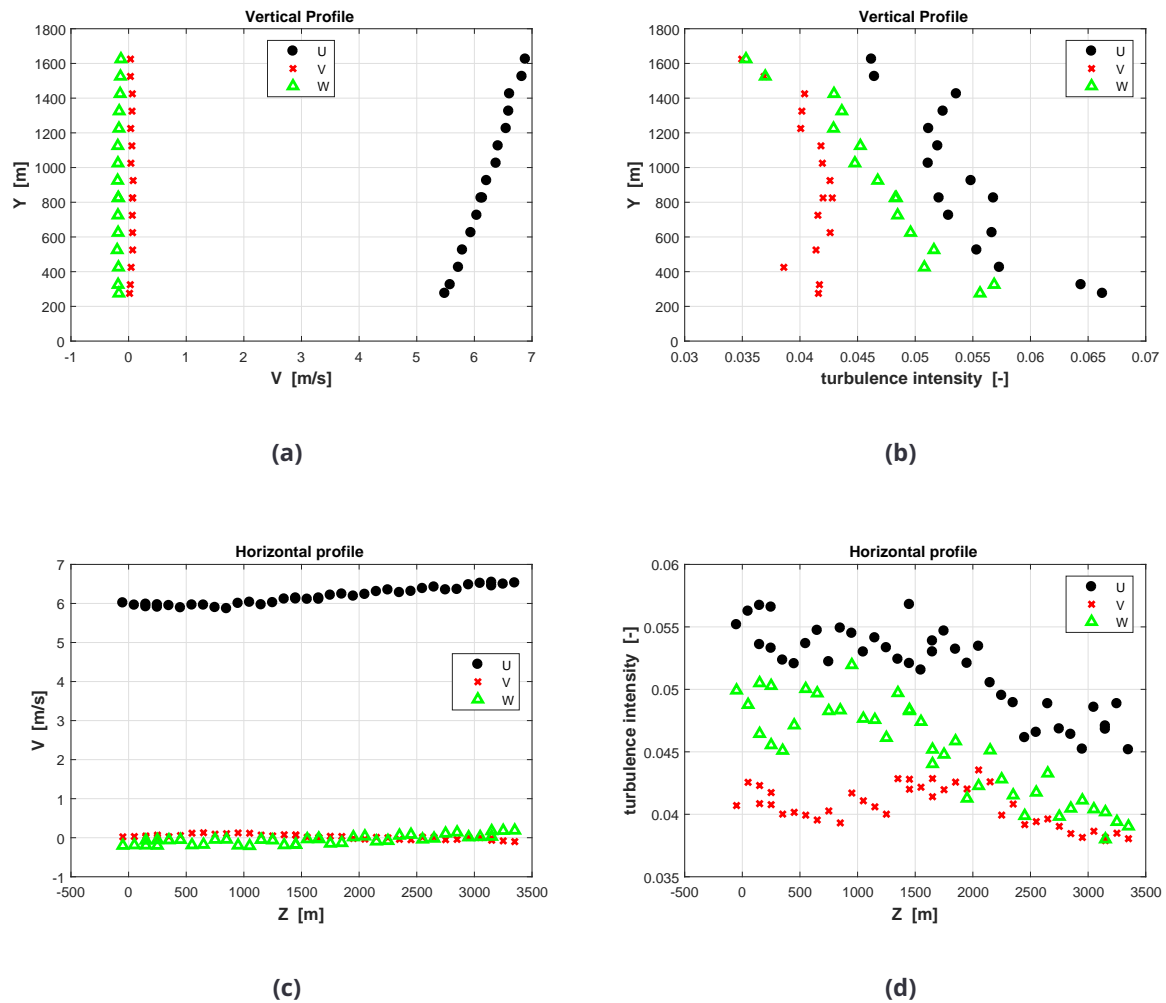
Figure 21. Mean flow characteristics for offshore (low turbulence) condition at wind turbine location nr 2. (a) vertical profile of mean wind, (b) vertical profile of turbulence intensity, (c) horizontal profile of mean wind at hub height, (d) horizontal profile of turbulence intensity at hub height.
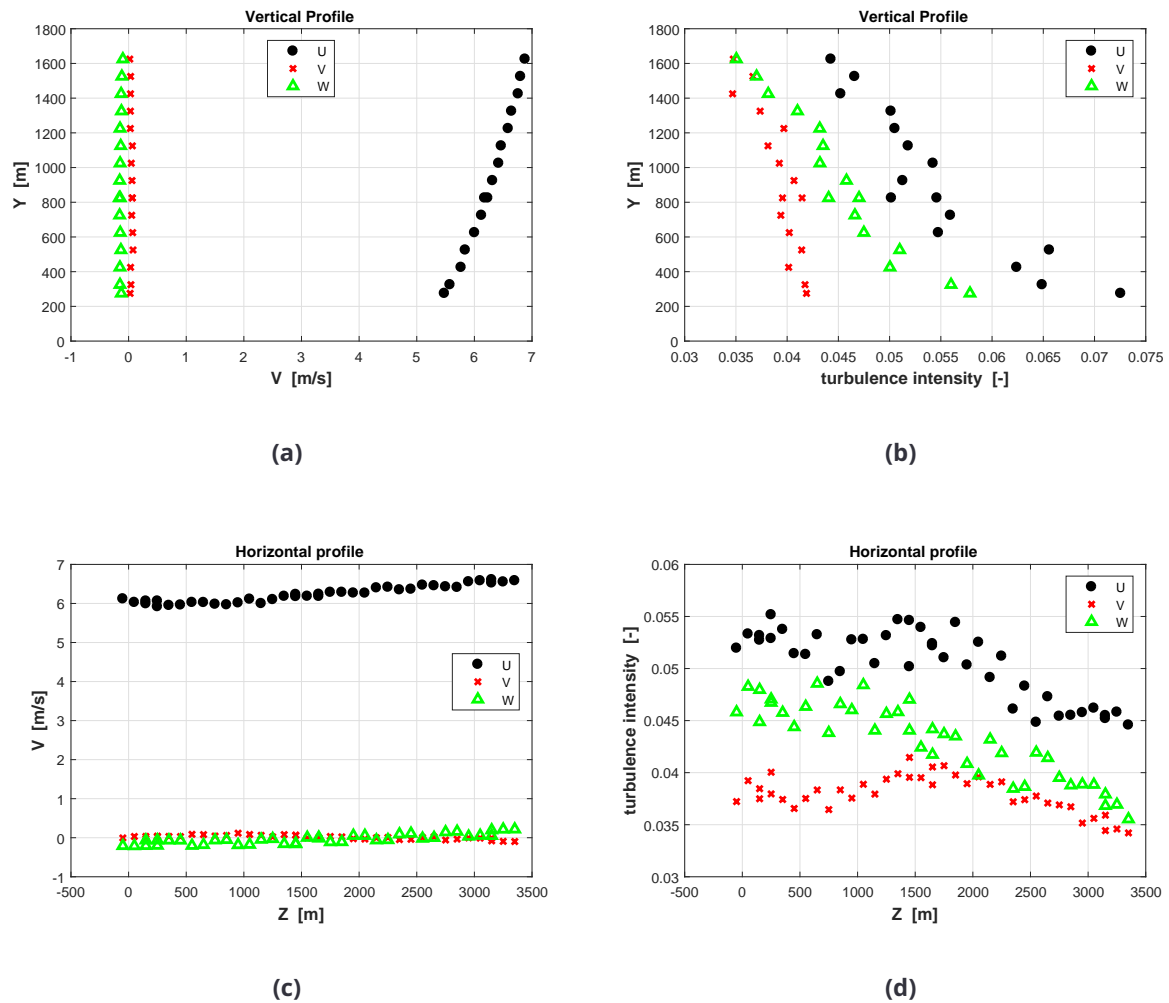
Figure 22. Mean flow characteristics for offshore (low turbulence) condition at wind turbine location nr 3. (a) vertical profile of mean wind, (b) vertical profile of turbulence intensity, (c) horizontal profile of mean wind at hub height, (d) horizontal profile of turbulence intensity at hub height.
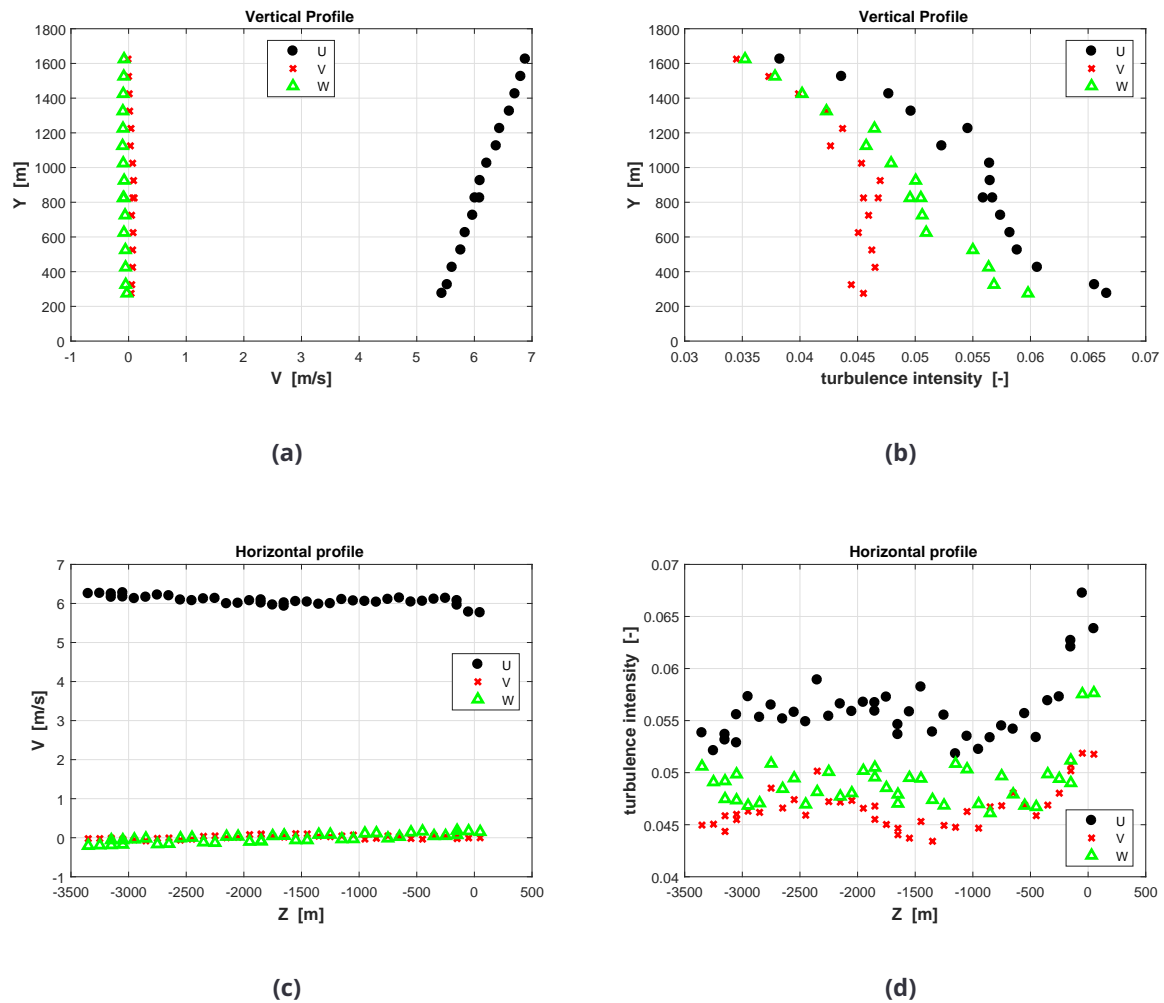
Figure 23. Mean flow characteristics for offshore (low turbulence) condition at wind turbine location nr 4. (a) vertical profile of mean wind, (b) vertical profile of turbulence intensity, (c) horizontal profile of mean wind at hub height, (d) horizontal profile of turbulence intensity at hub height.
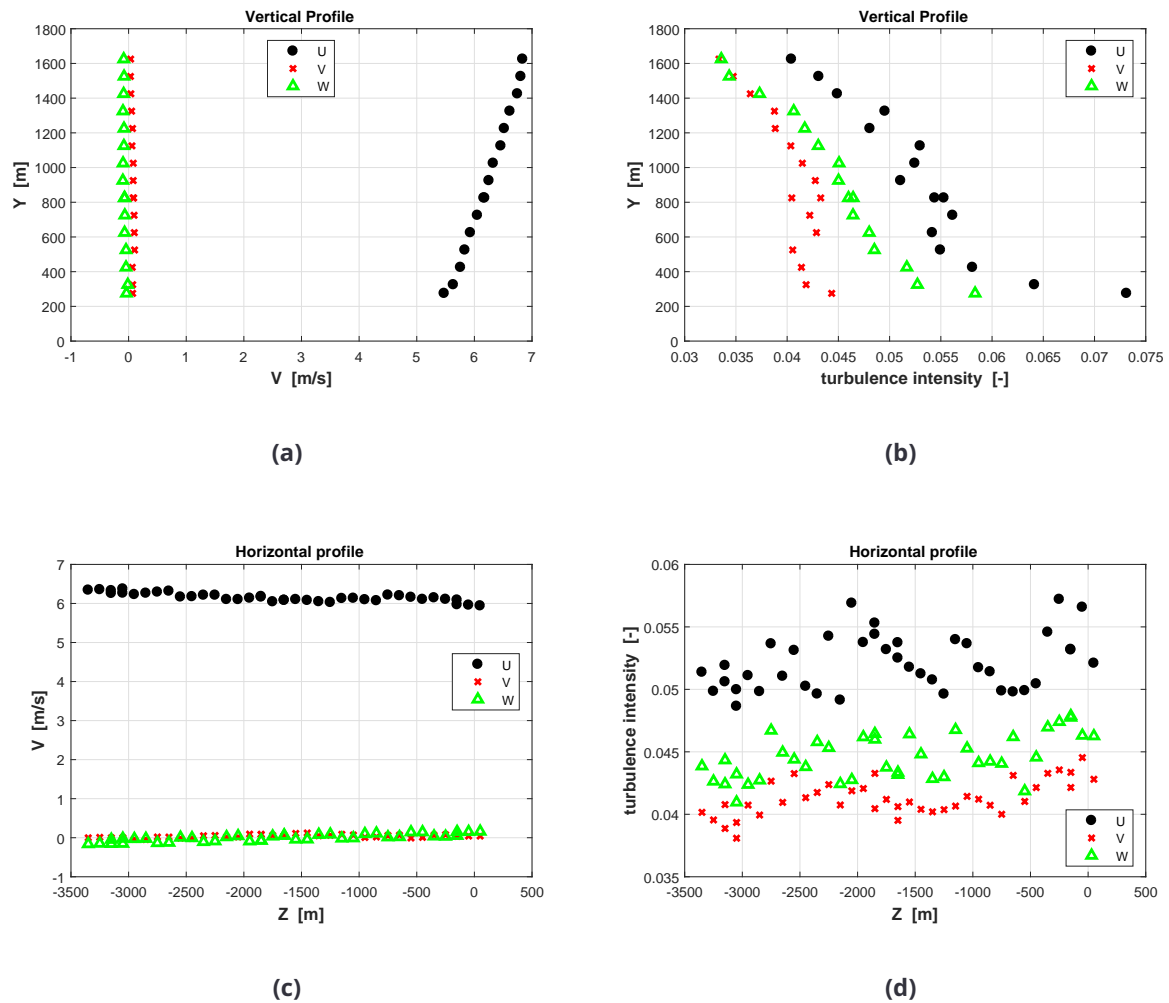
Figure 24. Mean flow characteristics for offshore (low turbulence) condition at wind turbine location nr 5. (a) vertical profile of mean wind, (b) vertical profile of turbulence intensity, (c) horizontal profile of mean wind at hub height, (d) horizontal profile of turbulence intensity at hub height.
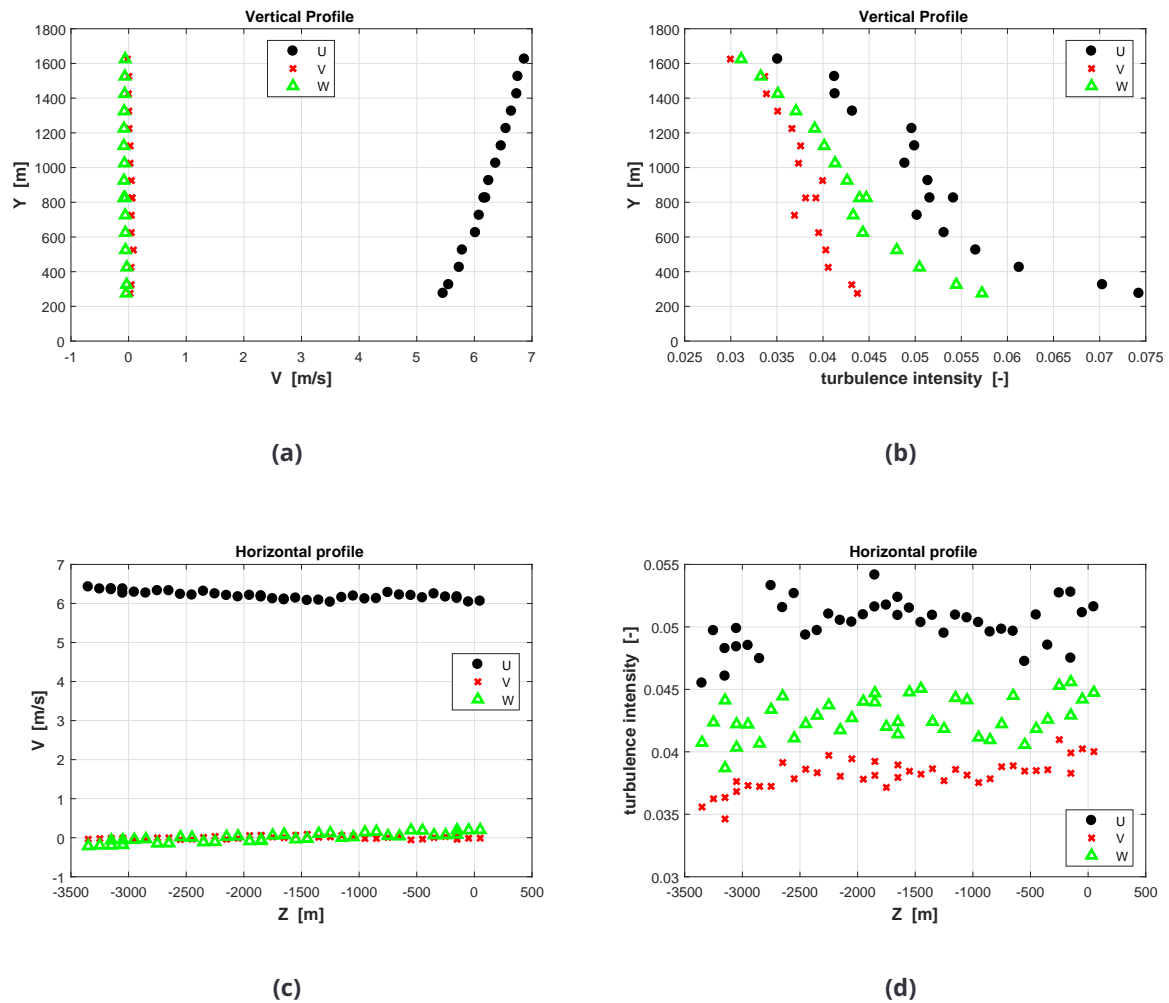
Figure 25. Mean flow characteristics for offshore (low turbulence) condition at wind turbine location nr 6. (a) vertical profile of mean wind, (b) vertical profile of turbulence intensity, (c) horizontal profile of mean wind at hub height, (d) horizontal profile of turbulence intensity at hub height.

4   SINGLE AND MULTIPLE WAKE CHARACTERIZATION

4.1   Introduction

Approaches for wake control try to influence the energy content of the wake or attempt to control its path. Given the complexity of the problem of controlling wakes, there is a need for a thorough understanding of the physics and for the validation and verification of simulation models. To this aim, the use of actively controlled scaled wind turbine models tested in a wind tunnel can provide remarkable experimental data. Indeed, the experiments in the wind tunnel can be conducted with with a better control and knowledge of the boundary and operating conditions than it is usually possible in the field, and at lower costs and risks. Therefore, although wind tunnel testing can not clearly replace full scale testing due to the impossibility of exactly matching all physical processes of interest, it can play an important role in the development of wind energy control technology in general, and of wake control strategies in particular [4].

In this chapter, we experimentally analyze different wake control strategies — namely, de-rating and yawing out of the wind. The analysis considers the effects of these wake manipulation methods on wake recovery, deficit and deflection. The chapter is therefore organized according to the following plan. First, the scaled wind turbine models and experimental facility are described in Section 4.2. Next, experimental results concerning the measurement of the single and multiple wake for different operating conditions of the wind turbine models are discussed in Section 4.3. The main results and conclusions are finally summarized in Section 4.4, which concludes the chapter.

4.2   Experimental setup

For the experimental characterization of the wake shed by a single wind turbine, as well as by a cluster of two wind turbines, scaled tests with up to two G1 models (see Deliverable 3.1) have been conducted in the boundary layer wind tunnel of the Politecnico di Milano, as shown in Figs. 26 and 27.

Figure 26. A single G1 model in the boundary layer wind tunnel of the Politecnico di Milano.
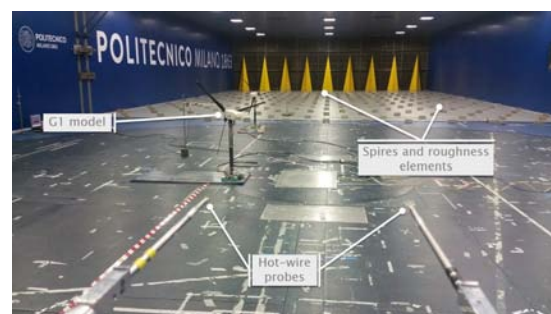
Figure 27. Two G1 models in the boundary layer wind tunnel of the Politecnico di Milano.

The turbines have been operated at moderate (approx. 6%) and high (approx. 11%) turbulence intensity. The ambient wind speed at hub height has been set in most experiments between 5.45

m/s and 5.6 m/s, which corresponds to a wind speed lower than the rated one. The two G1s have been installed in two different layouts, i.e. aligned and laterally shifted of 0.5 diameter, while the longitudinal distance between the turbines has always been set equal to 5D.

The control system of each wind turbine model, described in Deliverable 3.1, was used during the test so as to let the wind turbine models seeking for their optimal operating conditions for a wide range of power derating and yaw misalignment. The wake shed by a single wind turbine, as well as by a cluster of two wind turbines, has also been traversed and sampled at several downstream distances and along horizontal and vertical lines. To this aim, the traversing system and the hot-wire probes described in Deliverable 3.1 has been used.

4.3   Performed wake measurements

In the following, the experimental data concerning the sampling of the single wake are discussed first. Successively, the results related to the sampling of the multiple wake are presented.

4.3.1   Single wake measurements

Single turbine measurements are carried out for two different inflow conditions; below-rated low-turbulent-inflow (mod-TI), characterized by an average speed of 5.60 m/s and a turbulence intensity of 6.12%, and below-rated high-turbulence-inflow (high-TI), characterized by an average wind speed of 5.46 m/s and a turbulence intensity of 11%. For each turbulence intensity, three set of measurements were conducted with different setting of the rotor speed Ω and blade pitch β, with the aim of observing the impact caused by different thrust coefficients C_T on the wake behavior (ID 1-3, 12-14). Moreover, in order to address the effect of different yaw misalignment on the wake characteristics, various measurements were performed with yaw misalignment varying from $-40°$ to $+40°$ (ID 4-11, 15-22), where a positive misalignment corresponds to a counter-clockwise rotation from the wind to the rotor axis looking down onto the terrain. The wind turbine operating conditions, for each of the 22 tested cases, are shown in Table 1.

For each scenario, the wind flow velocity and the turbulence intensity data were sampled at several points along an horizontal line passing at hub height and for 3 downwind distances (x/D = 5 : 2.5 : 10). Additionally, for the cases with yaw-misaligned wind turbine model the wake was also sampled along a vertical line passing through the wake center. The post-processed data therefore consists of average normalized flow velocity and turbulence intensity measured at each sample point, as well as key-parameters like the yaw misalignment γ, the thrust coefficient C_T, the collective blade pitch β and the rotor speed Ω. The average normalized flow velocity is obtained by computing the ratio between the average flow speed in the wake, measured by the hot-wire probe at a specific point placed at an height z from the ground and laterally shifted of the quantity y with respect to the rotor axis, and the corresponding average undisturbed flow speed $U_\infty(y, z)$ measured 4 diameters upstream of the rotor and at the same height and lateral position (see Chapter 3). The turbulence intensity is instead obtained by computing the ratio between the standard deviation of the flow

Table 1. Overview of the operating conditions of the wind turbine model for the single turbine wake measurements, with mod-TI and high-TI inflow conditions.

	$\Omega[rpm]$	$\beta[°]$	$\gamma[°]$	$C_T[-]$	ID
	806.3	1.42	0	0.76	1
	806.0	1.99	0	0.71	2
	796.1	2.50	0	0.67	3
mod-TI	656.4	1.42	−40	0.50	4
	729.4	1.42	−30	0.61	5
	773.2	1.42	−20	0.69	6
	798.4	1.42	−10	0.74	7
V = 5.60 m/s	797.6	1.42	10	0.74	8
	774.9	1.42	20	0.68	9
	731.9	1.42	30	0.60	10
	659.4	1.42	40	0.48	11
	770.6	1.45	0	0.76	12
	773.3	2.05	0	0.71	13
	770.0	2.44	0	0.68	14
high-TI	631.2	1.42	−40	0.49	15
	693.2	1.42	−30	0.60	16
	734.8	1.42	−20	0.69	17
	758.5	1.43	−10	0.74	18
V = 5.46 m/s	760.9	1.43	10	0.75	19
	737.8	1.42	20	0.69	20
	696.2	1.42	30	0.60	21
	629.6	1.42	40	0.48	22

speed in the wake and the average undisturbed flow speed $U_\infty(0, z_H)$ measured by a pitot tube placed 3 diameters upstream of the rotor disk and located at hub height z_H.

The measurements are reported in Figs. 28-44 for both moderate and high turbulence intensities, where each subplot refers to specific wind turbine operating conditions characterized by the thrust coefficient or yaw misalignment reported in the subplot title. The measured data are therefore arranged in groups, as described in the following:

1. Measurements along an horizontal line at hub height for $\gamma = 0°$ and different C_T values.

2. Measurements along an horizontal line at hub height for $\gamma = -40° : 10° : -10°$.

3. Measurements along an horizontal line at hub height for $\gamma = +10° : 10° : +40°$.

4. Measurements along a vertical line passing through the wake center for $\gamma = -40° : 10° : +40°$.

Each subplot within a figure depicts the normalized flow velocity or the turbulence intensity measured at 3 downwind distances from the turbine, as described in the legend. For measurements along an horizontal line at hub height, normalized velocities are reported on the y-axis, while the x-axis refers to the lateral distance from the rotor axis, expressed in rotor diameter. For measurements along a vertical line passing through the wake center, instead, normalized velocities are reported on the x-axis, while the y-axis refers to the distance of the measurement point from the ground, again expressed in rotor diameter.

Figs. 28-31 report the normalized flow velocity measured with moderate turbulent inflow conditions, while figs. 32-35 report the normalized flow velocity measured with high turbulent inflow conditions.
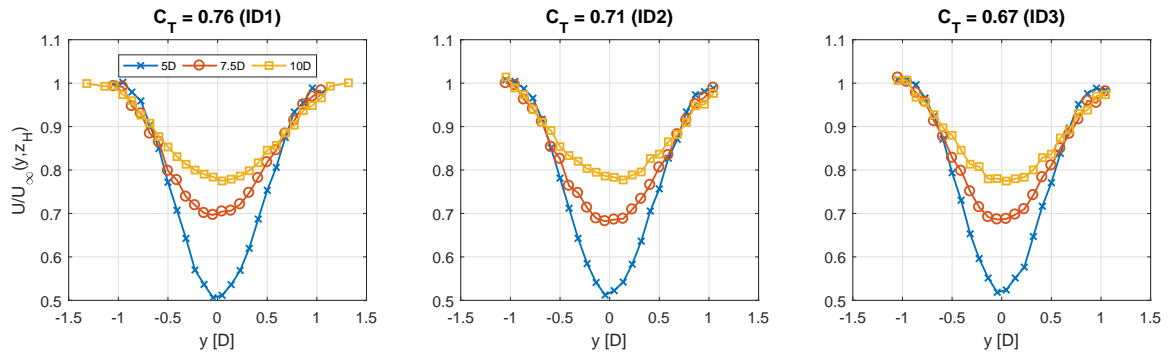
Figure 28. Single turbine wake speed measurements along horizontal lines for mod-TI, zero yaw misalignment, three C_T settings (ID 1-3).
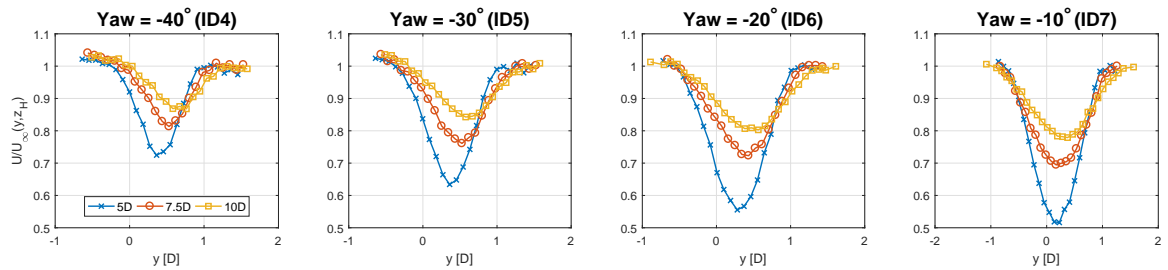
Figure 29. Single turbine wake speed measurements along horizontal lines for mod-TI, negative yaw misalignment (ID 4-7).
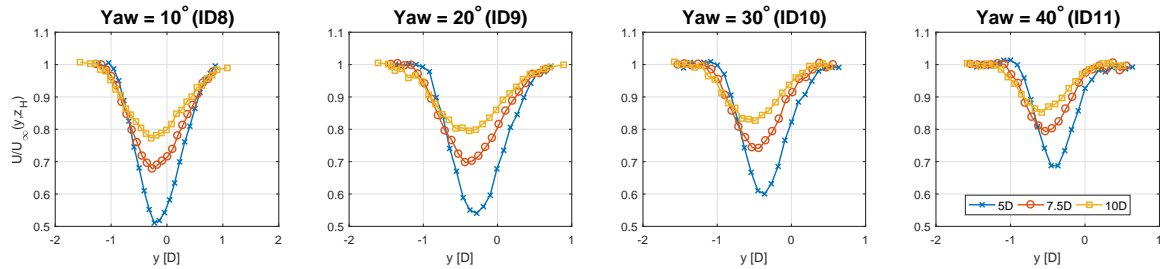
Figure 30. Single turbine wake speed measurements along horizontal lines for mod-TI, positive yaw misalignment (ID 8-11).

The measured wake centre positions are shown in Fig. 36 together with the fitted linear models, obtained with data related to misalignment angles $|\vartheta| \leq 20°$. By looking at the coefficients of these linear models, reported in Table 2, it is possible to first note that the wake deflection increases further downstream from the rotor disk, as generally expected. Moreover, the lower the inflow turbulence is, the higher is the amount of wake deflection that can be achieved by misaligning the wind turbine. These results well agrees with [1], where it is concluded that a low incoming turbulence extends the near wake region while reducing the flow entrainment in the far-wake region, thus leading to a stronger wake deflection.
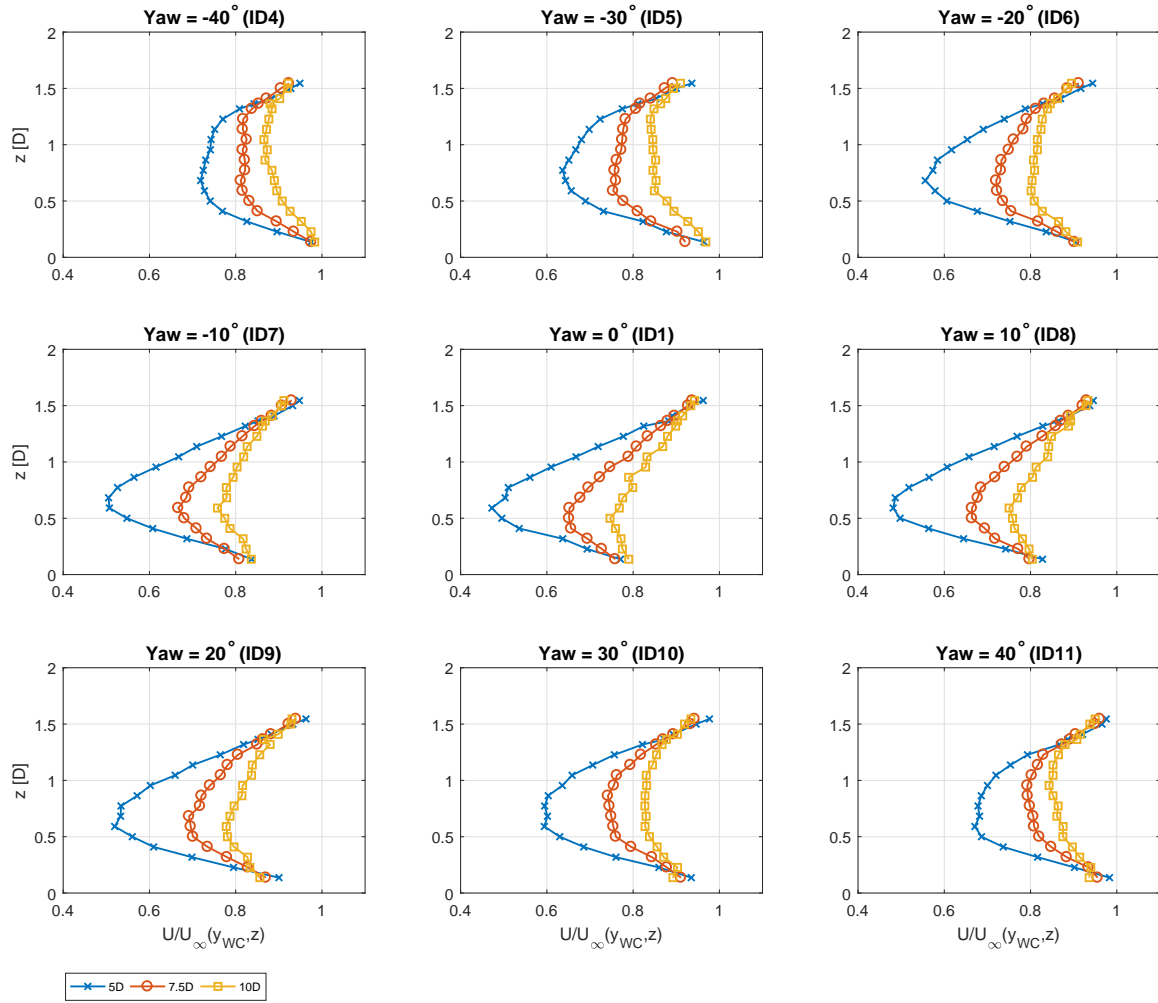
Figure 31. Single turbine wake speed measurements along vertical lines for mod-TI, yaw misalignment from $-40°$ to $+40°$ (ID 1, 4-11).
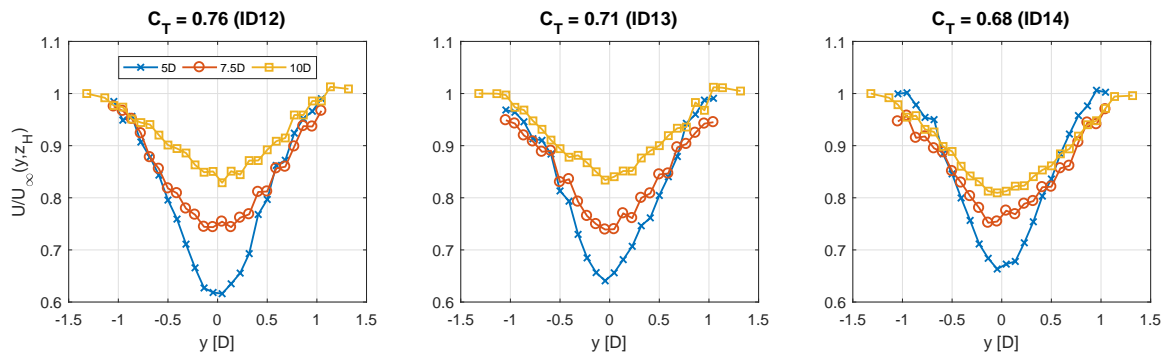
Figure 32. Single turbine wake speed measurements along horizontal lines for high-TI, zero yaw misalignment, three C_T settings (ID 12-14).
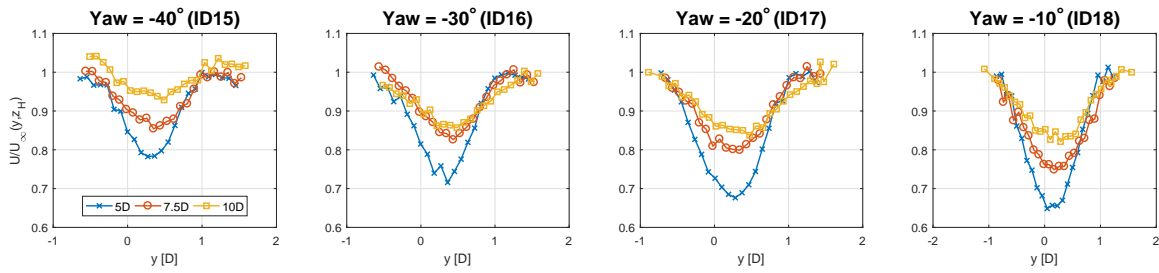
Figure 33. Single turbine wake speed measurements along horizontal lines for high-TI, negative yaw misalignment (ID 15-18).
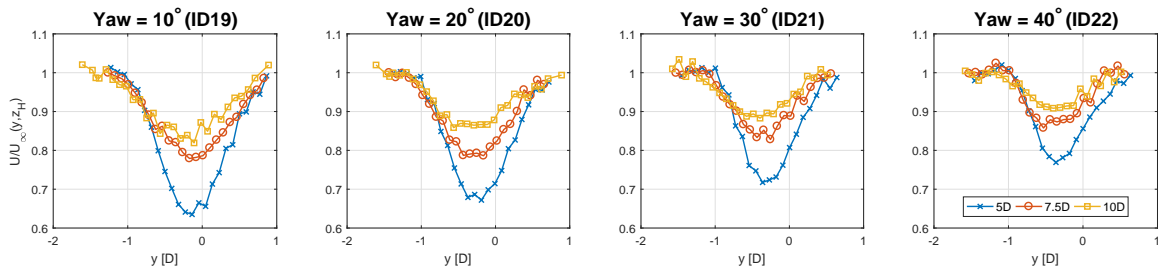
Figure 34. Single turbine wake speed measurements along horizontal lines for high-TI, positive yaw misalignment (ID 19-22).

The data reported in Fig 36 and Table 2 also show that the wake is deflected toward the left even for null yaw misalignment. Moreover, this null-yaw deflection increases as higher the vertical shear is. This can be explained by the very presence of a sheared inflow. Indeed, in the presence of a vertical speed gradient caused by the shear, blade section conditions are different for the top and bottom parts of the rotor, resulting in different sectional aerodynamic forces, which has the effect of generating a small non-zero net lateral resultant, which is eventually responsible for the side-ways deflection of the wake observed in Fig. 36 for null yaw.

Table 2. Coefficients of the linear model $\frac{y_{\mathrm{WC}}}{D} = \frac{\partial y_{\mathrm{WC}}}{\partial \vartheta}\vartheta + y_{\mathrm{WC},0}$ that best fits the wake deflections for $|\vartheta| \leq 20°$ and for mod-TI and migh-TI flow conditions.

x/D [-]	mod-TI		high-TI	
	$\frac{\partial y_{\mathrm{WC}}}{\partial \vartheta}$	$y_{\mathrm{WC},0}$	$\frac{\partial y_{\mathrm{WC}}}{\partial \vartheta}$	$y_{\mathrm{WC},0}$
5	0.0144	-0.0148	0.0118	-0.0126
7.5	0.0186	-0.0180	0.0152	-0.0438
10	0.0220	-0.0547	0.0199	-0.0916

The turbulence intensity is depicted similar to the representation of the flow velocity. Fig. 37 reports the turbulence intensity at different downwind distances in the wake for several thrust coefficients of the turbine. In each subplot the lateral distance is shown in the x-axis and y-axis denotes the turbulence intensity value. Each downwind distance is shown with a different line, as explained in the legend.

Figs. 37-40 depict the turbulence intensity measured in the wake at different downwind distances and for moderate turbulent inflow conditions. Similarly to the wake data, for measurements along
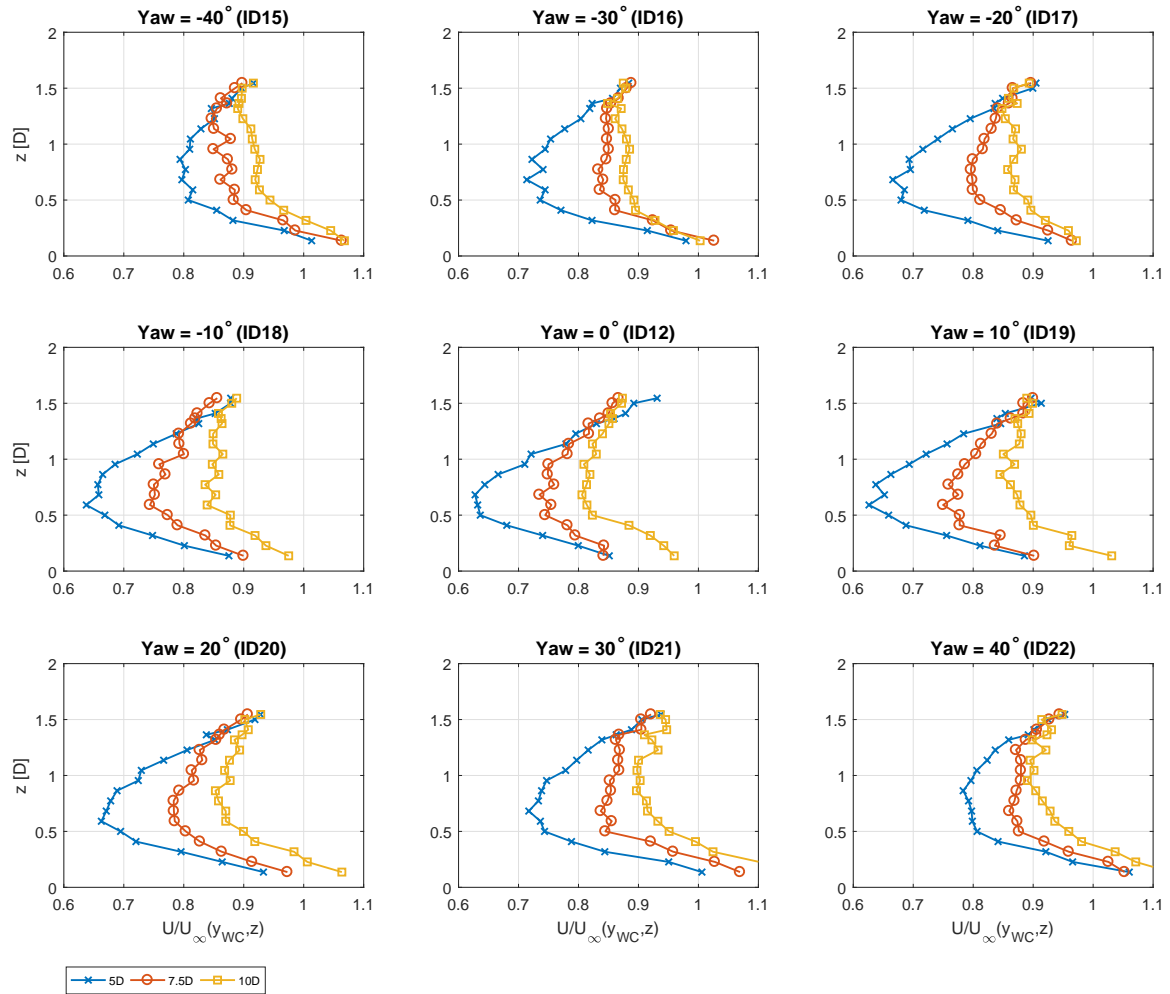
Figure 35. Single turbine wake speed measurements along vertical lines for high-TI, yaw misalignment from $-40°$ to $+40°$ (ID 12, 15-22).

(a) Mod-TI inflow conditions.   **(b) High-TI inflow conditions.**
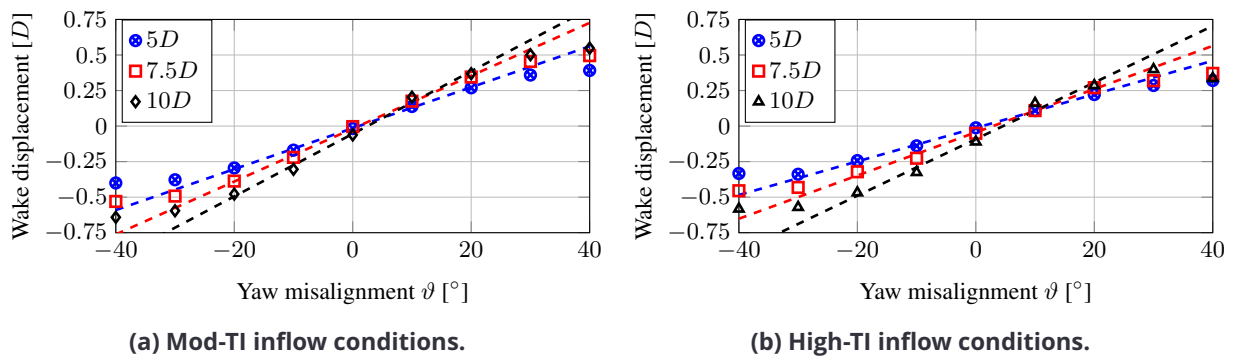
Figure 36. Wake deflection vs. misalignment angle at 5D, 7.5 and 10D downstream distances in a sheared and turbulent flow, the dashed lines representing fitted linear models.

an horizontal line at hub height the turbulence intensities are reported on the y-axis, while for measurements along a vertical line passing through the wake center the turbulence intensities are reported on the x-axis. Figs. 41-44) report the turbulence intensity measured in the wake for high turbulent inflow conditions.
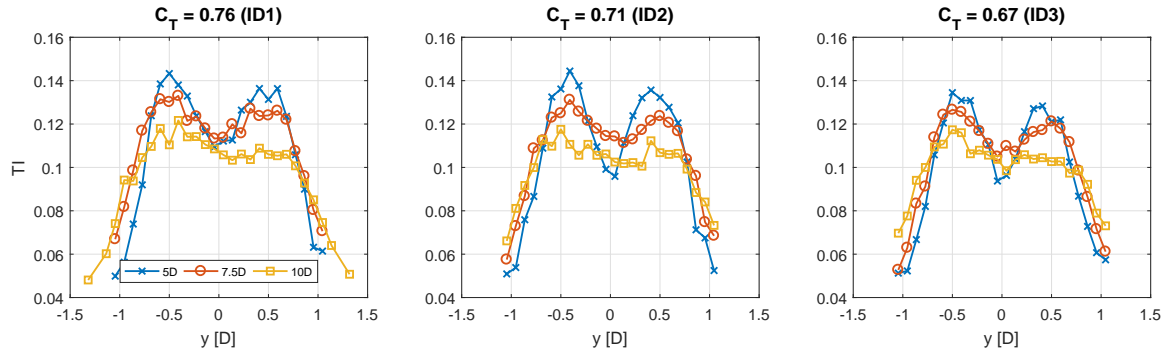
Figure 37. Single turbine turbulence intensity measurements along horizontal lines for mod-TI, zero yaw misalignment, three C_T settings (ID 1-3).
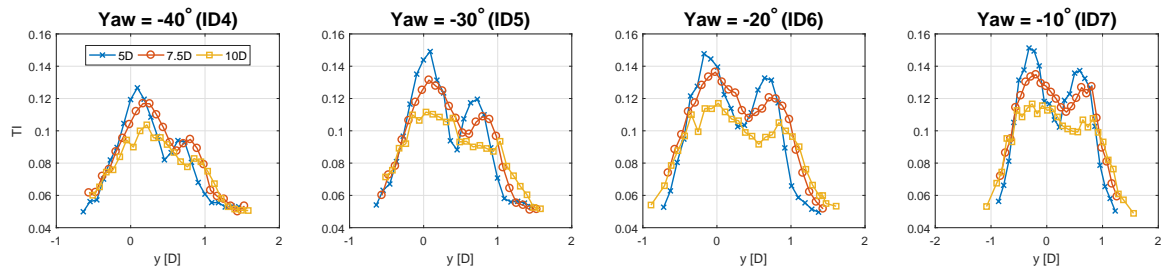
Figure 38. Single turbine turbulence intensity measurements along horizontal lines for mod-TI, negative yaw misalignment (ID 4-7).
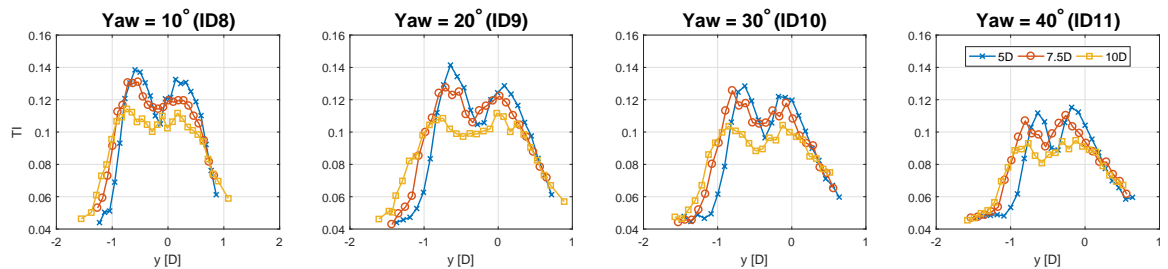
Figure 39. Single turbine turbulence intensity measurements along horizontal lines for mod-TI, positive yaw misalignment (ID 8-11).

4.3.2 Multiple wake measurements

The measurements of the speed in the multiple wake shed by a cluster of two wind turbines have been conducted again with two different inflow conditions: moderate and high turbulent inflow characterized by an average speed of approx. 5.75 m/s and 5.65 m/s, respectively for mod-TI and high-TI. With both the wind turbines aligned, five measurements were conducted with different setting of the rotor speed Ω and blade pitch β, with the aim of observing the impact caused by different thrust
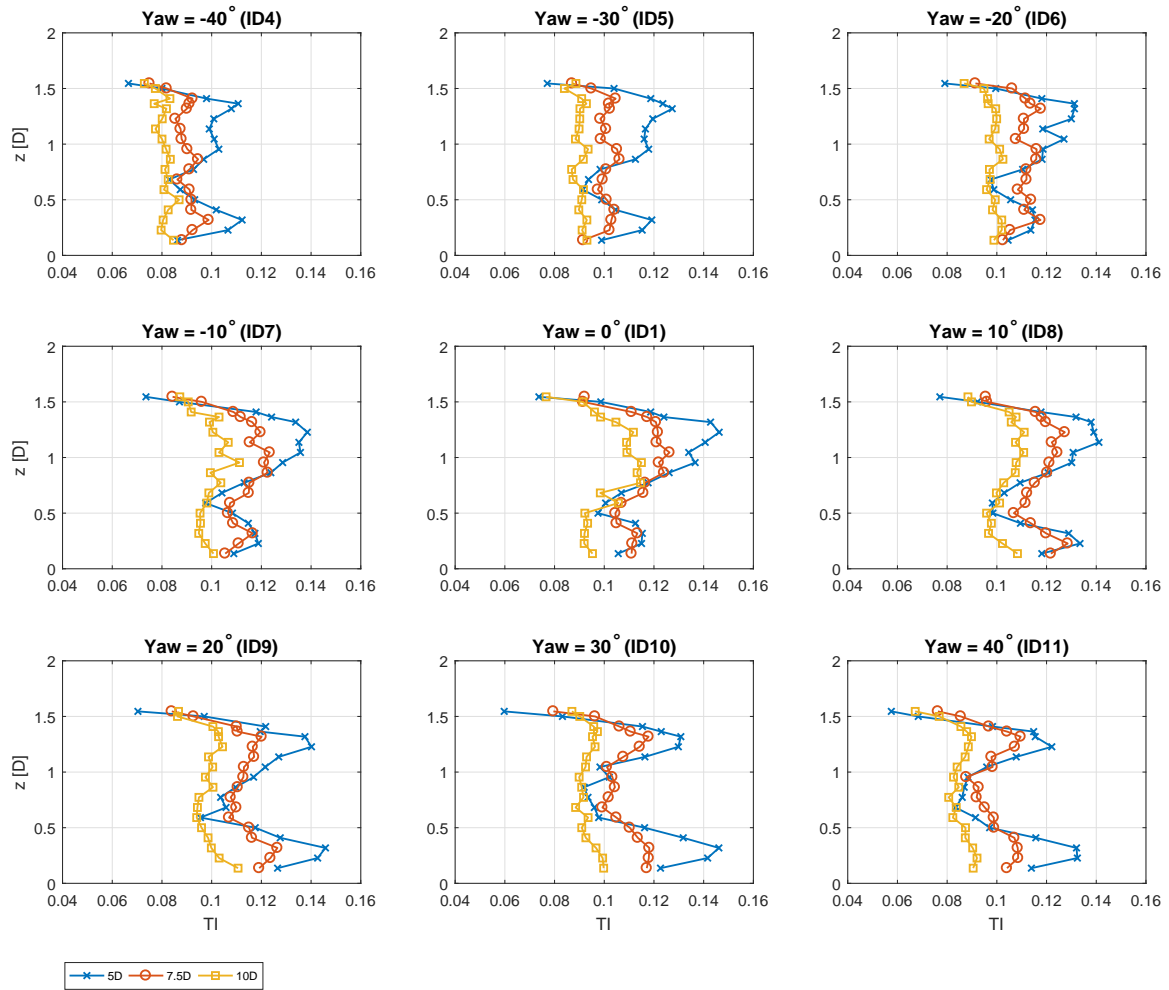
Figure 40. Single turbine turbulence intensity measurements along vertical lines for mod-TI, yaw misalignment from $-40°$ to $+40°$ (ID 1, 4-11).
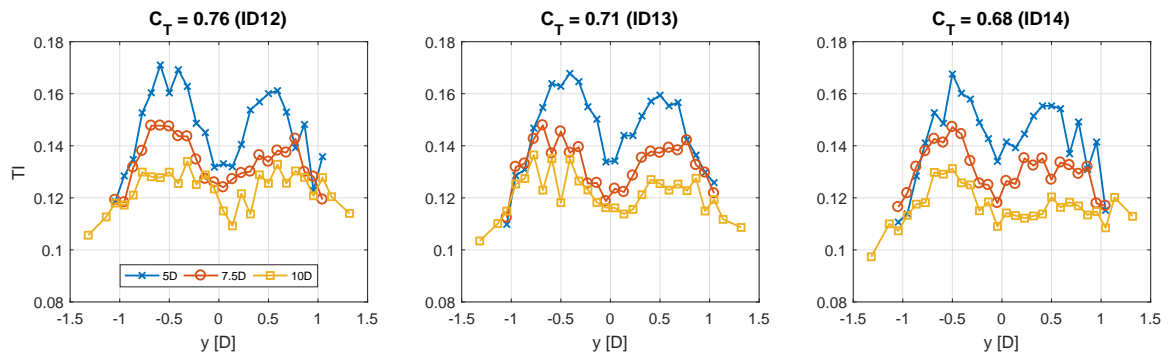
Figure 41. Single turbine turbulence intensity measurements along horizontal lines for high-TI, zero yaw misalignment, three C_T settings (ID 12-14).
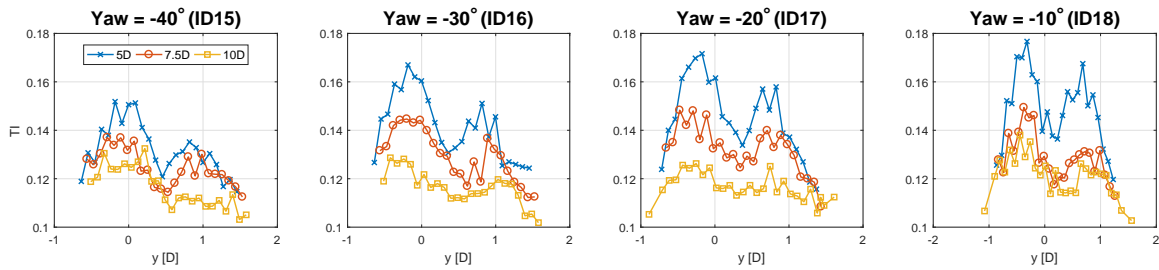
**Figure 42. Single turbine turbulence intensity measurements along
horizontal lines for high-TI, negative yaw misalignment (ID 15-18).**
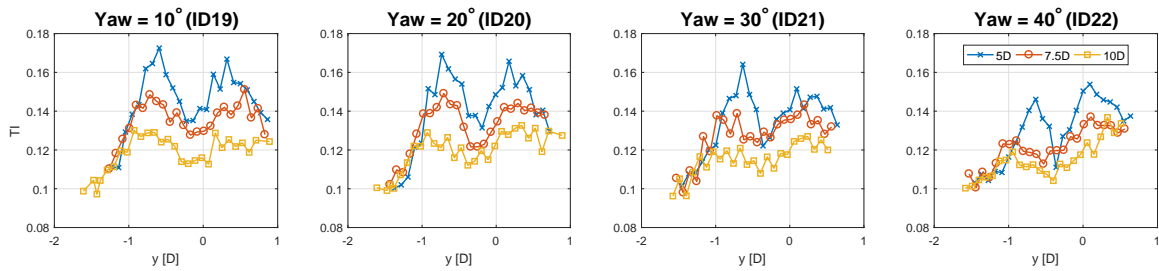
**Figure 43. Single turbine turbulence intensity measurements along
horizontal lines for high-TI, positive yaw misalignment (ID 19-22).**

coefficients C_T on the wake behavior (ID 1-5, ID 13-17). Moreover, in order to address the effect of different yaw misalignments on the wake characteristics, various measurements were performed with three yaw misalignment configurations of the aligned machines (ID 6-8, ID 18-20). Lastly the downwind turbine has been laterally shifted of 0.5D to the left (looking downwind) and the effect on the wake characteristics of different combinations of yaw misalignment has been investigated (ID 9-12, 21-24). The operating conditions of both the wind turbines, for each of the 24 tested cases, are shown in Table 3, where $(\bullet)^{WT1}$ and $(\bullet)^{WT2}$ indicate quantities pertaining to the upstream and downstream wind turbine, respectively.

For each tested case, flow velocity within the wake and turbulence intensity data were sampled at several points and for different distances (7.5D and 10D) from the rotor disk of the upstream wind turbine. For all cases, the measurements were conducted along horizontal lines passing through hub height, while for some cases the measurements were also carried along horizontal lines located 0.36D above and below the hub height. The post-processed data consists of average normalized flow velocity and turbulence intensity measured at each sample point, as well as key-parameters like the yaw misalignment γ, the thrust coefficient C_T, the collective blade pitch β and the rotor speed Ω of both the wind turbine models. Similarly to the data pertaining the single wake measurements, the average normalized flow velocity is obtained by computing the ratio between the average flow speed in the wake and the corresponding average undisturbed flow speed $U_\infty(y,z)$ measured 4 diameters upstream of the rotor, while the turbulence intensity is again obtained by computing the ratio between the standard deviation of the flow speed in the wake and the average undisturbed flow speed $U_\infty(0, z_H)$ measured by a pitot tube placed 3 diameters upstream of the rotor disk.
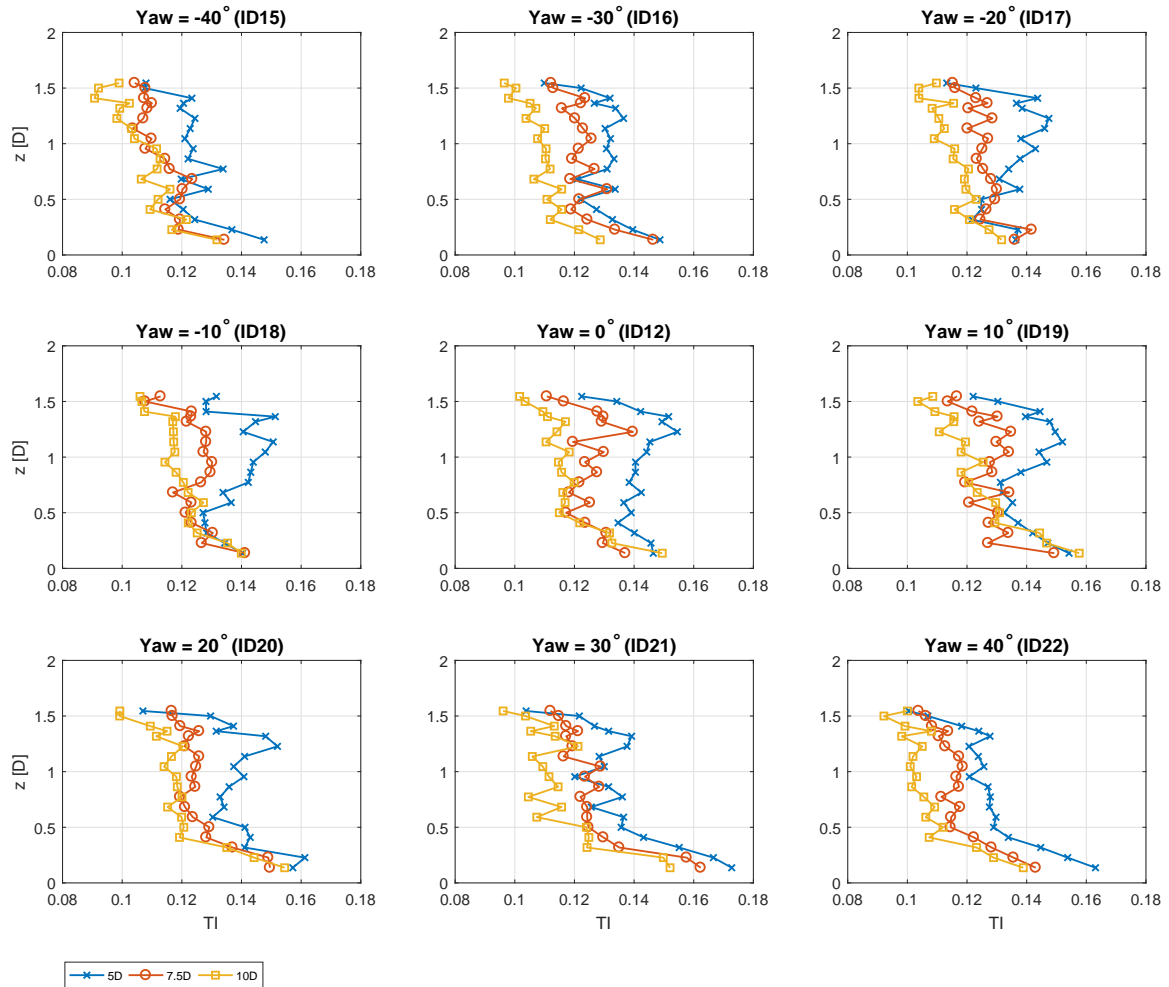
Figure 44. Single turbine turbulence intensity measurements along vertical lines for high-TI, yaw misalignment from $-40°$ **to** $+40°$ **(ID 12, 15-22).**

Table 3. Overview of the operating conditions of the wind turbine models for the multiple turbine wake measurements, with mod-TI and high-TI inflow conditions.

	$\Omega^{WT1}[rpm]$	$\Omega^{WT2}[rpm]$	$\beta^{WT1}[°]$	$\beta^{WT2}[°]$	$\gamma^{WT1}[°]$	$\gamma^{WT2}[°]$	$C_T^{WT1}[-]$	$C_T^{WT2}[-]$	ID
	817.7	558.0	0.44	0.42	0	0	0.81	0.84	1
	817.8	566.7	1.26	0.42	0	0	0.75	0.83	2
	804.9	576.4	1.93	0.42	0	0	0.70	0.83	3
low TI	812.9	548.8	1.27	2.01	0	0	0.75	0.71	4
	804.9	559.3	2.01	1.89	0	0	0.69	0.72	5
	750.6	729.9	0.42	0.42	30	0	0.65	0.85	6
	750.2	642.0	0.42	0.42	30	30	0.66	0.66	7
V = 5.73 m/s	812.9	513.5	0.44	0.42	0	30	0.81	0.65	8
	819.3	693.6	0.45	0.42	0	0	0.81	0.82	9
	818.6	597.5	0.44	0.42	0	30	0.81	0.65	10
	783.9	799.9	0.42	0.42	30	0	0.66	0.84	11
	738.5	726.3	0.42	0.42	30	30	0.65	0.67	12
	789.2	608.1	0.52	0.42	0	0	0.81	0.83	13
	787.7	620.2	1.65	0.42	0	0	0.72	0.82	14
high TI	781.5	627.1	2.14	0.42	0	0	0.68	0.82	15
	787.7	603.8	1.71	1.80	0	0	0.71	0.73	16
	781.0	609.6	2.17	1.86	0	0	0.67	0.72	17
	721.4	684.4	0.42	0.42	30	0	0.65	0.84	18
	723.5	608.0	0.42	0.42	30	30	0.65	0.66	19
V = 5.63 m/s	797.9	554.6	0.53	0.42	0	30	0.80	0.65	20
	796.0	677.2	0.53	0.42	0	0	0.79	0.83	21
	790.8	601.5	0.53	0.42	0	30	0.79	0.66	22
	721.7	742.4	0.42	0.42	30	0	0.63	0.83	23
	726.4	670.3	0.42	0.42	30	30	0.64	0.68	24

The wind tunnel measurements of the multiple wake are shown in Figs. 45-56 for both moderate and high inflow turbulence intensities. The measured data are therefore arranged in groups, as described in the following:

1. Measurements with aligned wind turbines and various combinations of the C_T values of both turbines, with $\gamma^{WT1} \setminus \gamma^{WT2} = 0° \setminus 0°$.

2. Measurements with aligned wind turbines and various combinations of $\gamma^{WT1} \setminus \gamma^{WT2}$.

3. Measurements with laterally shifted wind turbines and various combinations of $\gamma^{WT1} \setminus \gamma^{WT2}$.

For the measurements with aligned wind turbines and various combinations of the C_T values of both turbines, each subplot within a figure depicts the normalized flow velocity or the turbulence intensity measured at 2 downwind distances from the turbine, as described in the legend. For measurements with aligned and laterally shifted wind turbines and various combinations of $\gamma^{WT1} \setminus \gamma^{WT2}$, each subplot within a figure depicts the normalized flow velocity or the turbulence intensity measured along three horizontal lines, as described in the legend, and at a single downwind distance. Normalized velocities are reported on the y-axis, while the x-axis refers to the lateral distance from the rotor axis, expressed in rotor diameter.

Fig. 45 displays the distribution of the normalized velocity in the wake when both turbines are aligned, impinged by a moderately turbulent inflow and operating at conditions characterized by the thrust coefficients reported in the title of each subplot.
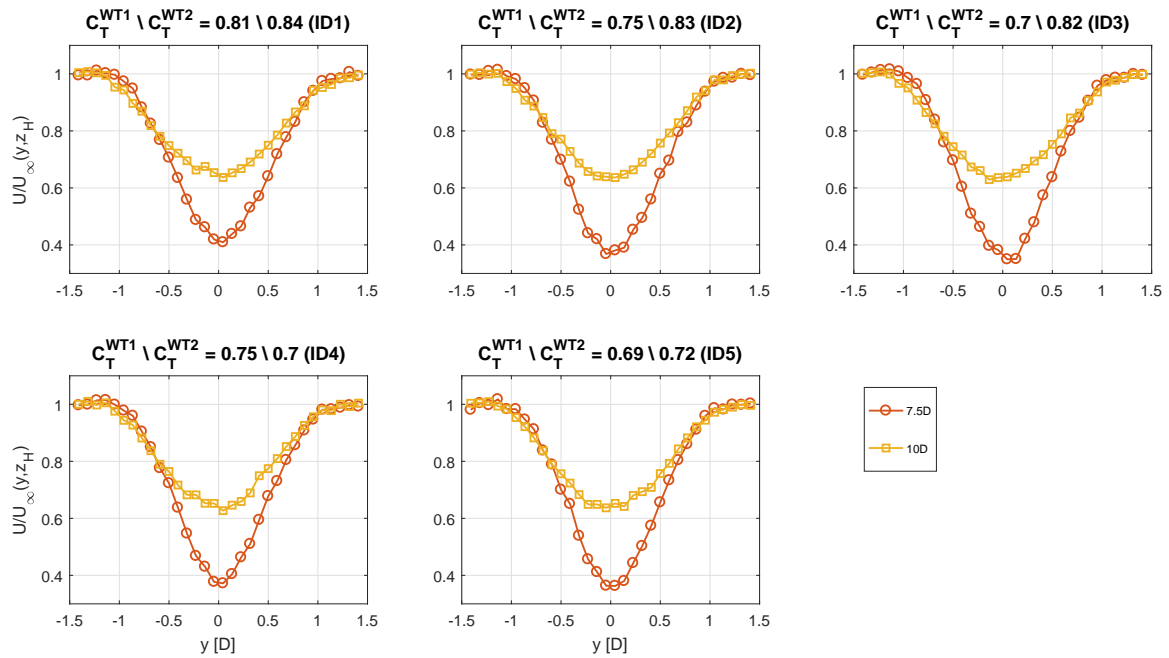
Figure 45. Wake speed measurements along horizontal lines with aligned wind turbines, mod-TI inflow conditions, $\gamma^{WT1} \setminus \gamma^{WT2} = 0° \setminus 0°$ and for different combinations of $C_T^{WT1} \setminus C_T^{WT2}$ (ID 1-5).

Fig. 46 reports the average normalized velocity in the wake measured with aligned wind turbines impinged by a moderately turbulent inflow and operating at three combinations of $\gamma^{WT1} \setminus \gamma^{WT2}$. Differently from the previous figures, each subplot within Fig. 46 does not depict the wake flow traversed at multiple downstream distances but rather wake data pertaining to measurements performed along three horizontal lines located at different heights from the ground. The data measured above the hub height are denoted with an upward pointing triangle, while data measured below the hub height are marked by a downward pointing triangle, as stated in the legend. The upper set of subplots — subplots 1-3 — show the data measured at 7.5D downstream of the upstream wind turbine, while the lower set of subplots report the measurements conducted 10D behind the upstream machine.

The data related to measurements performed with laterally shifted wind turbines and moderate inflow turbulence intensity are presented in Fig. 47. The subplots in the figure present the measured normalized wake speed along the longitudinal axis for several combinations of the yaw misalignment of both the wind turbines, as reported in the titles of the four upper subplots. For the mentioned cases the measurements were conducted along horizontal lines located at several distance form the ground; this means that each line in a subplot refers to a different measurement height, as reported in the figure's legend. Similarly to the previous figure, the upper subplots report data measured 7.5D downstream of the upstream machine, while data concerning measurements conducted at 10D are depicted in the lower subplots.
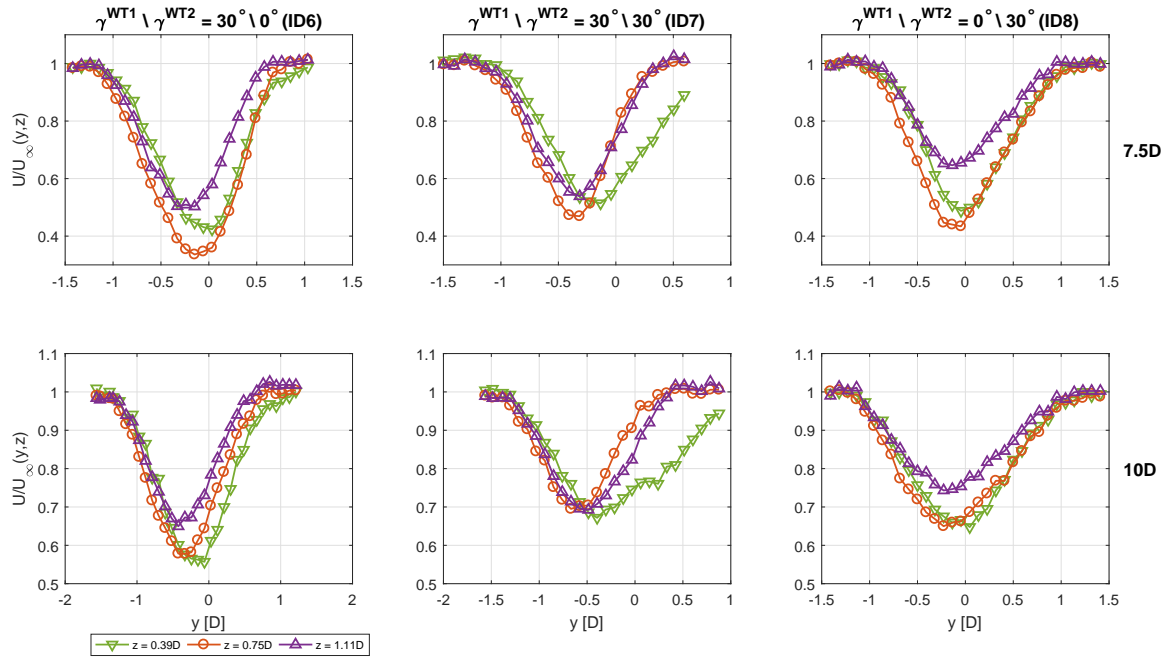
Figure 46. Wake speed measurements along horizontal lines with aligned wind turbines, mod-TI inflow conditions and for three different $\gamma^{WT1} \setminus \gamma^{WT2}$ combinations (ID 6-8).
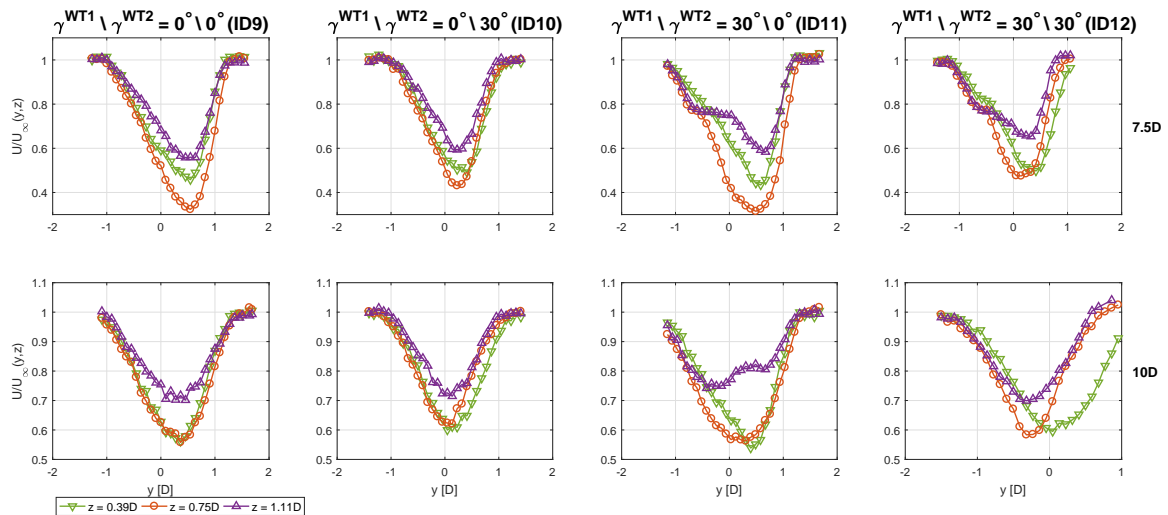
Figure 47. Wake speed measurements along horizontal lines with laterally-shifted wind turbines, mod-TI inflow conditions and for four different $\gamma^{WT1} \setminus \gamma^{WT2}$ combinations (ID 9-12).

The measurements of the wake flow speed performed with high inflow turbulence intensity are presented in Figs .48-50. Note that for some cases the wake flow has been traversed only along horizontal lines passing through the hub rather than at three distances from the ground.
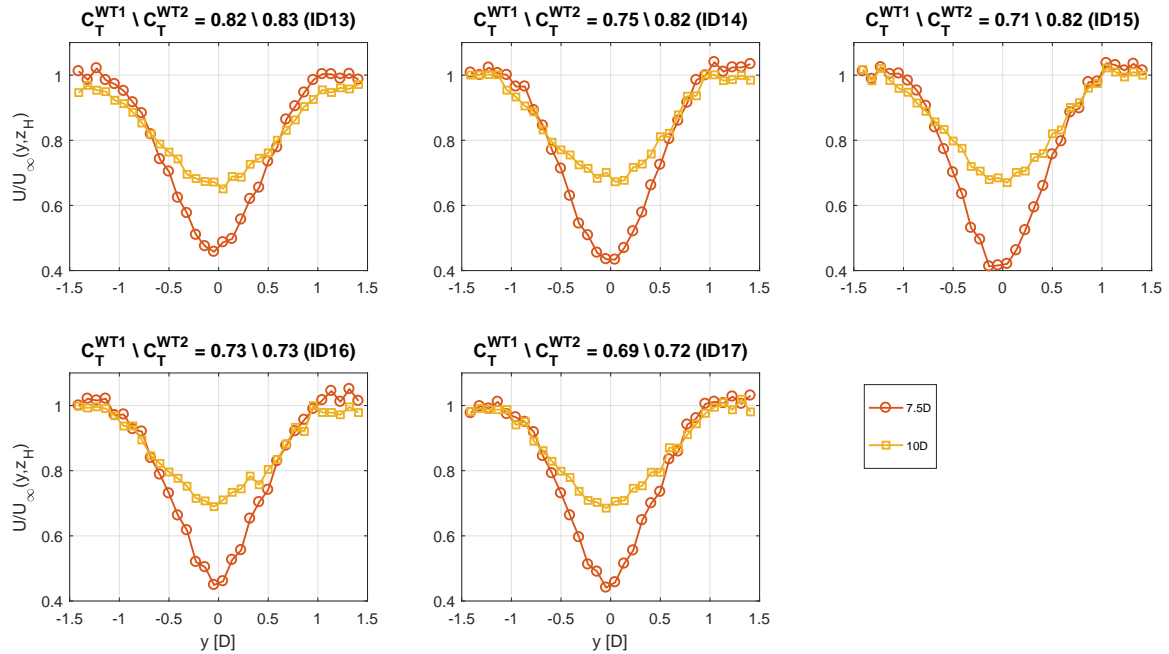
Figure 48. Wake speed measurements along horizontal lines with aligned wind turbines, high-TI inflow conditions, $\gamma^{WT1} \setminus \gamma^{WT2} = 0° \setminus 0°$ and for different combinations of $C_T^{WT1} \setminus C_T^{WT2}$ (ID 13-17).

The turbulence intensity plots are similar to the wake speed plots. Instead of wind flow velocity measurements, turbulence intensity measurement values are reported on the y-axis. In Fig. 51 the turbulence intensity values are displayed for various combinations of the models thrust coefficients and for low inflow turbulence intensity. Each subplot contains the turbulence intensity values for two different downwind distances, as described within the legend.

The turbulence intensity values measured along horizontal lines located at different height from the wind tunnel floor are shown in each subplot of Fig. 52. Each row of subplots show measurements performed at 7.5D or 10D downstream of the upstream machine, while each column of subplots depicts data pertaining a specific combination of upstream and downstream turbines yaw misalignment. The cases mentioned in this figure consider aligned turbines, while the y-axis and x-axis represent the turbulence intensity and lateral distance from the axis of the upstream rotor, respectively.

Fig. 53 reports the turbulence intensity measured within the multiple wake shed by two wind turbines laterally shifted of 0.5D. Each subplot reports data related to one combination of the two machines yaw misalignment, denoted by the title of each column, and to a specific downwind distance, as reported at the end of each row. Turbulence intensity is plotted with respect to the lateral distance from the axis of the upstream rotor in each subplot. Again, data measured at different altitude from the ground are marked differently, as reported in the legend.
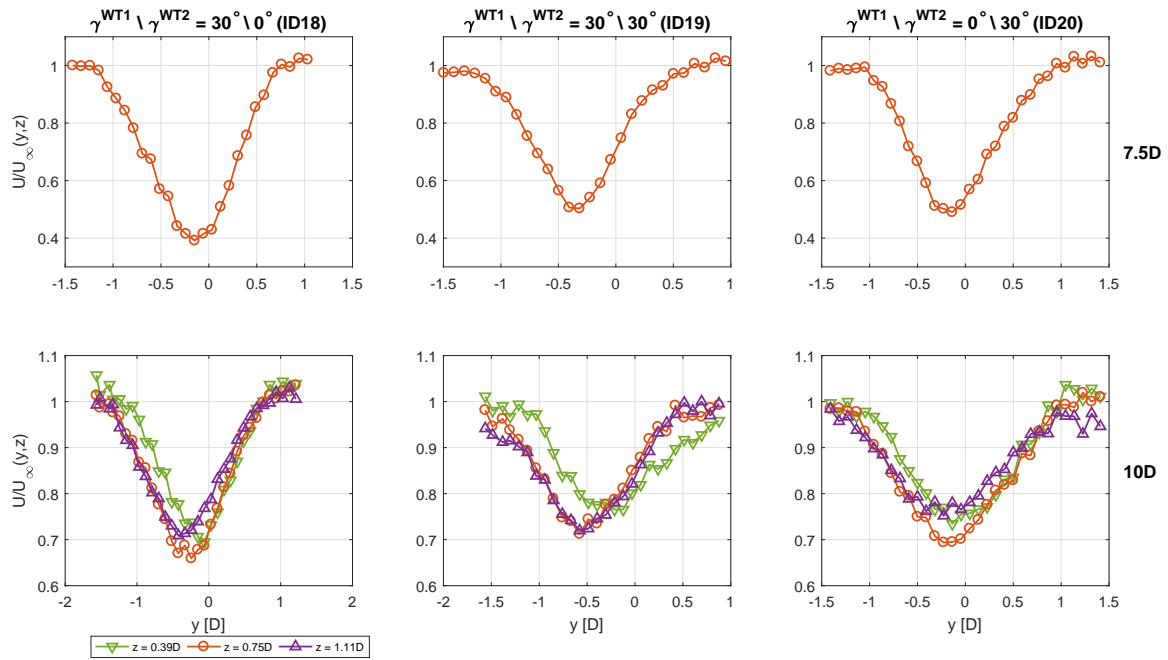
Figure 49. Wake speed measurements along horizontal lines with aligned wind turbines, high-TI inflow conditions and for three different $\gamma^{WT1} \setminus \gamma^{WT2}$ combinations (ID 18-20).
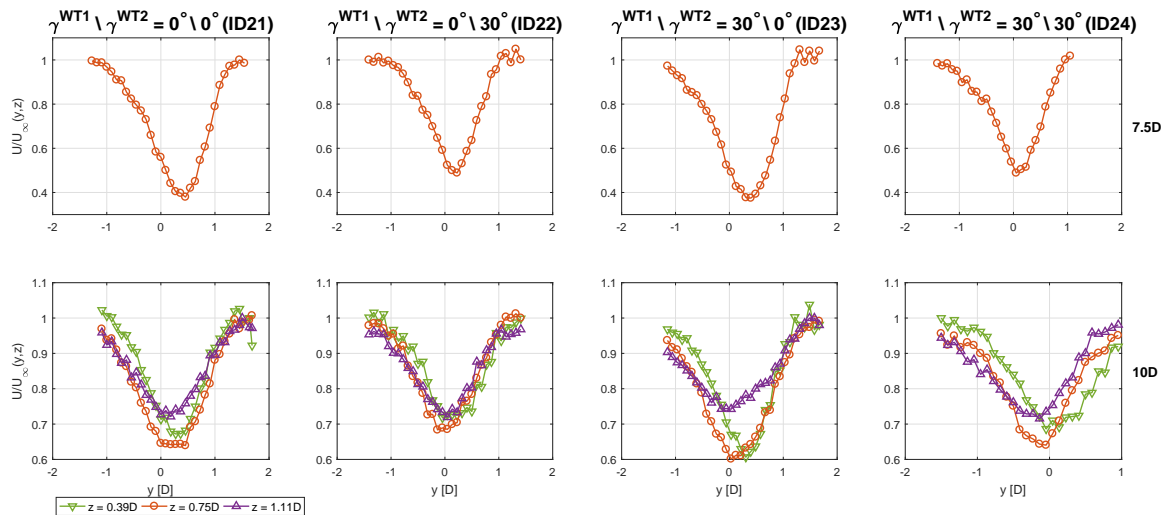
Figure 50. Wake speed measurements along horizontal lines with laterally-shifted wind turbines, high-TI inflow conditions and for four different $\gamma^{WT1} \setminus \gamma^{WT2}$ combinations (ID 21-24).
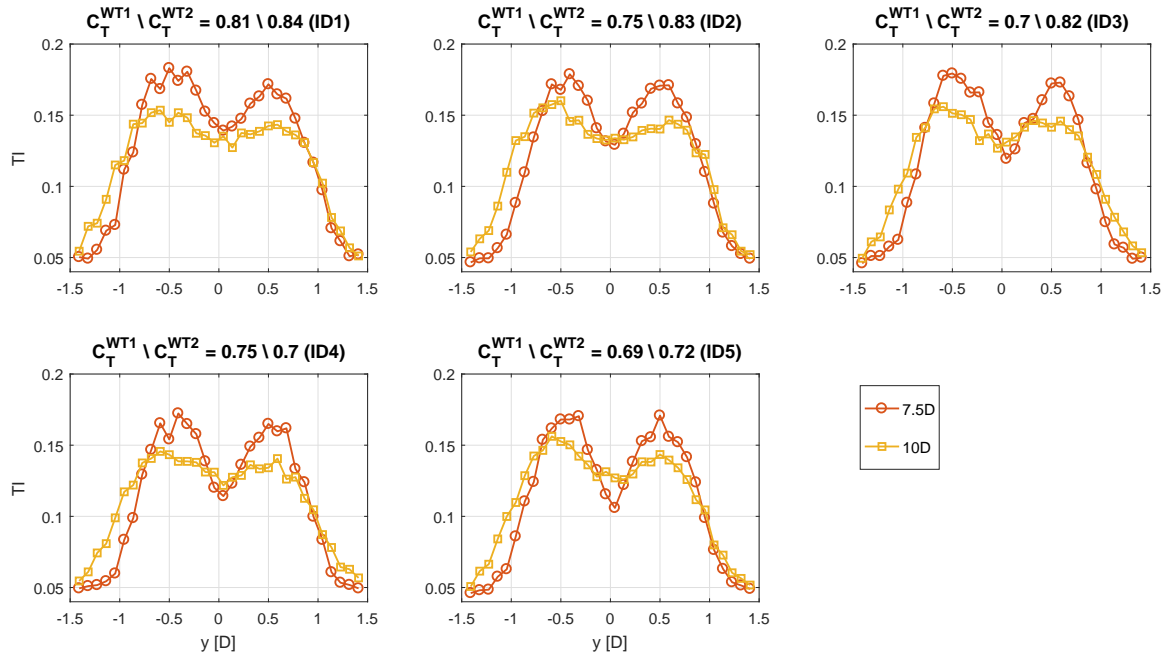
Figure 51. Turbulence intensity measurements along horizontal lines with aligned wind turbines, mod-TI inflow conditions, $\gamma^{WT1} \setminus \gamma^{WT2} = 0° \setminus 0°$ and for different combinations of $C_T^{WT1} \setminus C_T^{WT2}$ (ID 1-5).
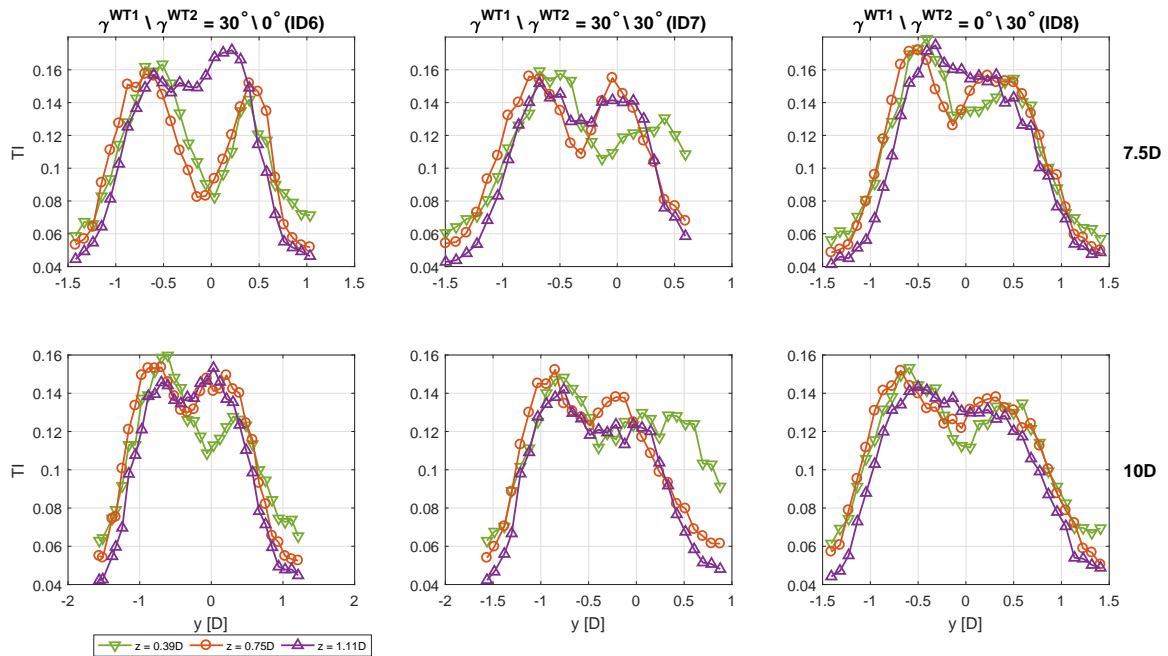
Figure 52. Turbulence intensity measurements along horizontal lines with aligned wind turbines, mod-TI inflow conditions and for three different $\gamma^{WT1} \setminus \gamma^{WT2}$ combinations (ID 6-8).

Finally, Figs. 54-56 report the turbulence intensity values associated to high turbulent inflow conditions.
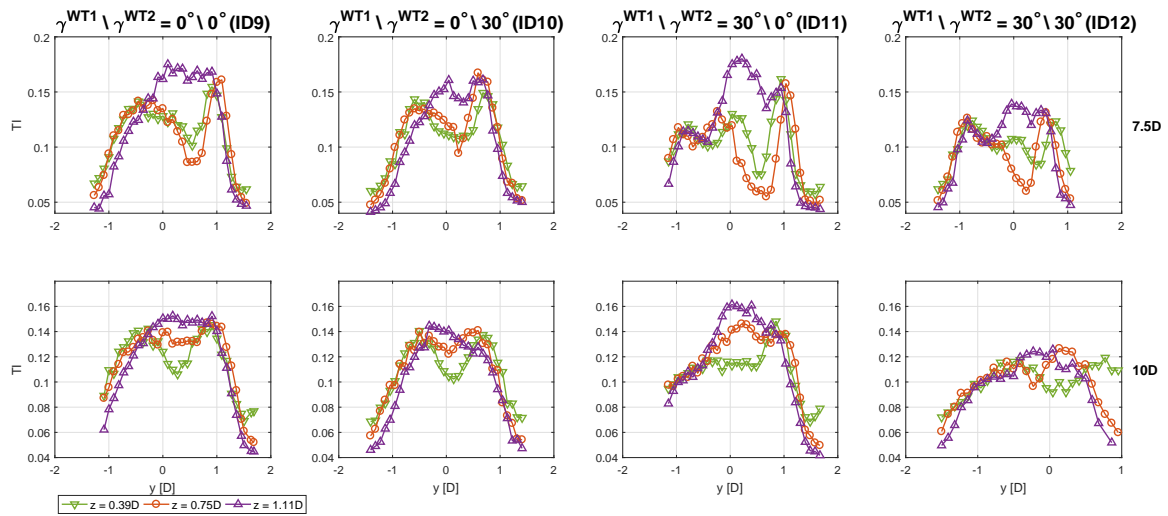
Figure 53. Turbulence intensity measurements along horizontal lines with laterally-shifted wind turbines, mod-TI inflow conditions and for four different $\gamma^{WT1} \setminus \gamma^{WT2}$ combinations (ID 9-12).

4.4   Conclusions

Two wind tunnel testing campaigns have been performed within the CL-Windcon project with the aim of measuring the characteristics of the wake shed by a single wind turbine model and by a cluster of two wind turbine models. The models have been operated under a wide range of conditions in order to experimentally analyze the effect of different wake control strategies — namely, de-rating and yawing out of the wind — on the wake recovery, deficit and deflection.

A valuable set of high quality flow data has been generated, post-processed, organized and distributed to the project consortium. The data are going to be used to validate and further develop a plethora of wind farm models, described in Deliverable 1.2, characterized by different computational costs and fidelity level. Moreover, the presented data are going to be uploaded in a server whose access will be freely and publicly granted at the end of the project.
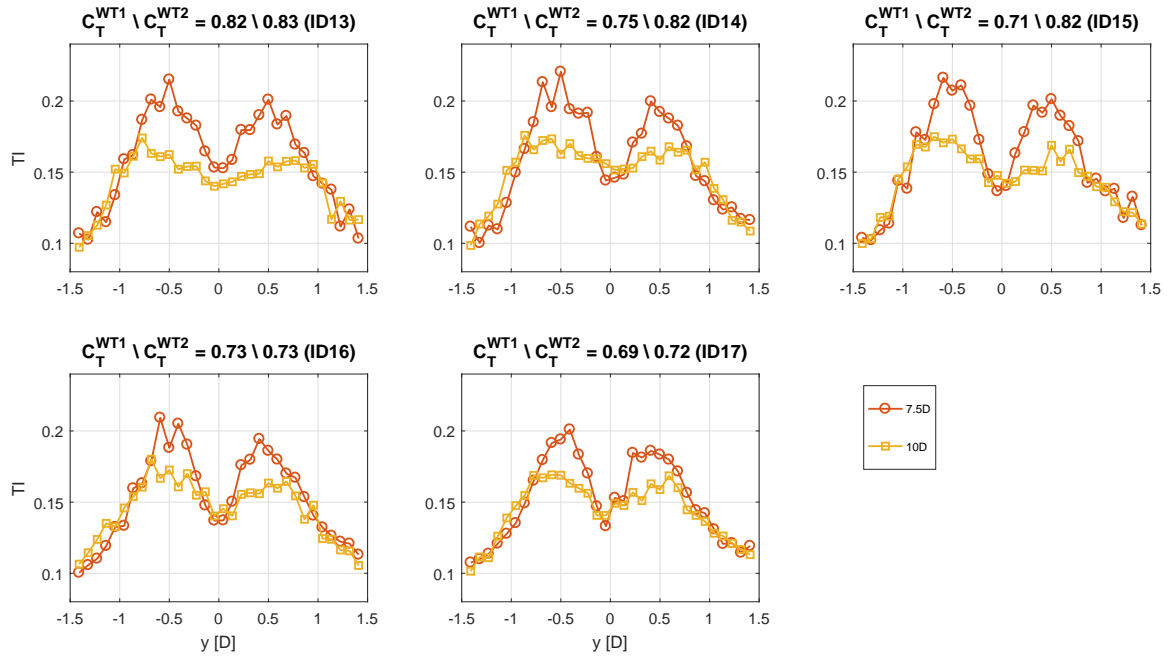
Figure 54. Turbulence intensity measurements along horizontal lines with aligned wind turbines, high-TI inflow conditions, $\gamma^{WT1} \setminus \gamma^{WT2} = 0° \setminus 0°$ and for different combinations of $C_T^{WT1} \setminus C_T^{WT2}$ (ID 13-17).
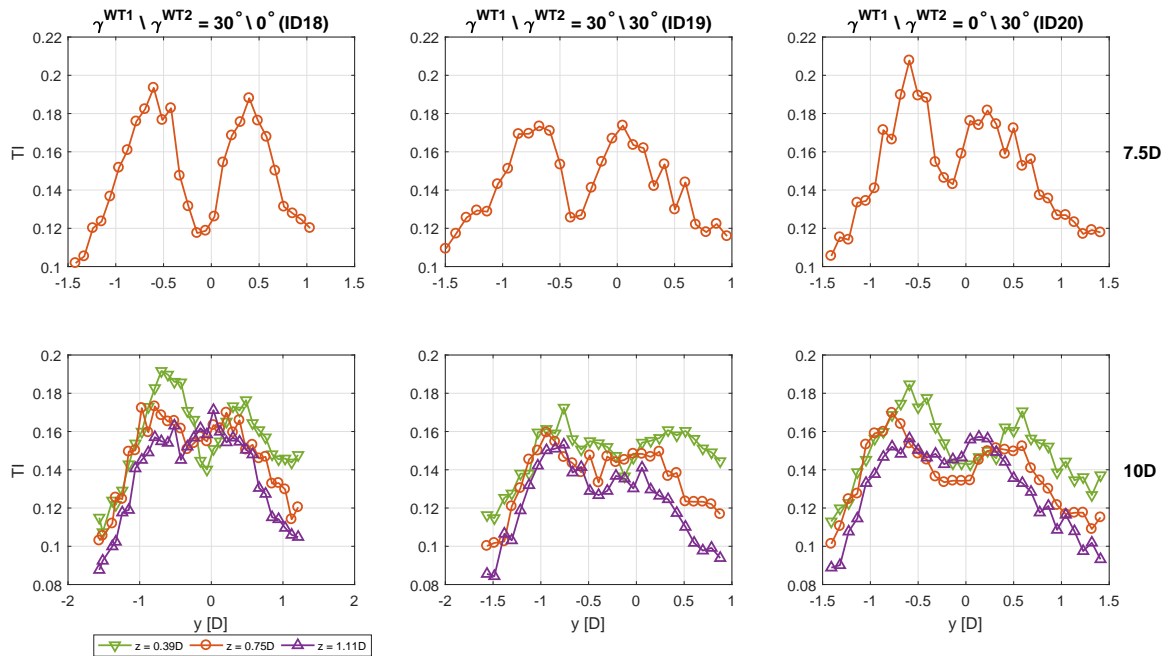
Figure 55. Turbulence intensity measurements along horizontal lines with aligned wind turbines, high-TI inflow conditions and for three different $\gamma^{WT1} \setminus \gamma^{WT2}$ combinations (ID 18-20).
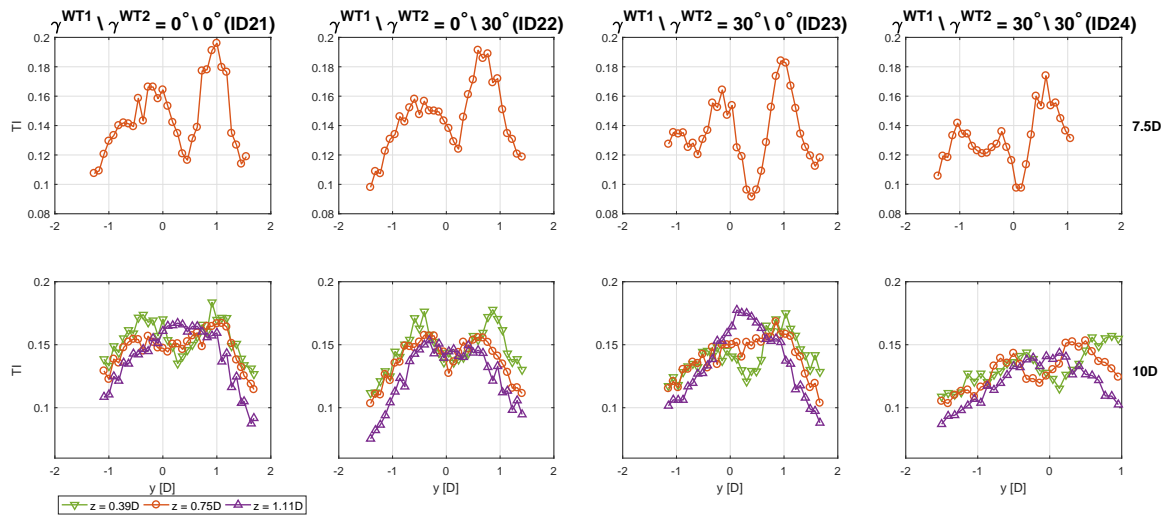
Figure 56. Turbulence intensity measurements along horizontal lines with laterally-shifted wind turbines, high-TI inflow conditions and for four different $\gamma^{WT1} \setminus \gamma^{WT2}$ combinations (ID 21-24).

5   INDIVIDUAL PITCH CONTROL EFFECTS ON LOADS AND WAKE SHED BY A MISALIGNED WIND TURBINE

5.1   Introduction

Individual Pitch Control (IPC) aiming at reducing the wind turbine loads has received a significant portion of attention in the scientific community in recent years [3, 8]. The main goal of individual pitch control is to reduce the first harmonic of the blade loads by introducing the additional blade pitch action on the same frequency. Obviously such control algorithm increases the blade pitch activity, but since the first loads harmonic is typically very emphasized, it can also significantly reduce the fatigue and prolong the wind turbine expected lifetime.

So far, the effectiveness of IPC in reducing loads has been proven numerically and in the field for wind turbines that are aligned with the wind speed. However, few studies have been conducted concerning the effectiveness of IPC on wind turbines that are strongly misaligned with respect to the wind direction. Moreover, it has not been investigated yet whether the wake shed by a misaligned wind turbine could be affected by IPC, as well as if the eventual effect could lead to benefit also at the level of the downstream wind turbine power productions and loads.

The research described within this chapter aims therefore at experimentally assess, by means of wind tunnel testing with scaled models, the effects produced by IPC algorithms on the loads and the wake shed by a misaligned wind turbine, as well as the impacts of IPC on the downstream wind turbine power productions and loads.

The chapter is therefore organized according to the following plan. First, the adopted IPC formulation and its implementation within the wind turbine models is presented in Section 5.2. Next, the experimental results are discussed in Section 5.3 followed by the conclusions, summarized in Section 5.4.

5.2   Individual Pitch Control: formulation and implementation

5.2.1   Wind turbine loads propagation

At first the coordinate systems, in which wind turbine structural loads are observed throughout the rest of the chapter, are introduced. A blade coordinate system is first defined in the blade root of each blade as shown in Fig. 57 (left) and it is rotating together with the blade, i.e. wind turbine rotor. The main sources of blade loads are aerodynamic effects, gravity and inertial loads, where aerodynamic and gravity loads have very pronounced oscillatory behaviour caused by rotation of the wind turbine rotor. Since the blade loads are propagated to the rest of the turbine, reduction of the blade loads significantly reduces the loads on other wind turbine components.

The rotating hub coordinate system has the same direction of the axes as the coordinate system of the first blade, but its origin is in the hub centre instead of the blade root, as shown in Fig. 57

(right). Since the rotating hub coordinate system is rotating with the same speed as blade coordinate systems, the misalignment among them are constant. Therefore the blade loads are propagated into rotating hub coordinate system as follows:

$$
\begin{aligned}
M_{r,y} &= \sum_{i=0}^{2} M_{y,i} \cos \frac{2\pi}{3} i - \sum_{i=0}^{2} M_{z,i} \sin \frac{2\pi}{3} i, \\
M_{r,z} &= \sum_{i=0}^{2} M_{z,i} \cos \frac{2\pi}{3} i + \sum_{i=0}^{2} M_{y,i} \sin \frac{2\pi}{3} i,
\end{aligned}
\tag{5.1}
$$

where $M_{y,i}$ and $M_{z,i}$ are blade loads in y and z axes of the ith blade coordinate system, $M_{r,y}$ and $M_{r,z}$ are resulting loads in the rotating hub coordinate system.

The fixed hub coordinate system is the same as the rotating hub coordinate system when the first blade is positioned vertically up (rotor azimuth $\vartheta = 0$). Therefore the loads in the fixed hub coordinate system can be expressed as:

$$
\begin{aligned}
M_{YN} &= M_{r,y} \cos \vartheta - M_{r,z} \sin \vartheta, \\
M_{ZN} &= M_{r,y} \sin \vartheta + M_{r,z} \cos \vartheta.
\end{aligned}
\tag{5.2}
$$

Since the rotor of the observed wind turbine is rotating in the clockwise direction, rotor azimuth angle is defined as positive in the same direction.

Note that (5.1) and (5.2) do not describe the complete loads on the hub, but only the propagation of the blade loads to the hub. There are additional load components on the hub, but since they are not of the main interest for the following explanation of the IPC formulation, they are not written here.
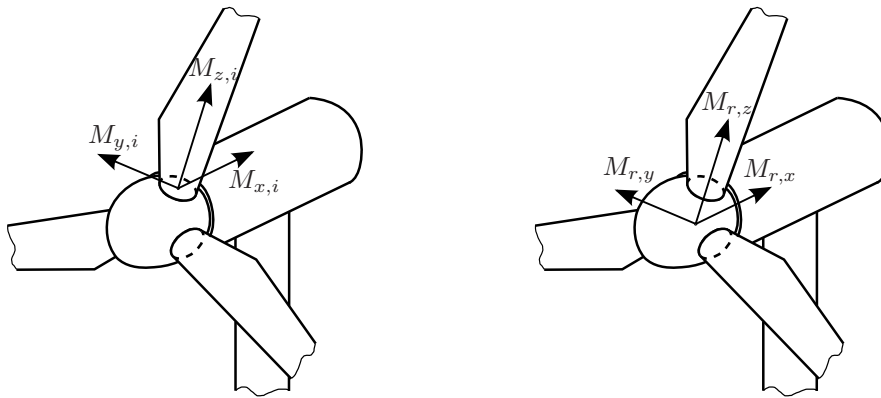
Figure 57. Structural loads in blade (left) and rotating hub (rigth) coordinate system.

5.2.2 Basic individual pitch control

Due to the rotation of the wind turbine rotor, the structural loads on the blades have emphasized periodic behavior, where the first harmonic (on the frequency 1p – once per revolution) is the most dominant. Therefore the main objective of the individual pitch control is to reduce the first har-

monic of the blade loads, which is expected to also reduce the mean value of the loads on the fixed wind turbine components (i.e. nacelle or tower). The individual pitch control as described in e.g. [3] is based on d-q transformation of the blade loads (where typically blade out-of-plane bending moments $M_{y,i}$ are used):

$$
\begin{aligned}
M_d &= \frac{2}{3} \sum_{i=0}^{2} M_i \cos \vartheta_i, \\
M_q &= \frac{2}{3} \sum_{i=0}^{2} M_i \sin \vartheta_i,
\end{aligned}
$$

(5.3)

where M_i is the blade load and ϑ_i is the azimuth position of the ith blade, while M_d and M_q are loads in d-q coordinate system. Such transformation extracts the information about the first blade loads harmonic, i.e. the mean value of the transformed loads represents the amplitude of the first blade loads harmonic. Therefore, two controllers in the transformed d-q coordinate system are used for reducing the mean of the transformed loads – one controller for each axis. The three blade pitch reference signals are then obtained by applying the inverse d-q transformation on the controller outputs and adding the collective pitch reference β_c defined by wind turbine rotor speed (i.e. power) controller:

$$
\beta_i = \beta_c + \beta_d \cos \left(\vartheta + \frac{2\pi}{3} i \right) + \beta_q \sin \left(\vartheta + \frac{2\pi}{3} i \right),
$$

(5.4)

where β_d and β_q are blade pitch references in the d-q coordinate system and β_i is the blade pitch reference of the ith blade.

Note that d-q transformation (5.3) has similar mathematical formulation as the propagation of the blade loads to the fixed wind turbine components (5.1) and (5.2). Therefore, the loads on the fixed wind turbine components can be used for individual pitch control instead of the transformed blade loads, as suggested in [3]. For instance, loads from fixed hub coordinate system can be used for individual pitch control, where the mean of such loads corresponds to the amplitude of the first blade loads harmonic.

Since the experimental model used for the tests described in the following is not equipped with blade root load sensors but only with shaft load sensors, it is quite clear that transformation of the measurements to fixed shaft coordinate system (5.2) would be convenient for the basic individual pitch control.

5.2.3   Proposed control algorithm

Using transformation (5.2), the control algorithm for reduction of higher loads harmonics based on shaft measurements can be implemented. The basic controller structure is shown in Fig. 58. The transformed loads are first subtracted of the gravity induced loads, than filtered and fed to two PI controllers which try to bring the mean value of the transformed loads (and hence the amplitude of the observed harmonic) to zero value.
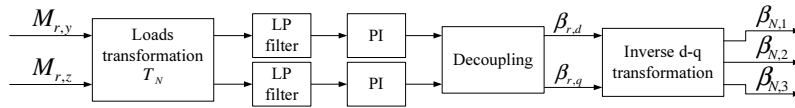
Figure 58. Control loop for reduction of 1P loads harmonic.

Namely, the axes in the transformed coordinate system are typically coupled. The amount of coupling depends on the time delays in the system (e.g. caused by blade pitch actuators) – slower dynamical system response, higher rotor speed and higher sample time generally increase the amount of coupling. The orientation of the measured loads can also have influence on the coupling. To solve this issue, it is sufficient to implement static decoupling (which actually causes decoupling on the frequency of observed harmonic in original coordinate system).

After the decoupling, the blade pitch references are obtained by using the inverse d-q transformation (5.4). Note that filtering of the transformed loads (see Fig. 58) limits the frequency bandwidth of each loads controller around the harmonic they are designed to reduce. Furthermore, the described controllers for load reduction will never change the collective pitch angle and therefore they will not interfere with wind turbine rotor speed control:

$$\frac{1}{3}\sum_{i=0}^{2} \beta_i = \beta_c. \qquad (5.5)$$

5.3 Results

5.3.1 Experimental setup

For the experimental demonstration of the effect of IPC on the loads acting on a yawed WT and its shed wake, scaled tests with two G1 models (see Deliverable 3.1), have been conducted in the boundary layer wind tunnel of the Politecnico di Milano, as shown in Fig. 59

The turbines have been operated at moderate (approx. 6%) turbulence intensity, while the ambient wind speed at hub height has been set to approx. 5.8m/s, i.e. just below rated wind speed. The two G1s have been installed aligned and at a downstream distance of 5D. The upstream wind turbine has been also yawed of $\pm 30°$, where a positive misalignment corresponds to a counter-clockwise rotation from the wind to the rotor axis looking down onto the terrain, while IPC has been executed on both the upstream and downstream wind turbine. Overall, 9 tests have been conducted, as reported in the following Table 4.

In order to properly understand the effect of the IPC running on the upstream WT on the performance (power/loads) measured on the second WT, the wake shed by the upstream WT with IPC on has been measured and compared to the wake shed by the same wind turbine with IPC off. To this aim, the wake of a single $\pm 30°$ yawed and unyawed wind turbine has been traversed, at a distance of 5D, at hub height and along a vertical line passing through the wake center. Two CTA hot wire

Figure 59. A G1 wind turbine scaled model running IPC algorithms for load reductions within the wind tunnel of the Politecnico di Milano.

Table 4. Test matrix of the conducted tests with IPC.

$\gamma^{WT1}[°]$	IPC-WT1	IPC-WT2
	OFF	OFF
30	ON	OFF
	ON	ON
	OFF	OFF
0	ON	OFF
	ON	ON
	OFF	OFF
-30	ON	OFF
	ON	ON

probes, assembled on the traversing system already described in Deliverable 3.1, has been used for the purpose.

The results are reported in the following. At first the effect of IPC running on the upstream WT on the upstream WT performance/loads/wake is discussed followed by the presentation of the effects produced by the IPC running on the upstream WT on the downstream WT performance/loads.

5.3.2   Effect of IPC running on the upstream WT on the upstream WT performance/loads/wake

At first, the effect of IPC running on the upstream wind turbine on its performance and pitch activity is presented in Fig 60. It is quite interesting to note that IPC seems to induce a modest gain in the power output for positive yaw misalignment, while a marginal and modest decrease is observed when the wind turbine is aligned to the wind direction and with a negative yaw misalignment, respectively. The observed small variations in the power output quite well agree with the measured changes at the level of the tip-speed-ratio λ, thus indicating that the measured power gain are not due to measurement or turbulence-induced noise. Concerning the pitch activity, the figure shows

that the activation of IPC leads to quite a substantial increase of the pitch actuator usage, as high-lighted by the values , observed for the actuator duty cycle (ADC). These latter, indeed, vary approx-imately linearly from 0.19 to 0.26 for $\gamma^{WT1} = 30°$ to $\gamma^{WT1} = -30°$. The figure also reports the amount of cyclic pitch pertaining to the d-q axis, where a positive value of $\beta_d = \beta_{tilt}$ means that the upward blade ($\vartheta = 0°$) is characterized by an higher pitch than the downward blade ($\vartheta = 180°$), while a positive value of $\beta_q = \beta_{yaw}$ means that a blade passing through the azimuthal position $\vartheta = 90°$ is characterized by an higher pitch than a blade passing through the azimuthal position $\vartheta = 270°$.
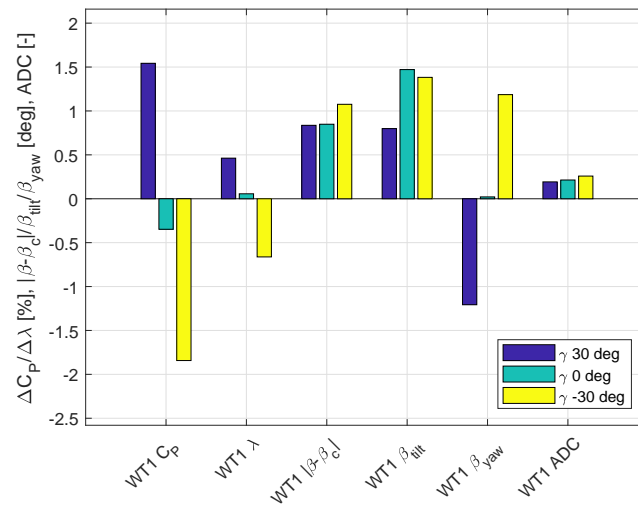
Figure 60. Effect of IPC running on the upstream wind turbine on its power output and pitch activity.

The bars depicted in the figure highlight that, for all the tested conditions, the IPC execution induced an higher upward blade pitch. This clearly highlights the effectiveness of the IPC in reducing the shear-induced tilt moment. Indeed, the airfoils along the upward blade produce higher out-of-plane forces than the airfoils of the downward blade due to sheared inflow, thus resulting in a non-null tilt moment M_{YN} in the fixed frame. Since the goal of the implemented IPC is to bring down to zero the mean value of the fixed-frame hub loads, the IPC demands for an higher upward blade pitch, which in turn leads to an overall reduction of the angle of attack experienced by the airfoils along the upward blade.

Fig 60 also reports that negative and positive values of $\beta_q = \beta_{yaw}$ are observed for $\gamma^{WT1} = -30°$ and $\gamma^{WT1} = +30°$, respectively, while a value almost close to zero is observed when the wind tur-bine model is aligned with the wind direction. In other words, the pitch of the blade sweeping upwind is increased when the wind turbine model operates under yaw misaligned conditions. These obser-vations well agree with the expected IPC behavior and the impact of yaw misalignment conditions on the rotor aerodynamics, which is described in Fig 61 reported in [5].

It is indeed known [5] that the asymmetry of the flow through a yawed rotor, caused by the flow expansion, implies that a blade sweeping upwind is characterized by an higher angle of attack than when it is sweeping downwind. The out-of-plane forces generated by the upwind blade upwind are,
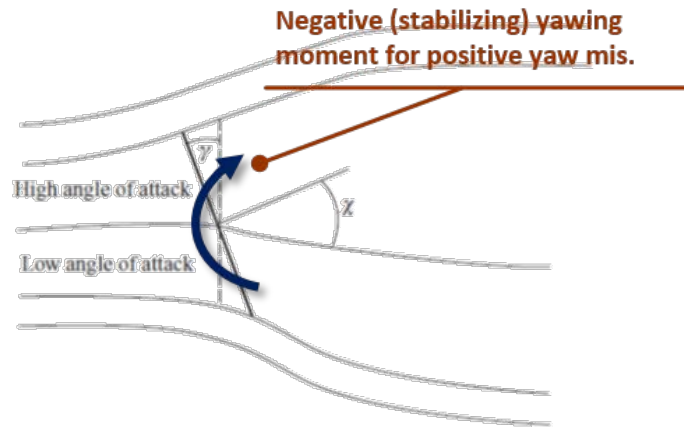
**Figure 61. Effect of yaw misalignment on the angle of at-
tack experienced by the upwind and downwind blade.**

therefore, greater than the ones produced by the downwind blade. It can therefore be seen that there is a net average moment about the yaw axis in a direction which will tend to restore the rotor axis to a position aligned with the wind direction. Since the goal of the implemented IPC is to bring down to zero the mean value of both the yaw and tilt fixed-frame hub moments, the IPC execution generates an higher pitch for the blade sweeping upwind, which in turn induces an overall reduction of the angle of attack experienced by the airfoils along the upwind blade, thus leading to a null yaw moment.
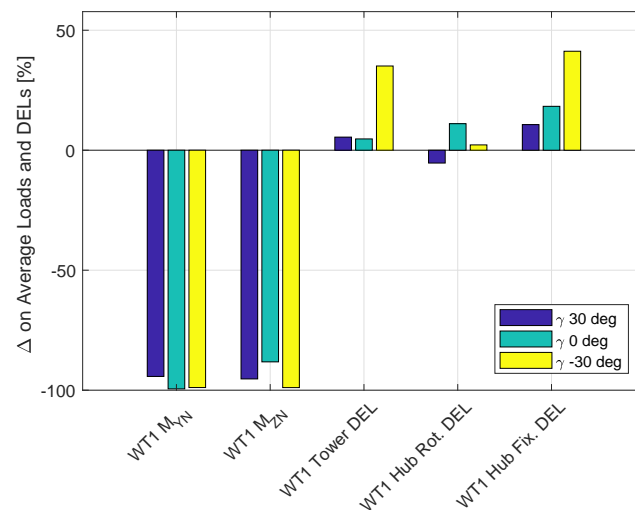
Figure 62. Effect of IPC running on the upstream wind turbine on its mean loads and DEL.

Fig 62 reports the difference, expressed in percent, between the mean fixed-frame hub tilt M_{YN} and yaw M_{ZN} moments measured with the IPC on/off, as well as the difference, again in percent and between IPC on/off, related to the damage equivalent loads (DELs) for the tower root and the rotating and fixed hub loads. These latter are computed, by means of rainflow counting, using the combined moment at the most damaged point of the tower root, rotating and not-rotating shaft

section, respectively. The bars in the figure highlight that the IPC is effective in almost completely eliminating the mean component of the fixed hub loads, as expected. However, the IPC seems not really effective in reducing the tower and hub fixed DELs, specially for negative yaw misalignment. Possible reasons for the increased DELs could be traced back to an improper setting of the IPC gains, which could lead to a too weak or too aggressive control if not properly tuned, or either to the effects that IPC could produce on a unbalanced rotor. The scaled models used for the testing, indeed, are characterized by a modest mass imbalance that induces 1-per-rev loads, on both the tower base and rotor shaft, which are amplified by the machine dynamics, namely the tower first mode. Since the rotational speed is affected by the the IPC, the loads due to the mass imbalance and their interaction with the machine dynamics is also affected by the IPC. Overall, this results in a complex effect of IPC on the DELs which would definitely require further understanding.
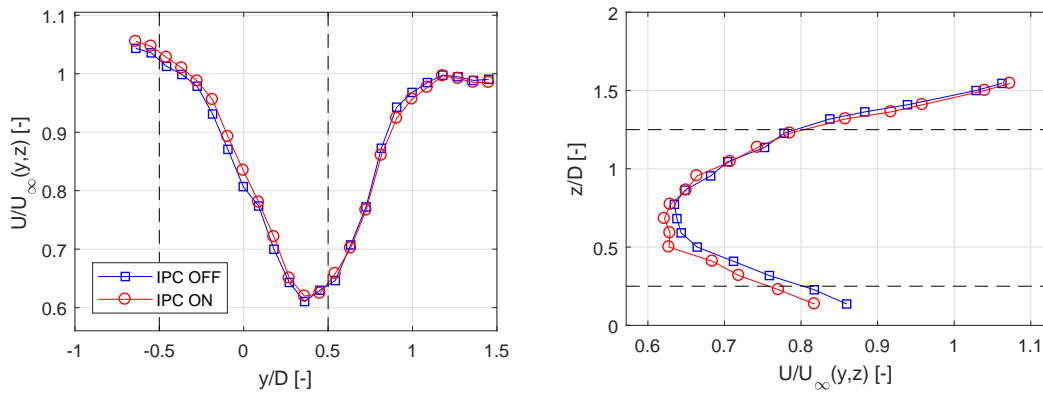
Figure 63. Average wake speed measured, with IPC on and off, along an horizontal line at hub height (left) and along a vertical line passing through the wake center (right) and with the upstream wind turbine operating with $\gamma^{WT1} = -30°$.

Once understood the effect of IPC running on the upstream WT on its performance and loads, the wake shed by the upstream WT operating with a yaw misalignment of -30 [deg] and with IPC on/off has been traversed at a downstream distance of 5D with respect to the machine rotor disk, i.e. in correspondence of the position where a second model has been located during experiments whose results are discussed in the following. The measured average wake speed is reported in Fig. 63, where for measurements along an horizontal line at hub height normalized velocities are reported on the y-axis, while the x-axis refers to the lateral distance from the rotor axis, expressed in rotor diameter. For measurements along a vertical line passing through the wake center, instead, normalized velocities are reported on the x-axis, while the y-axis refers to the distance of the measurement point from the ground, again expressed in rotor diameter. Similarly to the data shown in chapter 4, the average normalized flow velocity is obtained by computing the ratio between the average flow speed in the wake and the speed measured by a Pitot tube placed at hub height and 3 diameters upstream of the rotor. The plots in the right of Fig. 63, concerning the measurements along an horizontal line at hub height, highlight once more the wake displacement induced by the yaw misalignment, which seems however not that much affected by the IPC activation. On the other side, the figure clearly enhances which is the effect of the IPC running on the upstream model on its shed wake. Indeed, it is known

that the cyclic pitch control induces a velocity field within the wake that is far from symmetrical and characterized by a region of significantly lower speed on one side of the rotor disk, as discussed in [11]. A similar behavior can be noted also for the IPC, despite the magnitude of the observed wake asymmetry is lower than those discussed in [11]. Indeed, with the IPC activated the left side of the wake, i.e. the wake region whose deficit is mainly governed by the axial induction produced by the blade sweeping upwind, is characterized by a lower deficit. Moreover, a faster flow is observed within the upper wake, i.e. the one associated to the axial induction produced by the upward blade. On the other side, higher wake deficits are observed for the portion of the wake "generated" by the downward and downwind sweeping blades. These observation are due to the previously discussed effects of IPC on the pitch of the upwind/downwind sweeping blades, as well as on the pitch of the upward/downward blades. Indeed, the higher pitch for the upwind/upward blades enables a lower energy extraction from the flow passing through the related rotor disk portions, thus resulting in a lower wake deficit. On the other side, the lower pitch for the downwind/downward blades induces locally a stronger wake deficit.
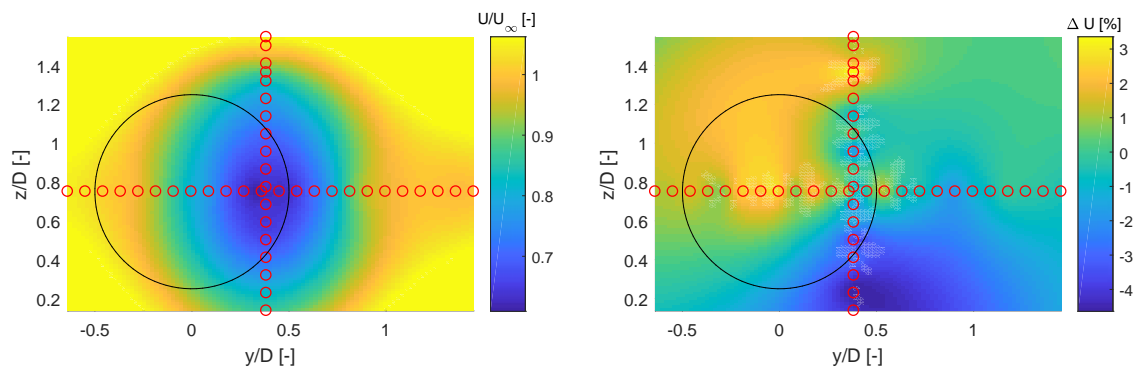
Figure 64. Average wake speed with IPC off (left) and difference between the average wake speed with IPC on and IPC off (right) on a vertical plane and with the upstream wind turbine operating with $\gamma^{WT1} = -30°$.

In order to quantify which could be the impact, on the downstream machine power/loads, produced by the observed wake speed changes due to IPC running on the upstream wind turbine, the wake deficit on a vertical plane, shown in Fig. 64 (right) with IPC off, has been reconstructed using the available wake profiles and by means of biharmonic spline interpolation provided by the *griddata* function of Matlab. Fig. 64, on the right, depicts the difference ΔU, expressed in percent, between the reconstructed average wake speed with IPC on/off, with the upstream wind turbine operating with $\gamma^{WT1} = -30°$. The figure, which also shows the machines rotor disk and the points were the flow in the wake has been sampled (red dots), highlights that the speed in the wake is increased in the upper-left region and decreased in the bottom-right one. However, the important feature to highlight is that the downstream wind turbine is expected to be impinged by a faster flow when the IPC on the upstream machine is activated. In details, an increase of approx. 0.8% is obtained by computing the average of ΔU within the rotor disk of the downstream wind turbine. Considering the standard cubic relationship between power and wind speed for a wind turbine operating in region

II, it is expected that IPC executed on the upstream machine misaligned of -30 [deg] with respect to the wind direction will lead to a power increase of approx. 2.5% on the downwind machine.
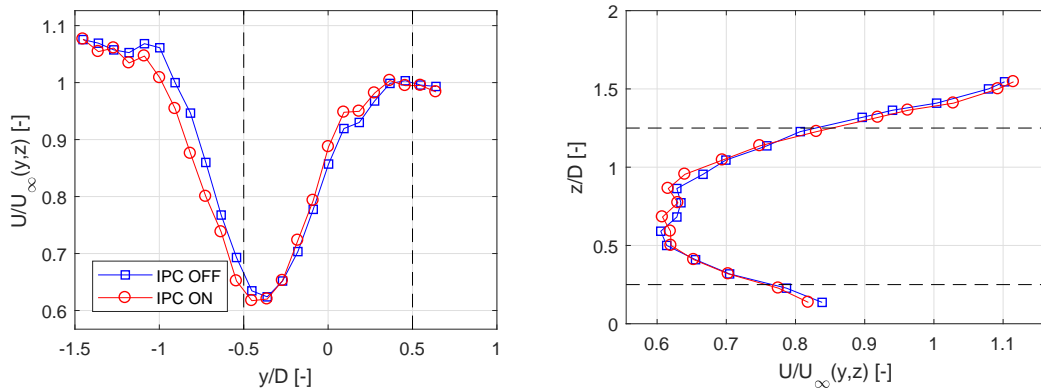
Figure 65. Average wake speed measured, with IPC on and off, along an horizontal line at hub height (left) and along a vertical line passing through the wake center (right) and with the upstream wind turbine operating with $\gamma^{WT1} = 30°$.

The wake shed by the upstream WT operating with a yaw misalignment of +30 [deg] and with IPC on/off was also traversed, and the measured wake profiles along an horizontal and vertical line are depicted in Fig. 65. Similarly to the case with $\gamma^{WT1} = -30°$, the figure highlights the effect of the IPC running on the upstream model on its shed wake. Indeed, it is again observable the lower deficit within the portion of the wake generated by the blade sweeping upwind. On the other side, when comparing the effect of IPC on the deficit of the wake region generated by the downward blade with $\gamma^{WT1} = -30°$ and $\gamma^{WT1} = +30°$, it is possible to note the IPC has a lower impact for this last case. This confirms the observations, reported in Fig. 60, about the IPC-demanded β_{tilt} for the tested yaw misalignment. Indeed, β_{tilt} is lower for $\gamma^{WT1} = +30°$ than for $\gamma^{WT1} = -30°$, thus resulting in a lower impact of IPC on the deficit of the wake region generated by the downward blade.
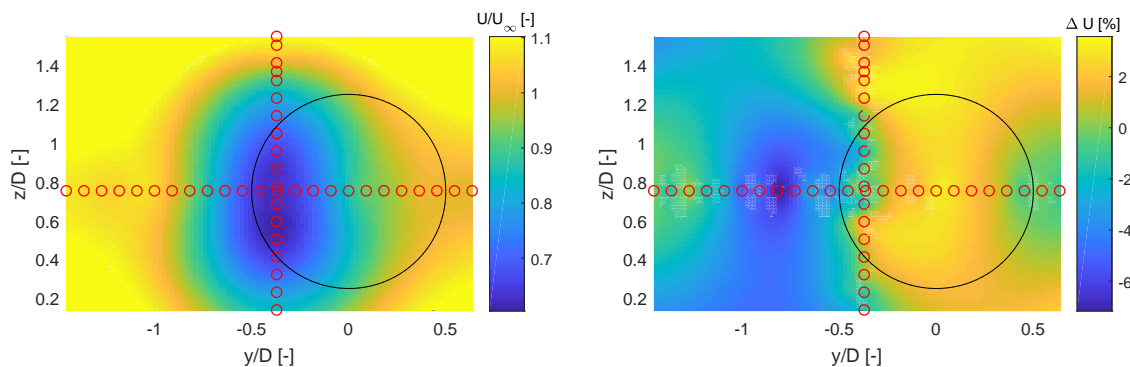
Figure 66. Average wake speed with IPC off (left) and difference between the average wake speed with IPC on and IPC off (right) on a vertical plane and with the upstream wind turbine operating with $\gamma^{WT1} = 30°$.

In order to assess the impact of IPC on the downstream machine power/loads, the wake deficit on a vertical plane has again been reconstructed using the available wake profiles, as shown in Fig. 66
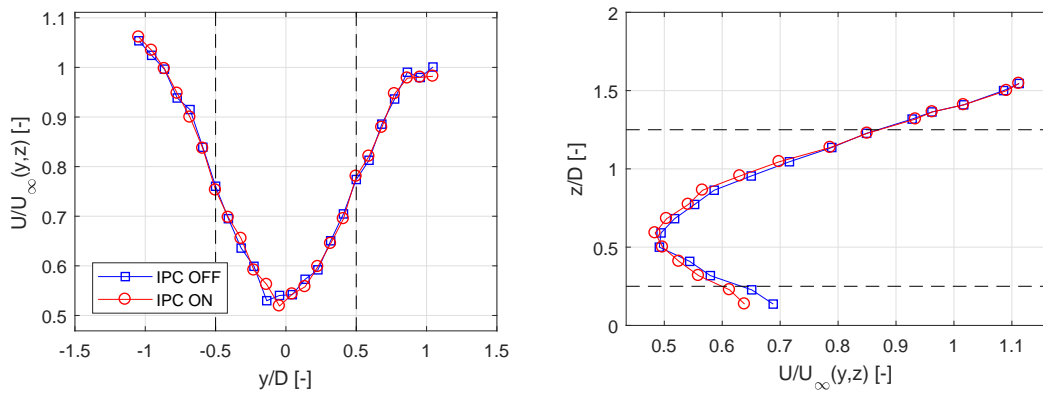
Figure 67. Average wake speed measured, with IPC on and off, along an horizontal line at hub height (left) and along a vertical line passing through the wake center (right) and with the upstream wind turbine operating with $\gamma^{WT1} = 0°$.

on the left and with IPC not active. Based on the resulting difference ΔU between the reconstructed average wake speed with IPC on/off, shown in Fig. 66 on the right, it is expected that IPC running on an upstream wind turbine misaligned of +30 [deg] would lead to an increases of approx. 1.8% on the average rotor disk speed sensed by an aligned downstream wind turbine, thus leading to a power increase of approx. 5.5%. This latter gain is considerably higher that the one expected with the upstream machine misaligned of -30 [deg] with respect to the wind direction. It is reasonable to trace back this difference to the lower IPC-demanded β_{tilt} observed with the 30 [deg] misaligned wind turbine.
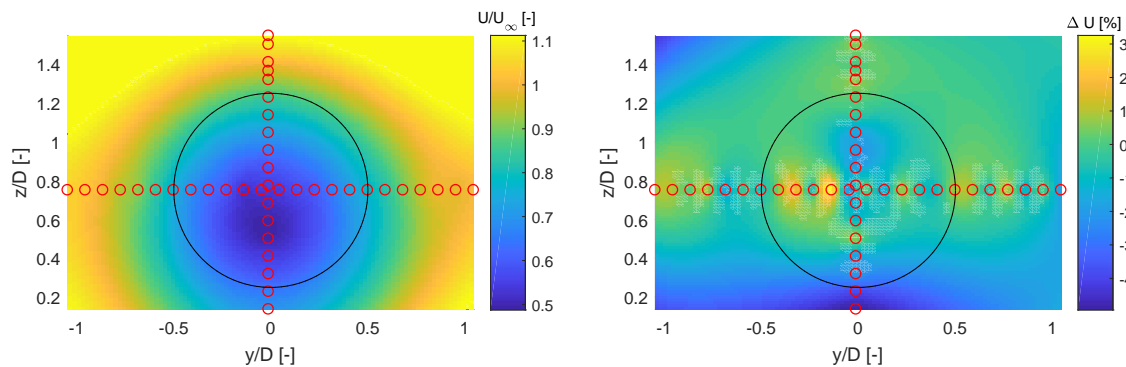
Figure 68. Average wake speed with IPC off (left) and difference between the average wake speed with IPC on and IPC off (right) on a vertical plane and with the upstream wind turbine operating with $\gamma^{WT1} = 0°$.

Finally, the measured deficit of the wake shed by the upstream aligned WT and with IPC on/off is reported in Fig. 67. The plotted data confirm the results presented in Fig. 60: since $\beta_{yaw} = 0°$ for $\gamma^{WT1} = 0°$, almost no variation is observed for the wake deficit at hub height with IPC on/off, while IPC has some effect on the vertical wake profile due to $\beta_{tilt} > 0°$. The difference ΔU between the reconstructed average wake speed with IPC on/off is than presented in Fig. 68, on the left, while the same figure reports, on the right, the reconstructed wake deficit with IPC off. By looking at the figure,

it immediately stands out the difference with respect to the data plotted in Figs. 66 and 64. Indeed, it is not visible a region of the wake where the speed is increased due to IPC; it seems, instead, that the speed in the wake is overall reduced. This is expected to lead to a decrease of the downstream rotor average incoming flow speed of approx. 0.85%, which should imply a power decrease of approx. 2.6%.

5.3.3 Effect of IPC running on the upstream WT on the downstream WT performance/loads

Once measured the effect of IPC running on the upstream wind turbine on its loads and shed wake, experiments with a second G1 model placed 5D downstream of the first one were performed. In details, several tests were conducted with the IPC on/off on the first turbine, with the goal of evaluating the impact of IPC on the power and loads of the downstream wind turbine. The experimental findings, reported in Fig. 69, unfortunately do not include, due to a failure in recording some sensors data, results related to the case with the upstream wind turbine aligned with the wind speed ($\gamma^{WT1} = 0°$).
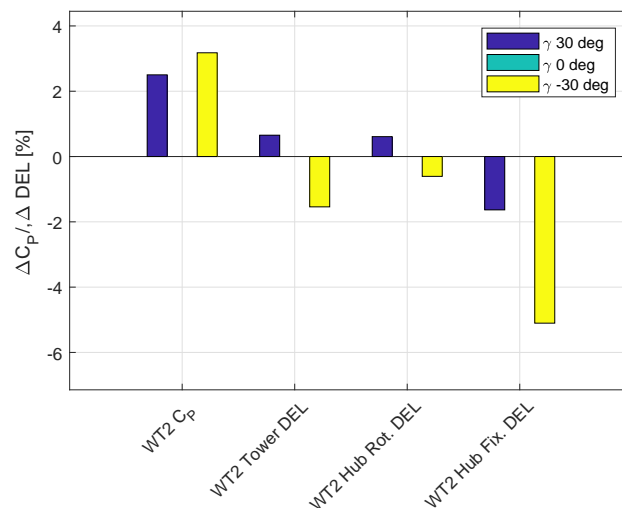
**Figure 69. Effect of IPC running on the upstream wind turbine on
the power output and loads of the downstream wind turbine.**

Particularly interesting are the increments of 3.1% and 2.5% for the power coefficient on the downstream wind turbine due to the activation of the IPC on the upstream machine respectively yawed of -30 and +30 [deg]. They indeed qualitatively agree with the expectations based on wake data analysis, which were found equal to 2.5% and 5.5% for $\gamma^{WT1} = -30°$ and $\gamma^{WT1} = +30°$, respectively. However, the power increase derived from the wake data and with $\gamma^{WT1} = +30°$ is higher than the measured one. Possible explanation of this difference could be related to the way the wake deficit, shown in Fig. 65 on the right, has been reconstructed on a vertical plane by using the available wake profiles. This reconstruction, indeed, is incapable of capturing the specific kidney-shape of the wake shed by yawed wind turbines [11], a fact that could lead to an inaccurate estimation of the average rotor speed and therefore to an imprecise estimation of the power output with IPC on/off.

Fig. 69 also reports the effect of IPC running on the upstream wind turbine on the DELs for the tower root and the rotating and fixed hub loads of the downstream wind turbine. The results highlight almost negligible effects on the tower and rotating hub DELs, while a modest decrease is observed for the fixed hub DELs.

5.3.4 Effect of IPC running on the downstream WT on the downstream WT performance/loads

The final experimental tests were conducted with the goal of measuring the effect of IPC executed on an aligned downstream wind turbine ($\gamma^{WT2} = 0°$) on its power and loads. Similarly to the results presented in the previous section, the experimental findings unfortunately do not include data obtained with the upstream wind turbine aligned with the wind speed ($\gamma^{WT1} = 0°$). At first, the effects of IPC on the power and the pitch activity is presented in Fig 70. It is quite interesting to note that IPC executed on the downstream wind turbine generates a much higher decrease of the power output than the IPC executed on the upstream aligned machine ($\gamma^{WT1} = 0°$). This observation can be explained if one looks at the pitch activity induced by the IPC and, specifically, to the values of the mean absolute deviation (MAD), indicated with $|\beta - \beta_c|$ on the x-axis label, where β is the blade pitch of a blade and β_c the collective pitch. The MAD, indeed, is strongly correlate to the loss of power associated to the activation of IPC on a wind turbine that operates in partial load conditions (region II): as higher is the deviation of the pitch from the region II optimum (β_c), as longer is the time a wind turbine operates under sub-optimal conditions ($\beta(t) \neq \beta_c$), and therefore as higher is the power loss. The reported values of MAD, equal to 1.5 and 1.95 [deg] respectively for $\gamma^{WT1} = 30°$ and $\gamma^{WT1} = -30°$, are indeed remarkably higher than the related ones presented in section 5.3.2 with the IPC running on the upstream machine. High values of the mean absolute deviation have also an impact on the actuator duty cycles (ADCs). These latter, equal to 0.35 and 0.44, are also remarkably higher than the ones measured with the IPC running on the upstream machine.
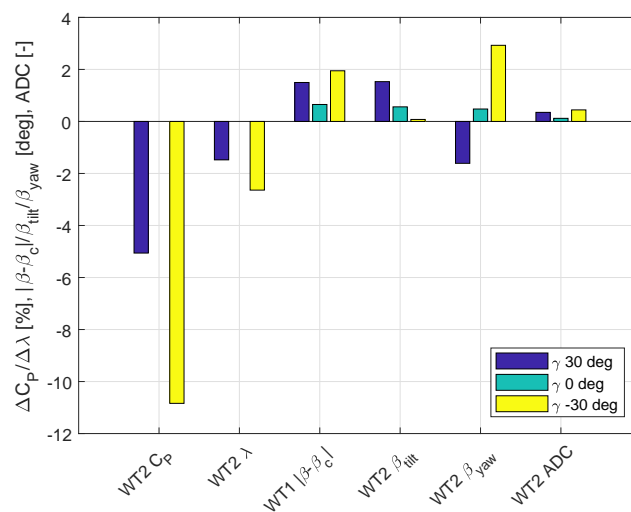
Figure 70. Effect of IPC running on the downstream wind turbine on its power output and pitch activity.

In order to better understand the reason behind the high pitch activity required by the IPC running on the downstream machine, it is convenient to look at the amount of cyclic pitch for the d-q axis, also reported in Fig 70. The bars depicted in the figure show that the cyclic pitches $\beta_d = \beta_{tilt}$ and $\beta_q = \beta_{yaw}$ varies with the yaw misalignment of the upstream wind turbine. In particular, β_{yaw} is positive when $\gamma^{WT1} = -30°$ and negative when $\gamma^{WT1} = +30°$. Moreover, β_{tilt} is positive and is almost proportionally increasing with γ^{WT1}.

Table 5. Coefficient of the first order polynomial that best-fit the flow field that impinges the upstream and downstream wind turbine, together with the cyclic pitches measured for the upstream and downstream machine.

	p_0	p_y	p_z	β_{tilt}^{WT1} [deg]	β_{yaw}^{WT1} [deg]	β_{tilt}^{WT2} [deg]	β_{yaw}^{WT2} [deg]
Inflow	0.998	0.0183	0.205	1.47	0.02		
$\gamma^{WT1} = -30°$	0.85	-0.513	0.063	-	-	0.077	2.93
$\gamma^{WT1} = 0°$	0.65	0.0042	0.2957	-	-	0.56	0.48
$\gamma^{WT1} = +30°$	0.855	0.514	0.086	-	-	1.53	-1.61

Given that the spatial not-homogeneity of the sheared inflow was the cause of the not-null β_{tilt} observed with the aligned upstream machine ($\gamma^{WT1} = 0°$), it is interesting to understand if the observed cyclic pitches could be explained by looking at the spatial not-homogeneity of the flow field that impinges the downstream wind turbine. To this aim, the non-dimensional reconstructed flow field (see Figs. 64-66-68) measured within the rotor disk area has been best-fitted with the following first order bi-dimensional polynomial

$$U(y/D, z/D)/U_\infty = p_0 + p_y \cdot y/D + + p_z \cdot (z - z_H)/D, \qquad (5.6)$$

where z_H is the hub height.

The resulting coefficients are reported in Table 5, which also includes the coefficient of the polynomial that best-fits the upstream shared inflow and the cyclic pitches measured for the downstream wind turbine ($\beta_{tilt,yaw}^{WT2}$) and for the aligned upstream machine ($\beta_{tilt,yaw}^{WT1}$). Based on the reported polynomial coefficients p_z, that indicates the amount of spatial not-homogeneity along the vertical direction, it should be expected that β_{tilt} is maximum when the IPC is activated on the downstream machine and $\gamma^{WT1} = 0°$, while it should be modest when $\gamma^{WT1} = -30°$ and $\gamma^{WT1} = +30°$. Moreover, based on the polynomial coefficients p_y, that quantifies the amount of spatial not-homogeneity along the horizontal direction, β_{tilt} should be maximum and approx. equal in magnitude for $\gamma^{WT1} = -30°$ and $\gamma^{WT1} = +30°$, while it should be almost null for both the upstream and downstream wind turbine with $\gamma^{WT1} = 0°$.

These expectation are however different than the measured cyclic pitches, as highlighted by Table 5. Possible explanation could again be related to the fact that the used wake deficit, estimated from wake profiles measured along a vertical and horizontal line, is not capturing the specific kidney-shape of the wake shed by yawed wind turbines. Another possibility could be due to the effect produced by the interaction of the downstream turbine induction zone with the impinging wake, which could

affect the spatial not-homogeneity of the impinging flow. More analysis, also supported by CFD simulations, should be conducted to better understand the phenomena.
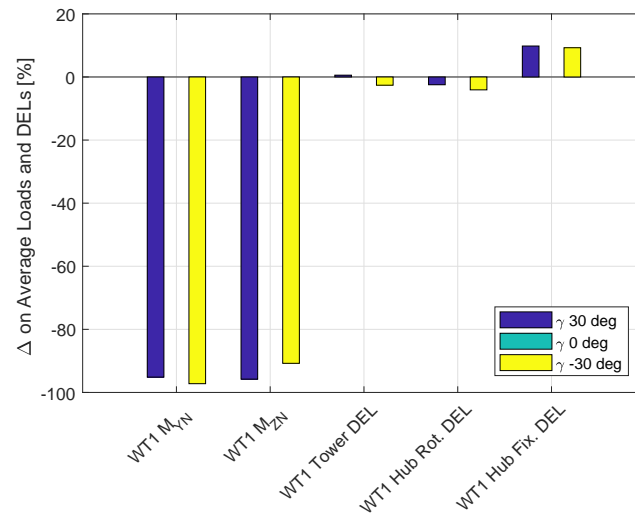
Figure 71. Effect of IPC running on the downstream wind turbine on its mean loads and DEL.

Fig. 71 reports the difference, expressed in percent, between the mean fixed-frame hub tilt M_{YN} and yaw M_{ZN} moments measured with the IPC on/off, as well as the difference related to the damage equivalent loads (DELs) for the tower root and the rotating and fixed hub loads. Similarly to the observations related to the effect of IPC running on the upstream machine on its loads, IPC running on the wake-impinged downstream wind turbine is effective in almost completely eliminating the mean component of the fixed hub loads. The IPC seems to also generate a modest reduction of the the tower and hub rotating DELs, while the hub fixed DELs are increased by the activation of IPC. Possible reasons could again be traced back to an improper setting of the IPC gains.

5.4   Conclusions

The effectiveness of IPC in reducing fixed-frame mean loads on wind turbines that are strongly mis-aligned with respect to the wind direction, or even partially impinged by the wake shed by an up-stream wind turbine, has been proven experimentally by means of wind tunnel testing conducted within the project. Moreover, it was assessed that the wake shed by a misaligned wind turbine is affected by IPC, a fact that could lead to modest increase, in order of few percent, of the downstream wind turbine power production.

However, the tested IPC did not prove to be effective in reducing DELs for all the sensed components, i.e. tower root and fixed-rotating shaft. A possible explanation could be an improper setting of the IPC gains or even the combination of IPC and rotor mass unbalance. Further testing should be conducted in this sense.

6 TESTING OF A STATE UPDATE METHOD

6.1 Introduction

In this chapter the results of a wind tunnel testing campaign conducted in February 2018 are presented. The goal of the experiments was to verify, by means of wind tunnel testing, the effectiveness of the state update method described in Deliverable 2.2 and validated, by means of CFD simulations, in Deliverable 3.3, as well as to address the potential of such a method once applied in support of closed-loop wind farm control algorithms.

The method is first briefly explained in section 6.2, while the experimental results are presented in section 6.3. Finally, the conclusions and the future activities are discussed in section 6.4.

6.2 State update method: formulation

The state update method described in Deliverable 2.2 utilizes the sector effective wind speed estimator, whose goal is estimating the local wind speed at each turbine blade by using measurements of the rotor loads. As the blades rotate within the rotor disc, the wind speed in different rotor disc sectors, usually two lateral and two vertical sectors, can be inferred. By comparing these local flow speed estimates to those predicted by a control oriented wind farm flow model like FLORIS (described in Deliverable 1.2), it is possible, as long as the wake is impinging on a downstream turbine rotor, to correct the modeled wake lateral position. In case of a relatively full wake impingement, which leads to wind speed changes in both lateral sectors of the downstream turbine, it is also possible to estimate the wake speed or deficit magnitude. Further turbine measurements, i.e. turbine power or rotor effective wind speed, can additionally improve the wake correction.

To ease the readability of this chapter, some variables are resumed in the following. In details, the state update method computes the model outputs

$$y = \begin{bmatrix} P_{\text{WT2}} \\ V_{\text{WT2}}^{\text{SE,right}} \\ V_{\text{WT2}}^{\text{SE,left}} \end{bmatrix} \tag{6.1}$$

where P_{WT2} is the FLORIS predicted power of the downstream wind turbine and $V_{\text{WT2}}^{\text{SE,left/right}}$ the left or right (looking downstream) sector effective wind speed. The corresponding filtered measurements – i.e. the sectors effective wind speed estimated by means of wind turbine rotor loads – are

$$z = \begin{bmatrix} P_{\text{WT2,exp}} \\ V_{\text{WT2,exp}}^{\text{SE,right}} \\ V_{\text{WT2,exp}}^{\text{SE,left}} \end{bmatrix}, \tag{6.2}$$

where a second order Butterworth filter, with cut-off frequency of 0.25Hz, has been employed. Through optimization, the upstream turbine's wake state update

$$\hat{x} = \begin{bmatrix} d_{\mathrm{WT1}} + e_{\mathrm{d}} \\ u_{\mathrm{WT1}} + re_{\mathrm{u}} \end{bmatrix} \tag{6.3}$$

is computed where d_{WT1} is the upstream turbine's lateral wake position and e_{d} the identified error, while u_{WT1} is the upstream turbine's wake velocity, e_{u} the identified deficit error and r a wake reduction factor. The effect of wake position and deficit error on the modeled flow field is exemplary shown in Fig. 73.

6.3   Results

6.3.1   Experimental setup

For the experimental demonstration of the state update method, scaled tests with two G1 models (see Deliverable 3.1), have been conducted in the boundary layer wind tunnel of the Politecnico di Milano, as shown in Fig. 72
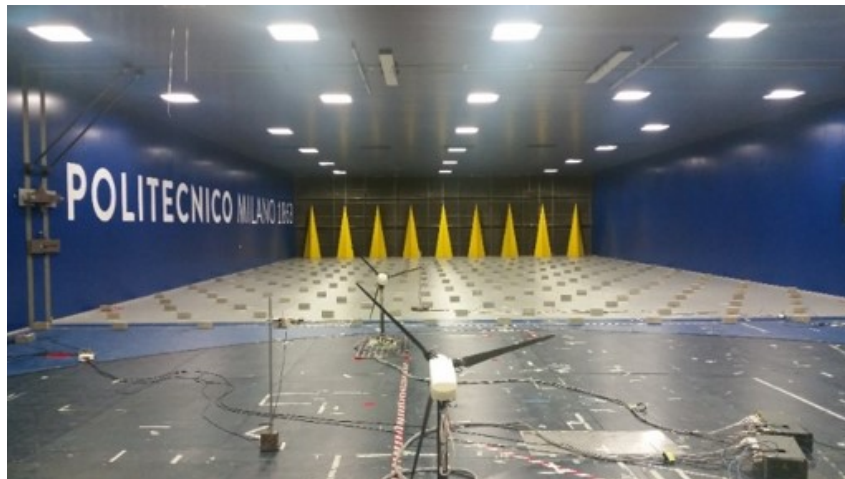
Figure 72. A cluster of two G1 wind turbine scaled models within the wind tunnel of the Politecnico di Milano.

The turbines have been operated at moderate (approx. 5%) turbulence intensity. The ambient wind speed at hub height has been set in most experiments to approx. 5.8m/s which corresponds to a wind speed just below rated wind speed. The two G1s have been installed in tree different layouts achieved by properly rotating the turntable: aligned, and ± 0.2 diameter (D) laterally displaced. In all experiments the downstream distance between the turbines is approx. 5D. Figure 74 shows a visualization of the flow field predicted by FLORIS for the three tested layouts, where Δy is the lateral turbines offset.
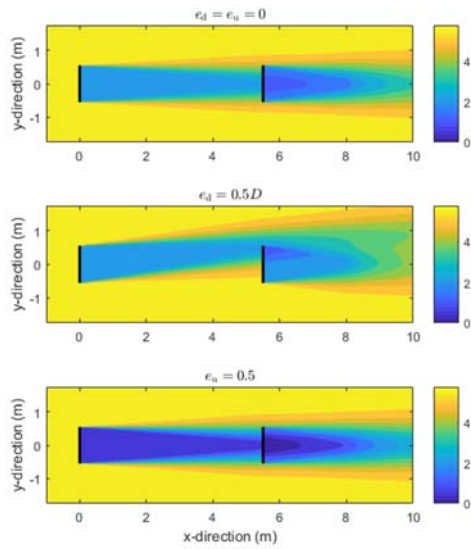
Figure 73. Top view of the flow field within a cluster of two wind turbines and for different wake state errors.
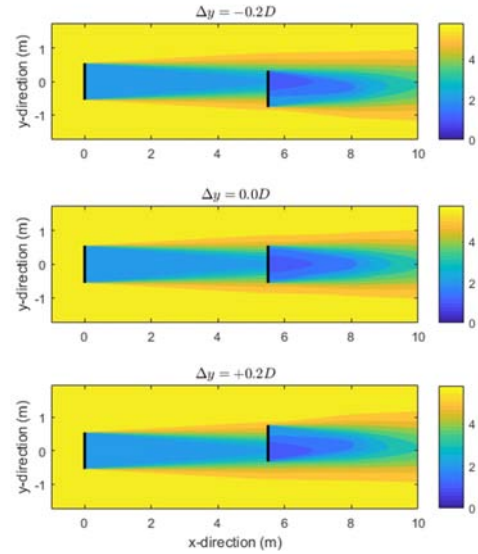
Figure 74. Top view of the flow field within a cluster of two turbines and for the tested layouts.

The control system of each wind turbine model, described in Deliverable 3.1, was enriched by a sector effective wind speed estimator, while a supervisory application, that runs the state update method, was executed on a standard Desktop PC. As shown in Figure 75, the sector effective wind speed estimator is implemented on the real-time Bachmann M1 controller at each turbine and executed at a frequency of 250 Hz, thus providing new estimates of the sector effective wind speed, as well as the related filtered values, every 4ms. On the supervisory PC, a Matlab instance is run. A script creates a Modbus object and every 2s data are pulled through TCP/IP from the individual turbines. The data consist of filtered rotor effective and horizontal sector effective wind speed estimates. In addition, the turbine yaw angle, air density and the Bachmann time, expressed in microseconds, are transferred through the same protocol. The state update method is executed at the same frequency, i.e. every 2s, providing a correction on wake position and deficit for the underlying wind farm model. Finally, the yaw angle of each wind turbine model can also be varied by the supervisory application, thus mimic a wind farm controller. Despite the supervisory application was not running in hard real-time, basically due to delays induced by the TCP/IP communication, it is expected that this will not generate relevant consequences on the proper execution of future wind farm control strategies.

The FLORIS model (see Deliverable 1.2) was adopted as underlying wind farm model for the state update method experiments. The original parametrization of the Porte-Agel wake model, again described in Deliverable 1.2, has been used, with the only exception of the lateral wake displacement parameters that govern the null yaw-misalignment, which have been set equal to zero ($a_\mathrm{d} = b_\mathrm{d} = 0$). As the state update method involves an high number of model evaluations, the computational speed has been increased by computing the wind farm flow velocities at each turbine rotor using a Cartesian grid with 15x15 points.
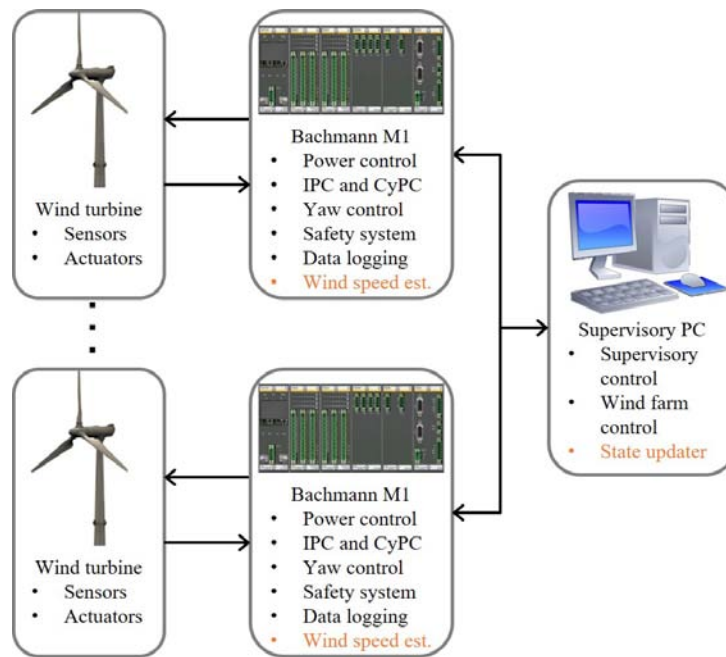
Figure 75. Wind farm control system enriched by a sector effective wind speed estimator and the state updater.

Moreover, the input turbulence intensity to the FLORIS model has been set equal to 5%, i.e. the one experienced in the wind tunnel. During all the experiments, the wind direction has been set to 0 degrees and the turbines cluster layout has been set according to the given experimental test case. The input ambient wind speed has been identified using the upstream turbine rotor effective wind speed $V_{\mathrm{WT1}}^{\mathrm{RE}}$, in turn estimated by solving the torque balance equation. In case of a turbine operated with a yaw misalignment angle γ, the rotor effective wind speed estimation is corrected by the yaw correction factor $f = cos(\gamma)^{-p_{\mathrm{P}}/3}$, where $p_{\mathrm{P}} = 2.174$ is the power loss coefficient of the yawed G1 turbines. To take wake propagation delays into account, the measurements of the upstream turbine are also delayed by one time step (2s).

6.3.2 Extrapolation of model corrections to different operating conditions

In this subsection, it is first assessed whether wake state errors identified in non-yawed conditions could lead to improvements in the FLORIS model predictions for conditions where the upstream turbine is yawed. In other words, for a specific upstream turbine yaw misalignment and wind direction (in the given experiments different wind direction are simulated by changing the turbines cluster layout) the wake position and deficit errors will be identified using the state update method and it is verified if those wake errors are also applicable for different yaw misalignment.

To test the described hypothesis, experiments in moderate turbulent inflow and without lateral turbine displacement $\Delta y = 0\mathrm{D}$ have been conducted. Figure 76 shows, in the first subplot, the prescribed upstream turbine yaw orientation. During the gaps in the following subplots the yaw maneuvers (dotted line) took place. The second and third subplots show the measurements (solid lines)
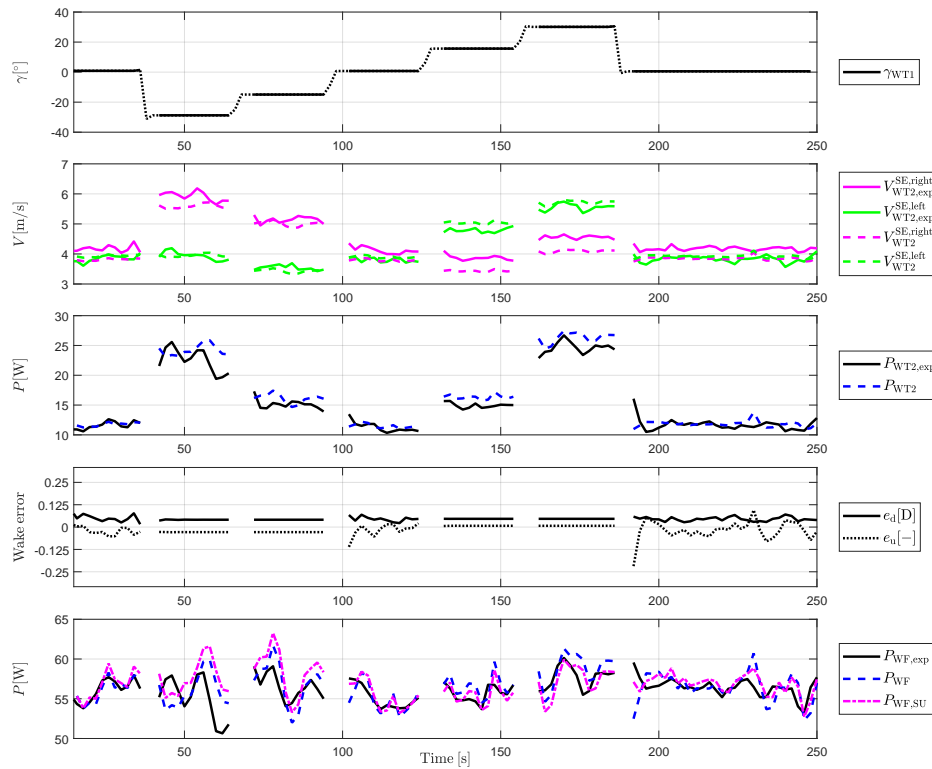
Figure 76. State update in wind tunnel experiment with upstream turbine yaw maneuvers.

and corresponding baseline model outputs ($e_d = d_u = 0$, dashed lines). The differences represent the mismatch between baseline model and measurements. By minimization, the state errors e_d and e_u are identified and shown in the fourth subplot. Following the hypothesis, the state errors are only identified if $\gamma_{WT1} = 0°$. In case $\gamma_{WT1} \neq 0°$ an average of the last three state error estimates is taken. Finally the last subplot of Figure 76 shows the value of three total cluster powers: the experimentally measured one ($P_{WF,exp}$), the one estimated by the baseline model (P_{WF}) and the one estimated by the FLORIS model updated with the state error ($P_{WF,SU}$).

The results show a good correlation between the modeled and the experimental turbines cluster power if $\gamma_{WT1} = 0°$, while in the other cases the baseline model, as well as the updated model, have significant bias. The state update is partially even providing worse results than the baseline model. This suggests that, at least for small model mismatches, the wake error in non-yawed conditions cannot be directly employed in yawed conditions.

As the identified wake state errors are relatively small, artificial model mismatch is imposed to test whether, in case of larger plant-model mismatch, the state update method can provide improved results. Figure 77 shows, for the same experimental conditions discussed so far, the identified state errors and total power for three different imposed plant-model mismatches (see subplot titles). The first and second plant-model mismatches are imposed by changing the wake model parameter a_d, that describes the wake deflection induced by wake rotation (see Deliverable 1.2, p. 72), by $\pm 0.2D$,
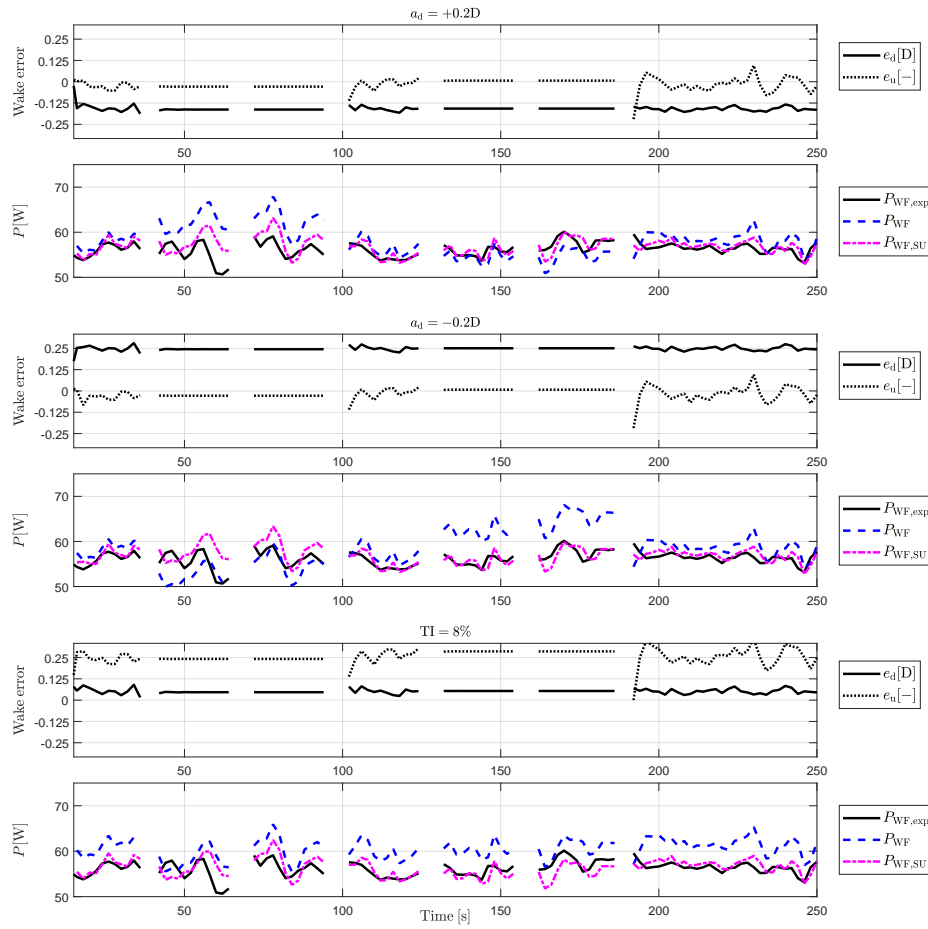
Figure 77. State update with artificially imposed plant-model mismatches.

which can be also interpreted as a wrongly measured wind direction affected by an error $\pm 2.3°$. The third plant-model mismatch is imposed by increasing the model input turbulence intensity from 5% to 8%, which would correspond to the high turbulence experiments.

The results in Fig. 77 show that the imposed plant-model wake position mismatch is detected by the state update method (e_d is shifted by $\approx \pm 0.2\text{D}$ in the first and second wake error subplot). For yaw misalignments where the baseline model has larger turbines cluster power estimation bias, the state update method shows a significant improvement. However, for some yaw misalignments the state update method slightly worsens compared to the baseline model. In case of a larger turbulence intensity (third model mismatch) the identified wake deficit error increases as expected (third wake error subplot) and the baseline model erroneously predicts a significantly increased total power (last subplot). The state update method is able to correct for the input error in turbulence intensity and a significant improvement through all yaw misalignments can be observed.

Summarizing these results, it can be stated that for smaller model mismatches the wake errors obtained by the state update method in non-yawed conditions do not provide improvements in conditions where the upstream turbine is yawed. However, for larger model mismatches the state update method provides improvement in the turbines cluster power estimation, with the most significant improvements achieved in case of a plant-model mismatch concerning the ambient turbulence intensity.

6.3.3 Alternative use of the state update method: look-up tables

The previous section showed that an identified wake error is valid mostly for the given configuration (yaw angle) and an extrapolation to other configurations is only improving the model estimates in case of significant model mismatch.

Therefore, in this section an alternative use of the state update method is tested. To this aim, a proper look-up table is first filled with identified state errors for a given configuration, i.e. a given wind direction (equivalent to the cluster layout in our experiments) and upstream turbine yaw misalignment. Firstly, three experiments with a prescribed upstream turbine yaw misalignment function (as shown in Figure 76) are conducted and the wake state error is identified in each configuration at each time step. If $\Delta y = \pm 0.2D$ and if the wake is steered away from the downstream turbine, the observability of both wake states might not be given anymore, therefore in those cases the previously estimated wake deficit is kept. The resulting average state errors are stored in a look-up table as function of wind direction and upstream turbine yaw misalignment. In practice, a more sophisticated method that would make use of forgetting factors or a neural network could be utilized. Moreover, the method could be easily extended to update the look-up table online during operation. Figure 78 shows the identified wake position error (left subplot) and deficit error (right subplot) as function of upstream turbine yaw misalignment for each lateral displacement.
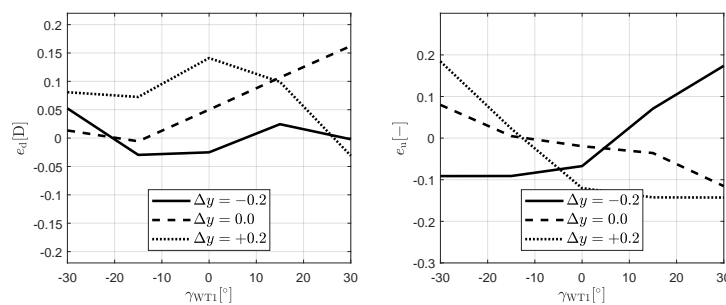
Figure 78. Identified look-up table for wake position error e_{d} and wake deficit error e_{u}.

Clearly, by applying the identified look-up table on the same experimental results, the updated wake model provides significantly better turbines cluster power predictions ($P_{\mathrm{WF,SU\ (LUT)}}$) than the baseline model (P_{WF}), as shown in Fig. 79. Note that for $\Delta y = 0.2D$ the downstream turbine data were not recorder at $t \approx 168\mathrm{s}$ and $t \approx 198\mathrm{s}$, thus explaining the large discrepancies there.
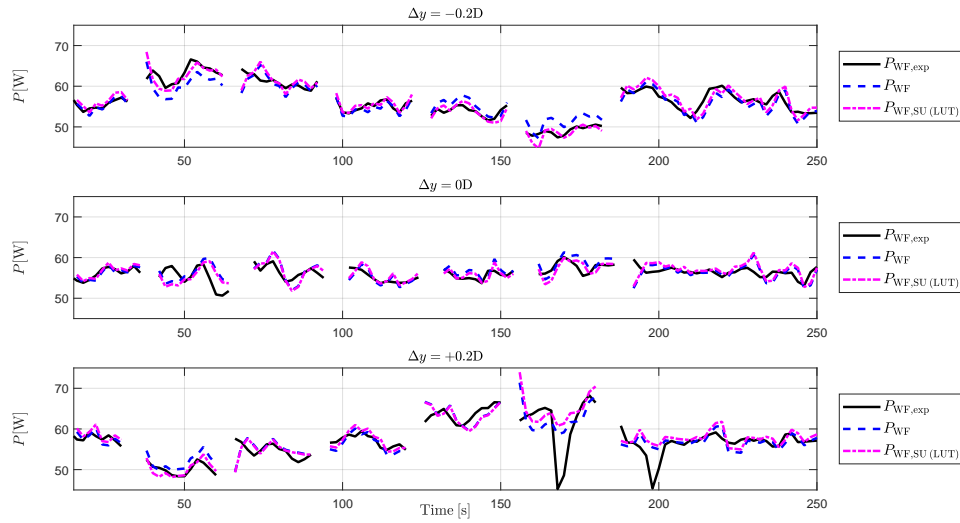
Figure 79. Baseline model (P_{WF}) and state update with look-up table predicted cluster power ($P_{\mathrm{WF,SU\ (LUT)}}$) compared to measured cluster power ($P_{\mathrm{WF,exp}}$) for the same experiments used to fill-up the look-up table.

However, in the given experimental campaign a very similar experiment with $\Delta y = 0D$ has been conducted allowing to check the look-up table on a different data set. The only difference is a slower yawing speed. The results displayed in Fig. 80 show that the learned state errors improve the wind farm power prediction slightly also in a case that has not been used for the identification of the look-up table.
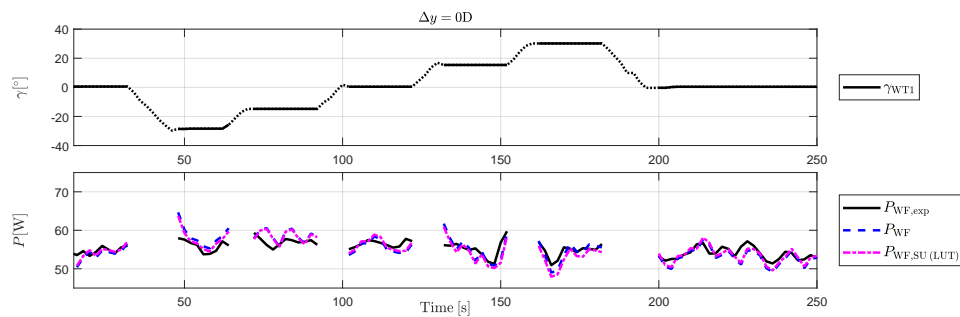
Figure 80. Baseline model (P_{WF}) and state update with look-up table predicted cluster power ($P_{\mathrm{WF,SU\ (LUT)}}$) compared to measured cluster power ($P_{\mathrm{WF,exp}}$) for a different set of experiments.

Further on, experiments have been conducted that combine a change in the upstream turbine yaw misalignment and the ambient wind speed V_{∞}. Again, applying the identified look-up table, it is shown in Fig.81 that the model predictions have been improved during most time. Clearly, some larger errors are still present due to the ambient wind speed fluctuation as well as to the fact the the upstream turbine were operating at above rated wind speed, i.e. a condition that differs from the ones used to fill-up the lookup tables.
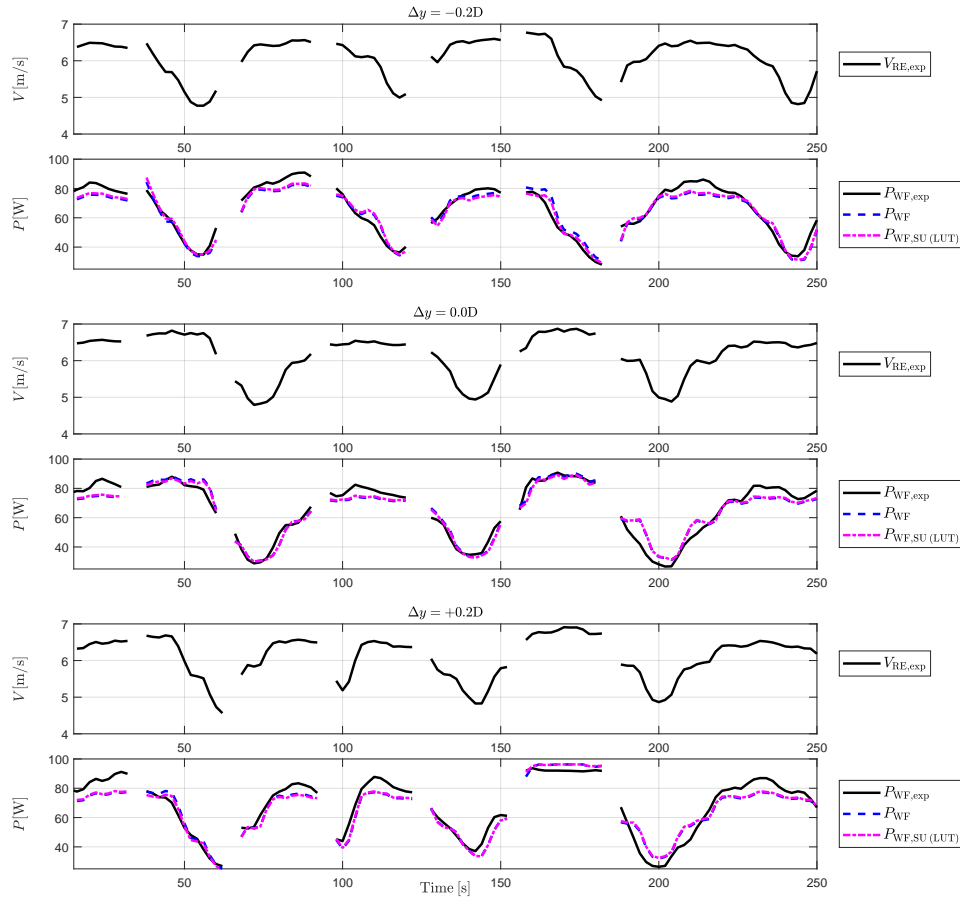
Figure 81. Baseline model (P_{WF}) and state update with look-up table predicted cluster power ($P_{\mathrm{WF,SU\ (LUT)}}$) compared to measured cluster power ($P_{\mathrm{WF,exp}}$) for a different set of experiments characterized by ambient wind speed fluctuations.

In this subsection, wake state errors have be learned in a set of experiments and then re-applied on different experiments. The results show improvements in the estimation of the wind farm power with respect to the baseline model.

6.4   Conclusions

Wind tunnel experiments have been successfully conducted testing the implementation of the state update method within the wind tunnel environment. The wind speed observer on each wind turbine was connected to a supervisory PC, which was running the state update method to estimate the model error on the upstream turbine's wake position and deficit.

Results suggest that an identified error in wake position and deficit for a given wind direction and upstream turbine yaw misalignment can only be partially assigned to other conditions. Improvements can only be observed for larger plant-model mismatches, that correspond in the shown examples

to lateral wake displacements of $\pm 0.2 \mathrm{D}$ or wrong ambient turbulence intensity inputs (8% instead of 5%) to the wind farm flow model. On the other hand, results show that even smaller model mismatches can be corrected in case the wake state errors are updated and stored for each configuration, i.e. different wind direction and upstream turbine yaw misalignment.

A future field application could therefore use a two stage approach: based on historic data that do not include wake steering, the baseline model can be updated with the identified wake state errors. In that first step, the wake state errors would be assumed to apply as well during yaw misalignment. In the second step, during wind farm operation, the wake state errors are continuously updated and stored for the given configuration leading to a continuously improving wind farm model and control actions. In coming wind farm control experiments, both approaches are planned to be tested.

7   VERIFICATION OF TECHNIQUES FOR FAST WAKE RECOVERY

7.1   Introduction

The interaction between wind turbines in a wind farm through their wake is a problem that is as old as wind farms itself. The wake of upstream turbines creates a wind field with a lower wind speed and a higher Turbulence Intensity (TI), resulting in a lower power production and higher relative loads for downstream turbines. In recent simulation studies [9, 10], dynamic induction control has shown promising results in improving power production in small to medium-sized wind farms. This approach, in short, dynamically varies the induction factor of the first upstream turbine of a wind farm. This creates a turbulent wind flow that enables wake recovery. Consequently, downstream turbines will compensate for the power loss of the upstream turbine, leading to a higher overall power production of the wind farm.

In [9], the optimal dynamic induction is found using a Model Predictive Control (MPC) approach. In [10], a simpler approach is suggested where the induction variation is limited to a sinusoidal signal. A grid search with different amplitudes and frequencies is performed to find the optimal dynamic signal. However, no experiments have yet been executed that validate this approach on actual, either scaled or full-sized, wind turbines. In this chapter, the dynamic induction control approach for wake recovery is evaluated in the Atmospheric Boundary Layer (ABL) wind tunnel of the Politecnico di Milano. The G1 models developed by the TU München, which have a rotor diameter of 1 m, will be used as turbine models. A small wind farm of three turbines, aligned with the wind direction, will be created in the wind tunnel.

To verify the validity of the dynamic induction approach for fast wake recovery in a wind farm, a number of wind tunnel experiments in both low and high Turbulence Intensity (TI) conditions are executed. The approach of [10] is used, where the excitation is limited to a sinusoidal signal. The effect of varying the amplitude and frequency of the signals is studied, and the performance of this approach is compared with the static greedy control approach.

Further experiments have been executed to study the possible benefits of different control signals, such as a block signal or an additional sinusoidal excitation on the second turbine. These experiments are unique in the sense that this has not been investigated before, neither in simulation nor in experiments. A positive result in these experiments would therefore be an important step towards proving the validity of this approach in real wind farms.

7.2   Verification of techniques for fast wake recovery

7.2.1   Testing environment

The experiments that will be described in this chapter will be executed in the low speed wind tunnel at Politecnico di Milano with an inflow velocity of approximately 5.5 m/s. The wind farm will consist

of 3 G1 turbine models placed in a row, with a lateral distance of $5D$. Each experiment will run for 240 seconds, which is equivalent to approximately 7 hours for a full-sized 10MW wind turbine. The performance of this approach will be evaluated both in a low Turbulence Intensity (TI) of 5% and in a high TI of 10%.

The power production of a wind turbine is proportional to the inflow velocity cubed. The inflow velocity in the wind tunnel is subject to small deviations, which can lead to significant deviations in the power production. This effect needs to be excluded from the results in order to enable a fair comparison between different experiments. This is done by determining the mean power coefficient $\bar{C}_p$. This coefficient is calculated as follows:

$$\bar{C}_{p,i} = \frac{P_i}{0.5\rho A(\bar{U}_\infty)^3} \tag{7.1}$$

with i the turbine index, P_i the total power produced by turbine i, ρ the air density, A the rotor area and $\bar{U}_\infty$ the mean inflow velocity as measured by the pitot tube in upstream of the first turbine. The target of the dynamic induction method is therefore to find the largest combined power coefficient for the 3-turbine wind farm.

7.2.2 Input signals

In [10], the control input C_T' is used. This signal relates to the thrust coefficient C_T through the following equation:

$$C_T = 1 - 4\left(\frac{C_T'}{4 + C_T'} - \frac{1}{2}\right)^2 \tag{7.2}$$

Since this relationship is not linear, a sinusoidal signal on C_T' does not result in a pure sinusoid on C_T. This is shown in Figure 82. However, preliminary simulations in PALM show that results with different input signals are very similar as long as the frequency is the same. These results are shown in Deliverable 3.3 of this report, which shows simulation results for the wake mixing strategy.

However, on the G1 turbine models, it is not possible to directly control the thrust coefficient. Alternatively, the fine pitch can be used to create a sinus-like signal on the thrust coefficient (Figure 82). Since PALM simulations show that the difference in output for these input signals is limited, this much better applicable approach is followed in the wind tunnel experiments.

Therefore, the fine pitch will be used to obtain a sinus-like dynamic thrust coefficient with the desired amplitude and offset. Since the internal torque controller of the G1 model is also active, the amplitudes and offsets of the pitch signals are tuned manually such that the resulting thrust coefficient matches the desired thrust coefficient in amplitude and phase. To achieve this, the thrust force on the turbine is measured which, together with knowledge about the wind conditions, is used to calculate the thrust coefficient over time.
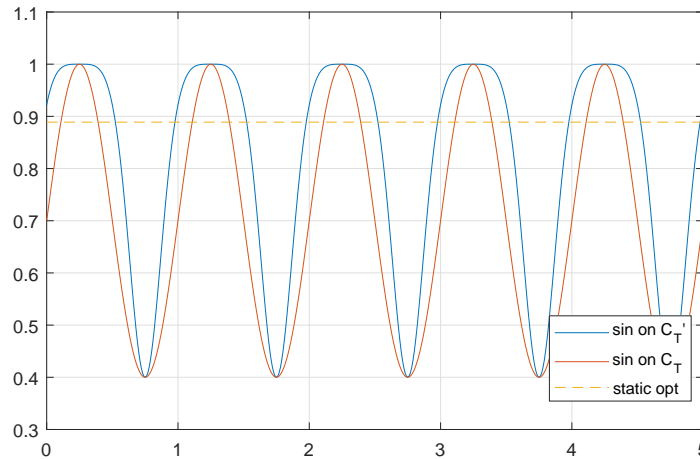
Figure 82. The values of C_T using a sine-like C_T' signal, compared to a sine on C_T. The dashed line shows the steady-state optimal C_T.

In the simulation studies (see Deliverable 3.3), different input signals have been evaluated: a sine on C_T', as well as a block wave on C_T (see Figure 82). In [10], it is shown that the amplitude and frequency of these signals determines the overall power production. In this paper, the optimum is found to be at a Strouhal number of $St = 0.25$. The dimensionless Strouhal number is defined as

$$St = \frac{fD}{U_\infty} \tag{7.3}$$

where f is the frequency, D the rotor diameter and U_∞ the inflow velocity of the wind. For the G1 models and an inflow velocity of 5.5 m/s, this Strouhal number would result in a frequency of 1.375 Hz. To validate these results, the interval from 0.5 to 2.3 Hz will be investigated in the wind tunnel.

In [10], four different amplitudes of C_T' are investigated: 0.5, 1, 1.5 and 2. Due to the limited time in the wind tunnel, the amplitude with the lowest power gain, $A = 0.5$ was not executed. Note that an amplitude of $C_T' = 2$ results in a thrust coefficient that varies from 0 to 1, *i.e.*, from the lowest to the highest possible thrust force. It is questionable whether this will be realizable in the wind tunnel. Therefore, it might be necessary to work with a slightly lower amplitude. Note that in the proceedings of this chapter, when the amplitude of the input signal is mentioned, it refers to the amplitude of C_T', unless stated otherwise.

Finally, [10] concludes in their simulation studies that a dynamic excitation of the second turbine in a 4-turbine farm yields disadvantageous results. These results will also be verified in the wind tunnel, albeit for a 3-turbine farm. Here, the influence of the phase delay between the excitation of both turbines will be investigated as well. In the following section, the results of the experiments executed with these input signals will be evaluated.

7.3   Results

In this sections, the results of the experiments that have been described above will be shown. The effect of changing the amplitude and the frequency of the sinus signals will be evaluated, and the overall power gain will be compared to static induction control.

7.3.1   Baseline control approach

To make a fair comparison with the state-of-the-art control methodology, baseline experiments have been conducted with static control approaches. The results of this experiments are shown in Figure 83.

Four experiments are shown here. In the first experiment (called *Baseline*), all turbines operate at their greedy optimum. For the G1 turbines, this means a collective pitch angle of 1.2°. The other three experiments are the result of an optimization done with the FLORIS model. Using FLORIS, the optimal settings for yaw, pitch and a combination of both is found, and these settings are implemented on the set-up.
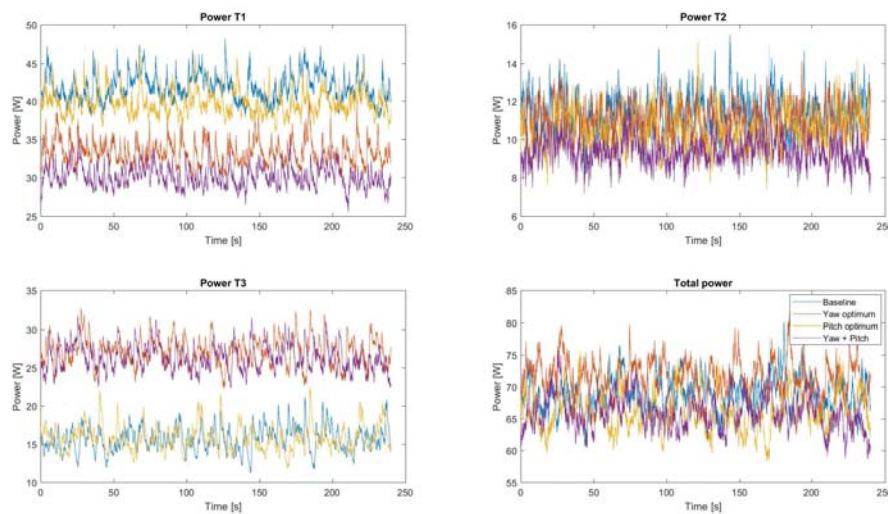
Figure 83. The power produced by all three turbines in different optimal static configurations. The bottom right figure shows the total power of the wind farm.

A thorough analysis of these results will be omitted here, it is important to note that the optimum found for static pitch control actually performs worse than the greedy control strategy. These settings lead to a decline of the total $\bar{C}_P$ (see Equation (7.1)) of 5.1%. The highest power production is accomplished using only yaw control, which yields an increase of $\bar{C}_P$ of 2.8%.

Since static induction control proves unable to increase the power production of the wind farm, the greedy control strategy will be used as baseline case for the dynamic induction approach.

Table 6. Optimal static settings found using FLORIS.

	Yaw angles [°]	Pitch angles [°]
Yaw control	[28.5 32 0]	[1.2 1.2 1.2]
Pitch control	[0 0 0]	[1.6 2 1.2]
Yaw and pitch control	[28.5 32 0]	[1.6 2 1.2]

7.3.2   Validating the input signals

As described in Section 7.2.2, the fine pitch angle is tuned manually for different experiments in order to match the desired thrust coefficients. In this section, the accuracy of this approach will be verified.
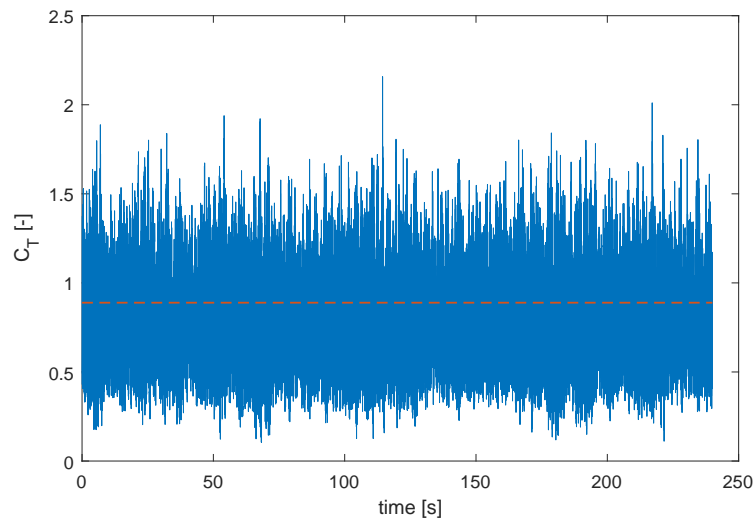
Figure 84. Measurements of thrust coefficient C_T over time for the baseline case. The dashed line shows the desired value of C_T.

Since the thrust coefficient C_T is determined using the tower fore-aft bending moment measurements, the resulting signal will show harmonics that are not caused by the varying pitch signal. An example is the eigenfrequency of the G1 model itself. It is therefore not trivial to determine the amplitude and frequency of C_T caused by the fine pitch variation. Figure 84 shows the measured C_T for the baseline case, *i.e.*, where no dynamic induction control is applied.

These oscillations at higher frequency can be clearly seen in the frequency spectrum of the thrust coefficient. Figure 85(a) shows this frequency spectrum for the sinusoidal measurement with amplitude $C_T' = 1.5$ and frequency $f = 1$ Hz. This spectrum shows a clear peak at the excited frequency, as would be expected, but also has additional peaks at approximately 15 and 35 Hz. These additional peaks cause the noisy signal that is observed in Figure 84.

Despite this high-frequent noise, it is still possible to distinguish the sinusoidal signal in this measurement. This is clearly visible in Figure 85(b), where a sine is fitted on the measurements of C_T.

(a)   *(b)*
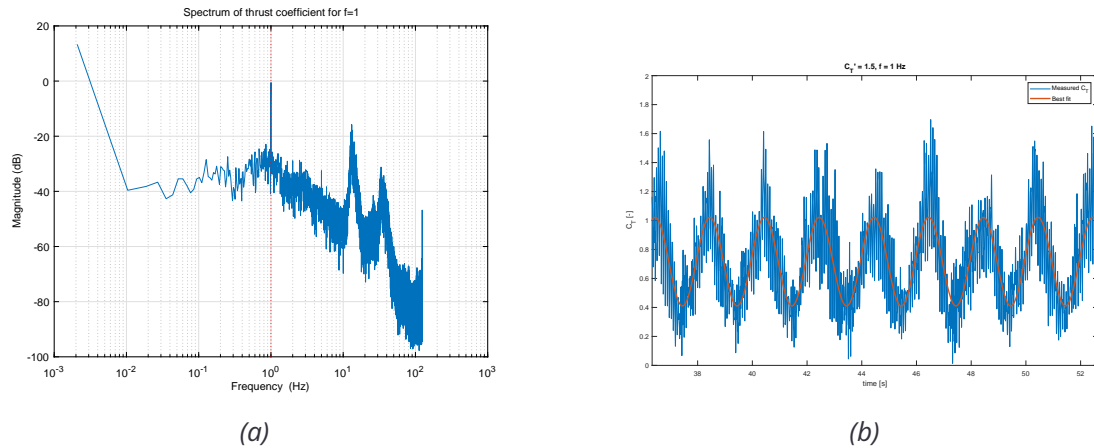
Figure 85. *(a) The frequency spectrum of C_T for the experiment with an amplitude of 1 and a frequency of 1 Hz; (b) The same signal in the time domain, including the best sinusoidal fit.*

By evaluating the amplitude and offset of these fits, it is possible to evaluate how well the desired excitation of C_T is achieved.
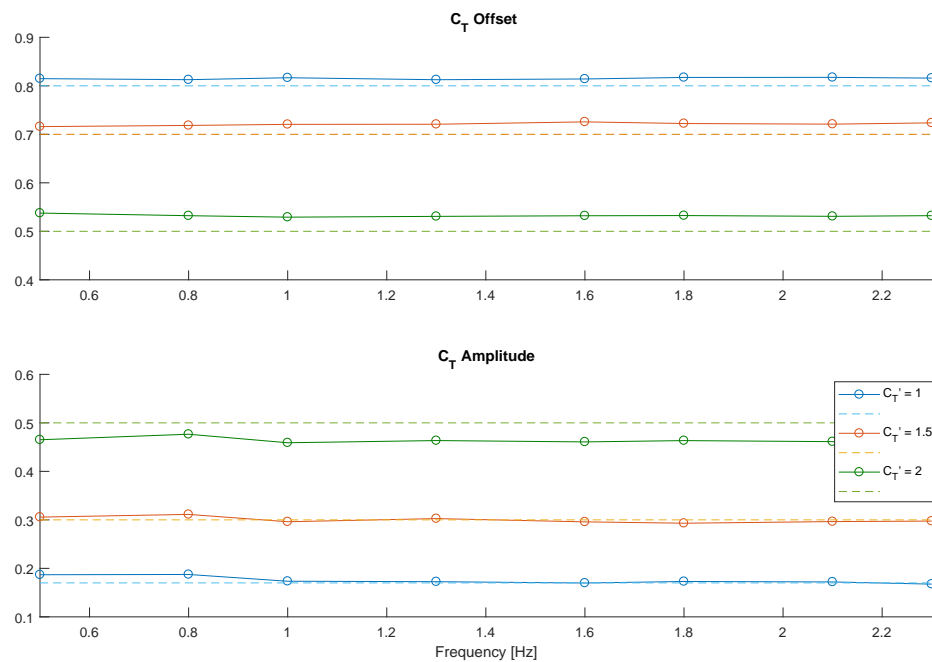
Figure 86. *The offsets and amplitudes of the fits of a sine on the C_T measurements in low TI. The dashed lines show the desired magnitude for the different experiments.*

Figure 86 shows the amplitudes and offsets of the fits on C_T for all different amplitudes and offsets in low turbulent conditions. This figure shows that the offset is slightly higher than expected for all experiments. However, the offset does appear to be constant for different frequencies. Therefore, this small bias is not expected to influence the effect of the frequency on the power production.

Looking at the bottom part of Figure 86, it can be seen that for the two low amplitude sets, the amplitude of C_T matches the desired amplitude very well. For the $C_T' = 2$ set, the amplitude is slightly lower. This was however expected, since this would require the thrust coefficient to go from 0 to 1 (the maximum) during each cycle. As it was not expected that this would be feasible, a slightly smaller amplitude was considered acceptable.
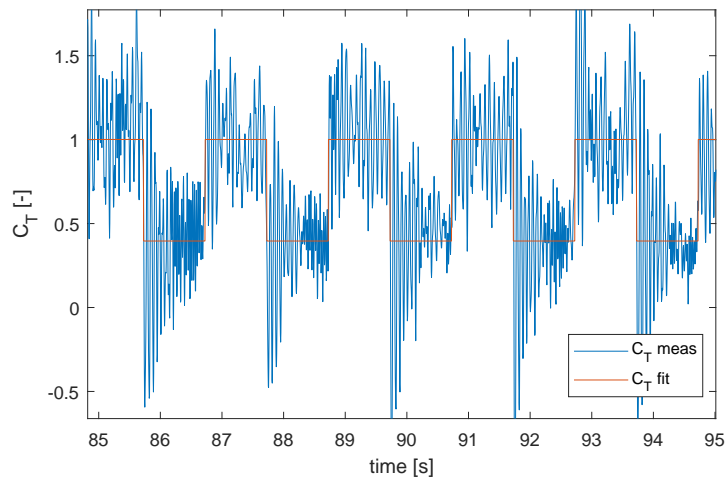
Figure 87. The measurements of the thrust coefficient when a block signal with amplitude $A = 1$ and a frequency $f = 1$ Hz is applied. In red is shown the best block signal fit for this measurement.

Next, the block input signals are evaluated. Figure 87 shows the measurement of C_T for one of these experiments, as well as the best fit for this signal. Notice that the peaks in C_T are significantly higher than with the smooth sinusoidal input. This could have a negative influence on the power production of this turbine, which will be evaluated in Section 7.3.4.

The best fit shown in Figure 87 has an offset of 0.698 and the amplitude of C_T is 0.302, where an offset of 0.7 and an amplitude of 0.3 was desired. It can therefore be concluded that the effective input signal matches the desired input signal very well.

7.3.3   Sinusoidal excitation

First, the results in the low turbulent wind (a TI of approximately 5%) are evaluated. In these conditions, 5 different sets of experiments have been conducted: three experiments with different amplitudes on a sinusoidal input, one with a block signal on the input and one where a sinusoid is put on both the first and the second turbine. In this last experiment, the phase difference between the two turbines is varied.

Figure 88 shows the mean power coefficients of the turbines and of the total wind farm. It can be seen here that increasing the amplitude of the sinus decreases the power coefficient of turbine 1, while it increases the power of turbine 2. However, for higher C_T', the loss at turbine 1 is too significant to compensate for by the downstream turbines. As a result, the case with the lowest
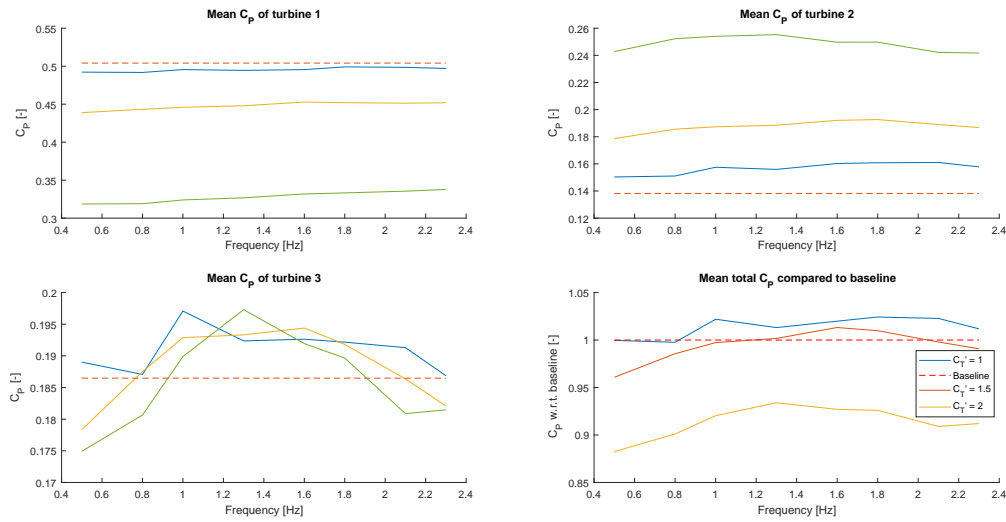
Figure 88. $\bar{C}_P$ **of the wind farm for different amplitudes of** C'_T**. The bottom right figure shows the total power conversion compared to the baseline case.**

amplitude proves to be the most effective. The highest increase in power extraction is found with $C'_T = 1$ and $f = 1.8\,\text{Hz}$, resulting in a 2.4% gain.
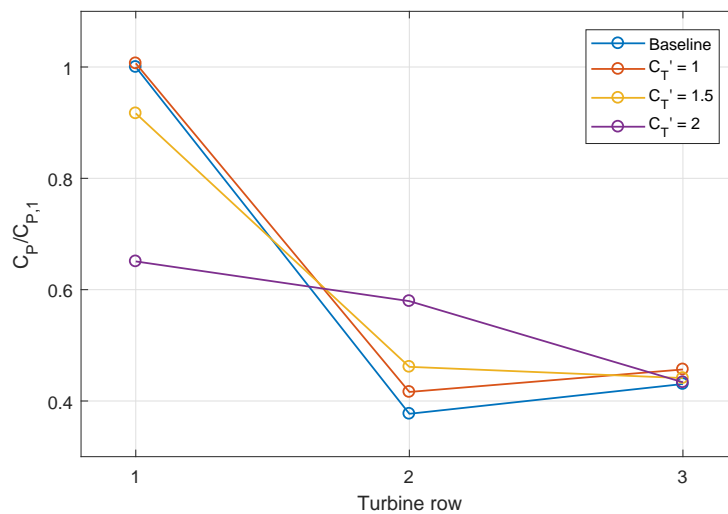
Figure 89. $\bar{C}_P$ **of each row scaled with the power of the first turbine in the baseline case. Shown are the 3 different amplitudes for the frequency with the highest power gain: 1.8 Hz.**

The results per row are shown in Figure 89 for the frequency of 1.8 Hz. As can be seen, the power production of the first turbine decreases significantly for higher turbines, while the power production of especially the first downstream turbine increases. However, the power gained at the second turbine is smaller than the power loss at the first turbine for the two biggest amplitude cases. Notice also that the power production of the third turbine in all three cases is very close to the baseline power production.

Table 7. An overview of the total power increase by applying dynamic induction control with different amplitudes (A, rows) and frequencies (columns) for the low turbulent experiments.

Frequency	0.5	0.8	1	1.3	1.6	1.8	2.1	2.3
Strouhal no.	0.09	0.15	0.18	0.24	0.29	0.33	0.38	0.42
$A = 1.0$	-0.04%	-0.24%	+2.20%	+1.30%	+1.6%	+2.4%	+2.3%	+1.2%
$A = 1.5$	-3.92%	-1.44%	-0.27%	+0.20%	+1.3%	+1.0%	-0.20%	-0.92%
$A = 2.0$	-11.76%	-9.89%	-7.97%	-6.61%	-7.30%	-7.41%	-9.09%	-8.80%

Table 7 gives an overview of the effect of different amplitudes and frequencies on the power production of the 3-turbine model wind farm. Note that the optimal frequency appears to decrease as the amplitude of the excitation increases.

Finally, the reliability of these results will be examined. To do this, the results are divided into four segments of 60 seconds. These shorter segments of measurements, still containing 15000 measurement points and between 30 (0.5 Hz) and 138 (2.3 Hz) sine cycles, will then be used to determine the variance of the measurements.
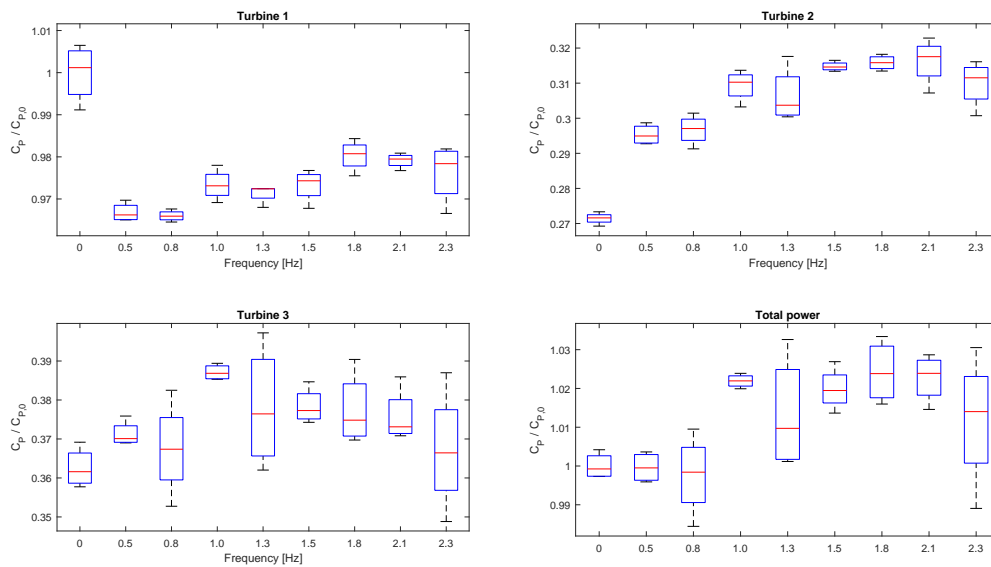
Figure 90. A boxplot showing the variance of the C_P measurements for the low turbulent, $A = 1$ experiments, for all turbines individually as well as for the entire wind farm. The $f = 0$ measurement represents the baseline case of no dynamic control.

Figure 90 shows a box plot of these data sets for $A = 1$, normalized by the steady state optimal C_P of turbine 1. This figure shows that the variance becomes larger at each downstream row due to the increased turbulence. As a result, the variance is significant in the total power production: up to $\pm 2\%$ of the power. However, this figure also shows that the variance is lower than the power gained by using dynamic induction control: the lowest values of the box plot around the optimal frequency of 1.8 Hz is still higher than the baseline value. This therefore shows that the power increase is significant, as this shows it is not a coincidental result of measurement errors.

The same experiments were executed in high turbulence intensity conditions. These results of all the amplitudes and frequencies that were studied are shown in Figure 91. The main conclusion that can be drawn from this figure, is that the effect of exciting the first turbine on the power production of this turbine is lower in these conditions. Due to the turbulence, the power production of this turbine is already slightly lower than in low TI conditions. As a result, the power loss at turbine 1 is negligible for the $A = 1$ case. As the power gain at the downstream turbines is similar, the total power gain at these conditions is 4%.
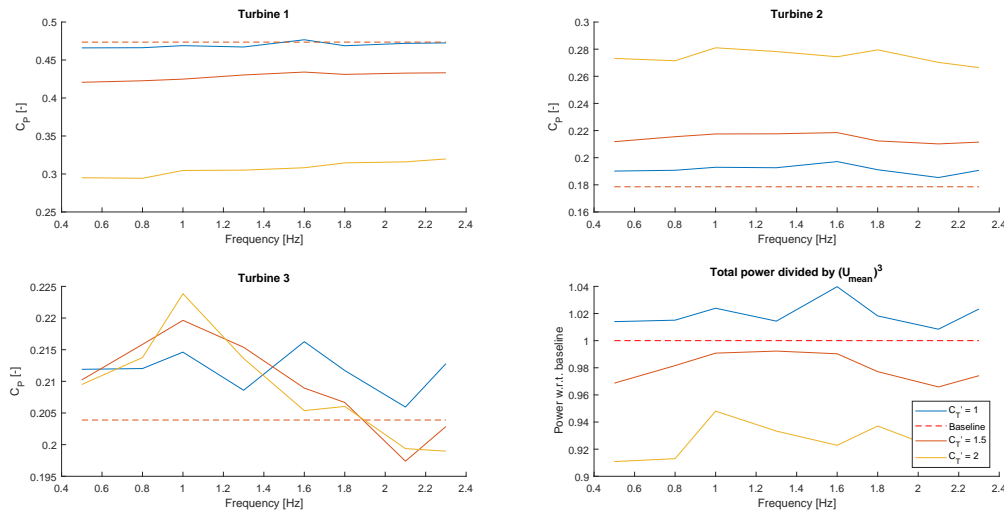
Figure 91. $\bar{C}_P$ **of the wind farm for different amplitudes of** C_T' **in the high TI conditions.
The bottom right figure shows the total power conversion compared to the baseline case.**

When the amplitude of the excitation is increased, the power loss at turbine 1 falls to a level comparable with the results in low TI conditions. However, since the power gain at turbine 3 is slightly lower, the total power is also lower than in the baseline case. Furthermore, it seems that the amplitude of the excitation is more important than the frequency in these conditions.

7.3.4   Block wave excitation

Next, the results of the experiments where a block wave was implemented on the fine pitch will be shown. A single amplitude of excitation was implemented, $A = 1$, with the same range of frequencies. As mentioned in Section 7.3.2, this input results in very high fluctuations of the thrust coefficient of the excited turbine, as shown in Figure 87. The effect of this is clearly visible in Figure 92: the first turbine produces significantly less than with a sinusoidal excitation, although the average collective pitch angle is identical.

Notice that the power gained at the downstream turbines is significantly higher with the block wave excitation. This indicates that the increased wake mixing indeed results in a higher effective wind speed for the downstream turbines. However, the greater power loss at turbine 1 results in a slightly
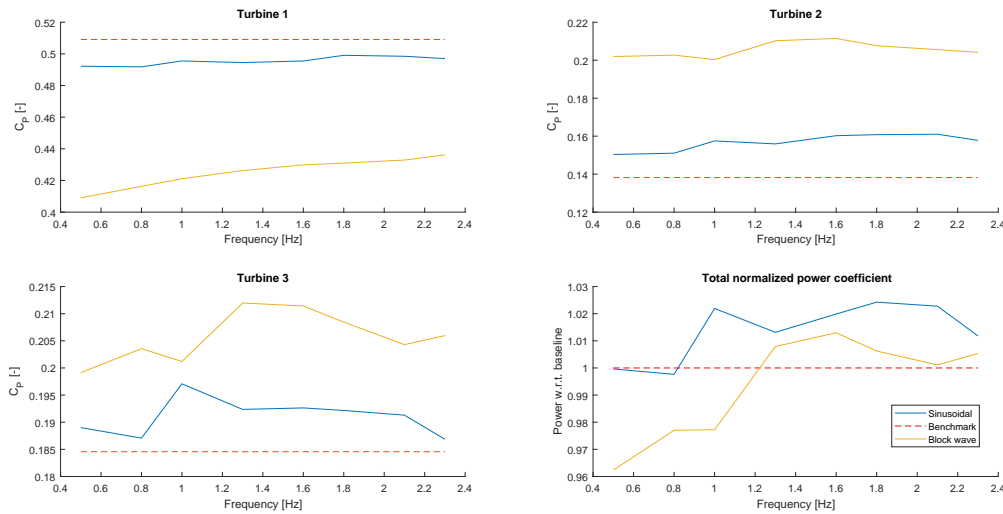
Figure 92. The power coefficient C_P of all turbines for both the sinusoidal and the block wave excitation of turbine 1, amplitude $A = 1$. The bottom right figure shows the combined power coefficient of the wind farm, normalized with the baseline controller.

lower overall power gain compared to the sinusoidal excitation. However, at the optimal frequency, 1.6 Hz, a power gain of 1.3 % is still obtained compared to the static optimum.

7.4   Excitation of turbine 2

In this section, dynamic induction control will be applied on both the first and the second turbine. A phase difference between both control signals will be applied, which will vary with steps of 30 degrees. The benefit of this approach is evaluated, as well as the effect of the phase delay.

Figure 93 shows the power production of this approach. The figure compares the performance for different phase delays compared to both the static baseline case and the optimal case found in Section 7.3.3. Unlike in the simulation studies of [10], exciting the second turbine does produce an addition power increase, as can be seen in the bottom right plot if Figure 93. The phase delay between the signals seems to have very little effect on the power production: the total power is roughly constant. The power gained with this approach is between 3 and 4 %, with a maximum of 4.0 % at a phase delay of 330 degrees.

Notice that this power gain seems to come from turbine 1 as much as from turbine 3. When the second turbine is excited, the first turbine quite surprisingly experiences an increase in power production. This indicates that there also exists some interaction from downstream to upstream turbines. Further research is needed to give insight in the fenomenon.
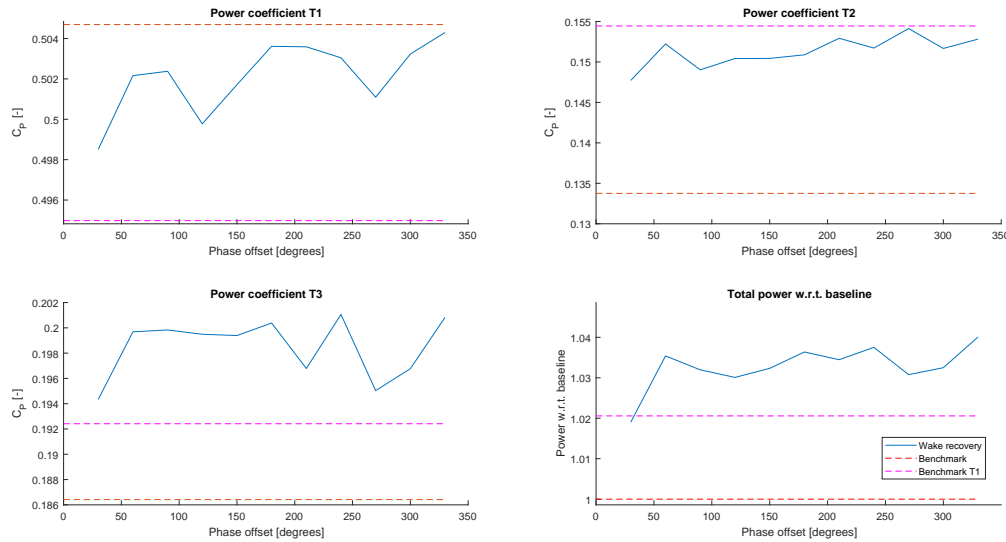
Figure 93. The power coefficient of all turbines when both turbine 1 and 2 are dynamically excited with an amplitude of $A = 1$ and a frequency of $f = 1.8$ Hz. Different phase delays between both turbines have been applied. The dashed lines show the baseline case of static control, as well as the optimal turbine 1 excitation case.

7.5   Conclusions

This chapter presents the results of unique wind tunnel experiments that demonstrate the potential of dynamic induction control in small wind farms. It has been shown that it is possible to increase the power production of a scaled 3-turbine wind farm by implementing this wake mixing approach.

This approach uses a dynamically varying thrust coefficient to enable better wake mixing. Due to this increased mixing, downstream turbines will be able to produce more power, compensating for the power loss at the first turbine. In these experiments, this varying input is limited to a sine with varying amplitude and frequency. It is shown that with the optimal settings, a power increase of 2.4 % in low turbulence intensity, and 4 % in high turbulence intensity can be achieved. These are significant gains, as static induction control has shown to be unable to increase the power production in this setup.

The experiments have shown the relevance of finding the optimal amplitude and frequency of the excitation. When suboptimal amplitudes and / or frequencies are used, the power production can easily decrease to values lower than the baseline case. This makes the development of an algorithm that is able to optimize these control parameters very relevant.

The highest power production was found at Strouhal numbers slightly lower than those found in the simulation studies of [10]. Also, where in [10] the optimal frequency was constant for different amplitudes, this was not the case in the wind tunnel experiments executed here (see Table 7). Furthermore, increasing the amplitude of the excitation had a bigger negative effect on the upstream

turbine than in these simulations. As a result, the optimal amplitude in the wind tunnel was significantly lower than in the simulation studies.

Another remarkable difference between simulation and wind tunnel experiments, is the effectiveness of exciting both the first and the second row of turbines. Where [10] concluded that this has a detrimental effect on the total power production, the wind tunnel experiments show a contradictionary result. The experiments showed that this approach can lead to an additional power gain compared to the approach of only exciting the first turbine.

Finally, a different input signal in the form of a block wave has also been examined in these experiments. This approach looked promising based on simulation experiments executed in Deliverable 3.3. However, in the wind tunnel, the high variations in thrust coefficient caused a significant power loss at the excited turbine, resulting in slightly less beneficial results: the power could still be increased with respect to the baseline case, up to 1.3%, but this gain was significantly lower than with the smooth sinusoidal excitation.

In all, it can be concluded that the dynamic induction control approach shows great promise, as now both simulations and scaled experiments show that it is possible to achieve a power gain. However, significant differences are found between simulation and experiments, which still need to be adressed. Future research can therefore be directed into clarifying these differences, as well as executing additional experiments.

As the amplitude and frequency of the excitation are shown to be important control parameters, it would be a very interesting challenge to develop an algorithm that is able to optimize these parameters. Furthermore, additional analysis on the increased loads on the turbines can be done to investigate the effect of these loads on the lifetime of turbines. Finally, application on full-scale wind turbines could be the last step in proving the validity of this approach.

8 VALIDATION OF A WIND STATE OBSERVER

8.1 Introduction

In this chapter, the wind tunnel validation of the so called *wind state observer* is discussed. This newly proposed methodology, described and validated by means of numerical simulations in deliverable 3.3, allows for the simultaneous estimation of both horizontal/vertical wind shears and yaw/tilt misalignments faced by a wind turbine during its operation and using, as inputs, the machine loads. A model is introduced to relate the one per revolution (1P) blade root bending moments to the inflow conditions, in order to collect useful information that can be exploited by the turbine/wind farm controller, for example, to increase power harvesting and reduce loads.

In section 8.2, the theory behind such observer is thoroughly explained. In addition, the rotational symmetry among the wind parameters is exploited to propose a simpler and more feasible identification of the model coefficients. In section 7.3, the wind tunnel set up is presented along with the results. Finally, in section 8.4 conclusions are drawn.

8.2 Wind state observer: formulation

8.2.1 Wind parametrization

The wind inflow is characterized in terms of four so called *wind states*, which are defined as the vertical (upflow) and horizontal (yaw) misalignment angles χ and ϕ, respectively, and the vertical and horizontal linear shears κ_v and κ_h, respectively. These quantities should be regarded as rotor-equivalent fits of the actual spatial distribution of the wind impinging on the rotor disk at a certain instant of time.

The wind states are defined with respect to a nacelle-attached reference frame $(\boldsymbol{x}, \boldsymbol{y}, \boldsymbol{z})$ centered at the hub, as shown in Fig. 94: unit vector $\boldsymbol{x}$ is aligned with the rotor axis and faces downwind, $\boldsymbol{z}$ points upward in the vertical plane, while $\boldsymbol{y}$ is defined according to the right hand rule. The components of the wind vector in the nacelle-attached frame of reference are noted $\boldsymbol{V} = \{u, v, w\}^T$ and they write

$$u(y, z) = W(y, z)\cos(\phi)\cos(\chi), \tag{8.1a}$$

$$v(y, z) = W(y, z)\sin(\phi)\cos(\chi), \tag{8.1b}$$

$$w(y, z) = W(y, z)\sin(\chi), \tag{8.1c}$$

where $W(y, z)$ is a linearly sheared wind field

$$W(y, z) = V_H\left(1 + \frac{z}{R}\kappa_v + \frac{y}{R}\kappa_h\right), \tag{8.2}$$

V_H being the wind speed at hub height, and R the rotor radius. According to this definition, the yaw misalignment and upflow angles are positive when the wind blows from the left and the lower part of the rotor, respectively, when looking upstream.
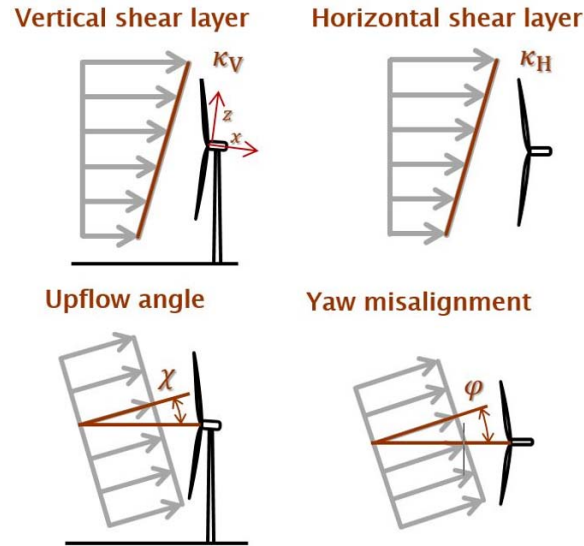
Figure 94. Definition of the four wind states used for parameterizing the wind field over the rotor disk.

Notice that in the present work the reference frame is aligned with the rotor axis. Together with the assumed linearity of both shears, this is necessary in order to exploit the rotational symmetry of the rotor response. Hence, if the rotor is up-tilted, one will have to transform the nacelle-frame wind components into a frame aligned with the ground, if necessary.

8.2.2   Wind observer formulation

In this work, the linear model of Cacciola, Bertelè, and Bottasso [6] and Bertelè et al. [2] is used to relate inflow conditions and machine response. The model writes

$$\boldsymbol{m} = \boldsymbol{F}(V, \rho)\boldsymbol{\theta} + \boldsymbol{m}_0(V, \rho) = [\boldsymbol{F}(V, \rho) \; \boldsymbol{m}_0(V, \rho)] \begin{bmatrix} \boldsymbol{\theta} \\ 1 \end{bmatrix} = \boldsymbol{T} \, \overline{\boldsymbol{\theta}}, \qquad (8.3)$$

where $\boldsymbol{m}$ is the load vector, $\boldsymbol{\theta} = \{\phi \; \kappa_v \; \chi \; \kappa_h\}^T$ is the wind state vector, while $\boldsymbol{F}$ and $\boldsymbol{m}_0$ represent the model coefficients, scheduled with respect to wind speed V and air density ρ. The load vector is defined as

$$\boldsymbol{m} = \{m_{1c}^{OP}, \; m_{1s}^{OP}, \; m_{1c}^{IP}, \; m_{1s}^{IP}\}^T, \qquad (8.4)$$

where m indicates the blade bending moment, subscripts $(\cdot)_{1s}$ and $(\cdot)_{1c}$ respectively indicate sine and cosine harmonics, while superscripts $(\cdot)^{OP}$ and $(\cdot)^{IP}$ respectively out- and in-plane components. The load harmonics are readily computed via the Coleman Feingold transformation [7], once three measured blade loads are available.

To identify the model coefficients $\boldsymbol{T}$, one should collect a rich enough data set for which both wind states $\boldsymbol{\theta}$ and associated blade loads $\boldsymbol{m}$ are known. Stacking side by side the ith wind and load vectors into matrices $\boldsymbol{\Theta}$ and $\boldsymbol{M}$, one gets

$$\boldsymbol{M} = \boldsymbol{T}\boldsymbol{\Theta}. \tag{8.5}$$

Finally, the model coefficients are readily identified as

$$\boldsymbol{T} = \boldsymbol{M}\boldsymbol{\Theta}^T(\boldsymbol{\Theta}\boldsymbol{\Theta}^T)^{-1}. \tag{8.6}$$

The invertibility of the system is discussed in Bertelè et al. [2]. Once the model has been identified, it can be used to compute estimated wind states $\boldsymbol{\theta}_{\mathrm{E}}$ given measured loads $\boldsymbol{m}_{\mathrm{M}}$:

$$\boldsymbol{\theta}_{\mathrm{E}} = \left(\boldsymbol{F}(V)^T\boldsymbol{R}^{-1}\boldsymbol{F}(V)\right)^{-1}\boldsymbol{F}(V)^T\boldsymbol{R}^{-1}(\boldsymbol{m}_{\mathrm{M}} - \boldsymbol{m}_0), \tag{8.7}$$

where $\boldsymbol{R}$ is the co-variance weighting matrix.

8.2.3 Rotationally symmetric identification

By considering the rotational symmetry of the rotor, the number of unknown coefficients in $\boldsymbol{F}$ can be reduced. Indeed, a vertical shear will cause the same response of an equivalent horizontal shear, delayed by $\pi/2$. The same consideration holds for a yaw misalignment and an equivalent upflow angle. This rotational symmetry is reflected in the derivatives of the loads with respect to the wind states, i.e. in the coefficients of matrix $\boldsymbol{F}$, by a rotation of $\pi/2$, $\sin(\psi + \pi/2) = \cos(\psi)$ and $\cos(\psi + \pi/2) = -\sin(\psi)$, where ψ is the azimuth angle. Considering further that ϕ is positive according to the right hand rule while χ is negative (cf. Fig. 94), the following conditions apply between pairs of model coefficients:

$$F_{i1} = \frac{\partial m_{1c}}{\partial \phi} = -\frac{\partial m_{1s}}{\partial \chi} = -F_{j3}, \tag{8.8a}$$

$$F_{j1} = \frac{\partial m_{1s}}{\partial \phi} = \frac{\partial m_{1c}}{\partial \chi} = F_{i3}, \tag{8.8b}$$

$$F_{i2} = \frac{\partial m_{1c}}{\partial \kappa_v} = \frac{\partial m_{1s}}{\partial \kappa_h} = F_{j4}, \tag{8.8c}$$

$$F_{j2} = \frac{\partial m_{1s}}{\partial \kappa_v} = -\frac{\partial m_{1c}}{\partial \kappa_h} = -F_{i4}, \tag{8.8d}$$

where $i = 1$ and $j = 2$ for the out-of-plane components, while $i = 3$ and $j = 4$ for the in-plane ones. This way, the unknown coefficients are reduced from 16 to 8.

The term $\boldsymbol{m}_0$ in Eq. (8.3) represents the effects of gravity on the loads [2]. Since this term is non-symmetric, no reduction of these coefficients is possible in this case.

The advantage of this approach is not only in the reduced number of unknown model coefficients, but, most importantly, in the reduced data points necessary for identification. In fact, by eliminating the coefficients of horizontal shear and upflow angle, one can use tests in which only yaw misalign-

ment angle and vertical shear are changing. Therefore, since the model is linear and depends on two parameters, a minimum of only four operating conditions is required for identification.

8.3   Results

8.3.1   Experimental Set up

To validate the rotational symmetric observer several tests were conducted in the wind tunnel of the Politecnico di Milano described in Deliverable 3.1. A scaled wind tunnel model, here named *G2* and also described in deliverable 3.1, was placed in the low speed section of the tunnel, under two different boundary layer conditions: a moderate and a higher turbulence intensity (TI) level, 3.8 and 8.5% respectively. Such configurations were obtained by changing the roughness elements on the floor and vortex generators at the chamber inlet. For sake of accuracy, such inflow conditions were mapped with hot-wire probes over the rotor swept area previous to the experiments, in order to obtain a mean reference inflow for the wind state observer. Fig. 95 shows the turbulence in the longitudinal direction for both turbulent set up.
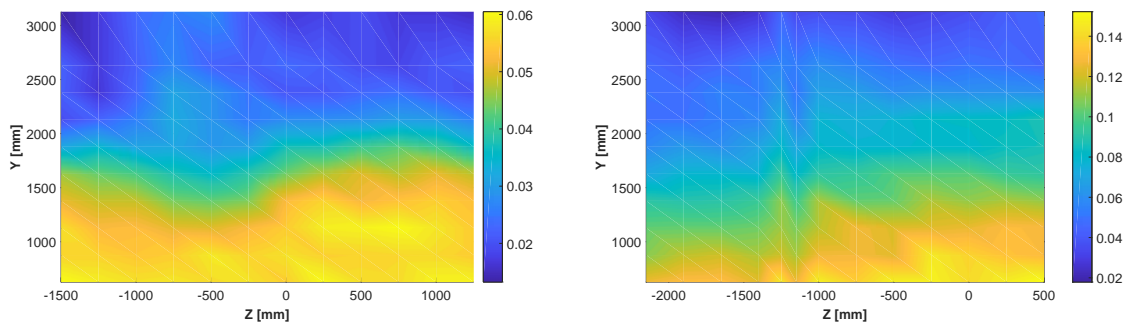
**Figure 95. Longitudinal TI over the rotor swept area for
the moderate (left) and high (right) turbulent set up.**

The G2, shown assembled in the Politecnico di Milano wind tunnel in Fig. 96, represents an aeroelastically scaled 3-bladed horizontal axis machine with a hub height of 1.7 m, a rotor diameter of 2 m and 6° of nacelle uptilt. Among other sensors, the machine is equipped with an optical incremental encoder which measures the blade azimuthal position and with strain gauges at the root of each blade, providing accurate measurements of the flap-wise and edge-wise blade root bending moments. In addition, a brushed motor coupled with an encoder guarantees a precise pitch angle actuation, allowing therefore for the calculation of in and out-of-plane blade root bending moments.

Several tests have been performed at different mean wind speeds in which the machine was yawed with respect to the wind. The table depicted in Fig. 97 shows the yaw configurations for each wind speed, and holds for both turbulence intensity levels. It follows that such tests allow for a change in mean vertical shear and yaw misalignment angle, whereas upflow and horizontal shear are consid-

Figure 96. G2 wind turbine scaled model within the wind tunnel of the Politecnico di Milano.

ered constant, i.e. +6° (given the machine uptilt) and null respectively. Nevertheless, to validate the rotational symmetry of the proposed observer, additional tests with changes in either mean horizontal shear or upflow were required. With this aim, the machine was mounted on top of a 6° inclined ramp: this allowed to perform, at 5.5 ms^{-1}, tests with changes in the mean upflow angle as well, ranging now from 0 up to 12°.

V [m/s]	Yaw demand [deg]								
	20	15	10	6	0	−6	−10	−15	−18
5	[x]		x		[x]	x			x
5.5	[x]		x		[x]	x			x
6		[x]	x	x	[x]	x	x	x	
7		[x]	x	x	[x]	x	x	x	
7.5		[x]		x	[x]	x		x	

Figure 97. Test matrix for both TI: the marked tests belong to the identification set.

The table depicted in Fig. 97 also shows which tests were used for identification, i.e. which tests were considered to compute the coefficients of the wind state observer. The choice of the identification set is completely arbitrary: in the present work, only the minimum amount of tests required per wind speed was considered, in order to simulate the harsher scenario, such as a field-based identification where not much data might be available. Since the proposed model is linear and its identification

only depends on two parameters, it follows that only 4 tests per wind speed are actually needed, making the identification set comprising of 20 out of the whole 64 available tests.

8.3.2   Wind tunnel results

For each available test, the mean blade root bending moments were computed averaging over the test time, i.e. 180 s. Fig. 98 shows the cosine 1P harmonic of both out and in-plane blade loads for changing yaw angle at 6 ms^{-1}. In accordance with what observed in a simulated environment, it appears that the loads change linearly with the yaw angle, and that each TI level causes a specific machine response. Similar conclusions, not shown here for the sake of brevity, can be drawn even for the sine harmonics and at different wind speeds: such results appear to validate the linear wind-load parameterization proposed in section 8.2.2.
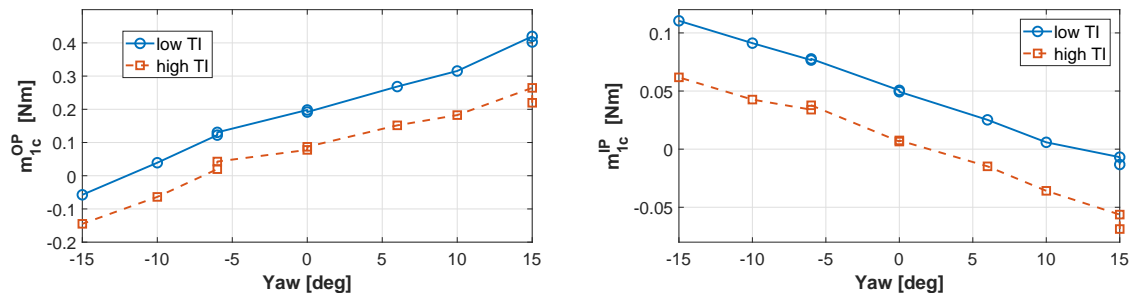
Figure 98. Out (left) and in-plane (right) 1P cosine of the blade root bending moments recorded at 6 ms^{-1} for low (solid) and high (dashed) TI with varying ϕ and $\chi = 6°$ and $\kappa_h = 0$.

To actually test the goodness of the proposed idea, the 1P blade harmonics were then fed into the previously identified wind state observer, and the corresponding mean wind field was estimated. Figure 99 and 100 show the estimation performance of yaw misalignment and vertical shear at 5 and 7.5 ms^{-1} respectively. On the x-axis the reference mean parameter is represented, whereas on the y-axis one finds the corresponding estimation: it follows that an ideal match would correspond to the bisector of the quadrant. The results clearly show that the proposed observer is capable of estimating both wind parameters. Indeed, at lower wind speeds only minor errors can be noted in the shear estimation, whereas the estimation of the wind direction appears almost perfect. With increasing wind speed, the estimation accuracy slightly decreases, leading to a maximum estimation error for the misalignment of about 2° and less than 0.02 for the shear.

Fig. 101 shows the observation of the yaw misalignment at an upflow of 12°, whereas on the right one can find the upflow angle estimation for a yaw angle of -6°, both at 5.5 ms^{-1}. These results validate the assumption of rotational symmetry of the parameters: indeed, here the estimations performed with upflow angles different from 6° are presented. Since the model identification was only based on tests with constant upflow angle, the model coefficients related to this parameter were obtained from the machine response to yaw misalignment, i.e. with Eq. 8.8. If the parameters are indeed rotationally symmetric, the proposed model should correctly estimate the wind inflow even
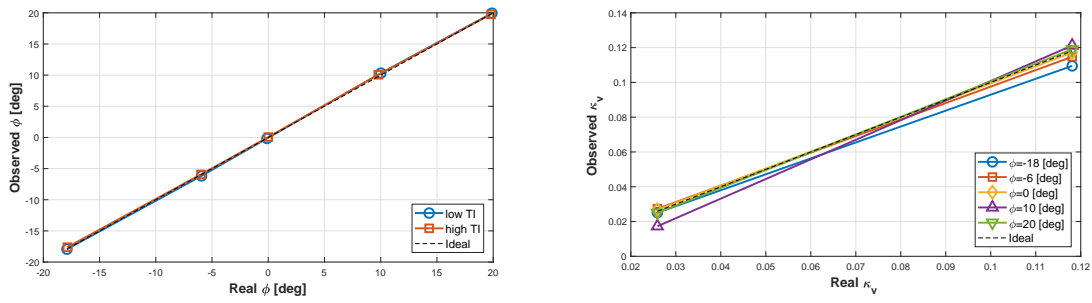
Figure 99. Observed and reference yaw misalignment (left) and vertical shear (right) for $\kappa_h = 0$ and $\chi = 6°$ at 5 ms^{-1}.
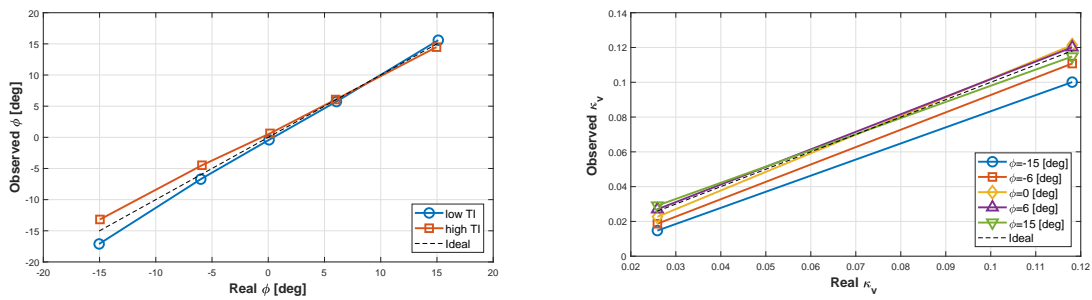
Figure 100. Observed and reference yaw misalignment (left) and vertical shear (right) for $\kappa_h = 0$ and $\chi = 6°$ at 7.5 ms^{-1}.

with non-constant upflow angle: the results are again quite accurate, with a maximum estimation error for both quantities of about 1.3°
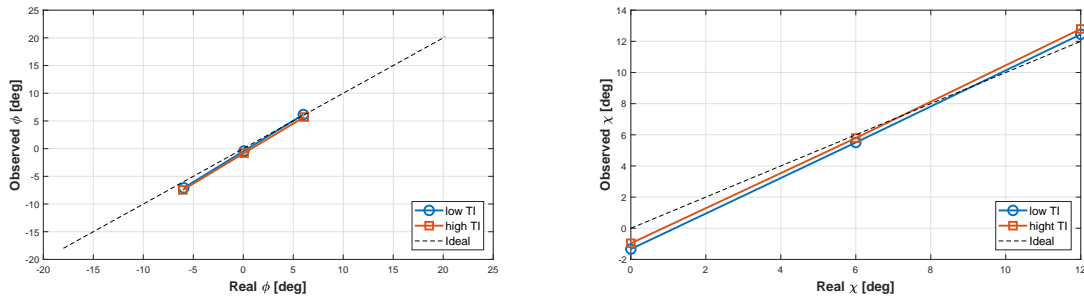
Figure 101. Observed and reference wind parameters at 5.5 ms^{-1} with $\kappa_h = 0$: yaw misalignment (left) for $\chi = 12°$ and upflow angle (right) for $\phi = -6°$.

Finally, in order to statistically quantify the observer performance, for each wind speed the mean estimation error was calculated averaging the single mean errors over the number of tests. Moreover, only the tests which were not included in the identification set were considered. The results are reported in Fig. 102. Again, it appears that the proposed wind state observer is capable of estimating all four parameters even considering different TI levels. The estimation of both shears appears to be very accurate, while the maximum mean error in the angle estimation is less than 1°.

Figure 102. Estimation mean error for each parameter as a function of the wind speed for low (solid) and high (dashed) TI: yaw angle (top left), vertical shear (top right), upflow angle (bottom left) and horizontal shear (bottom right).

8.3.3   Scheduled model

To test the rotationally symmetric observer even further, a new identification set was selected to exclude some wind speeds and quantify its performance if even less identification tests are available: the table depicted in Fig. 103 shows the chosen tests for both TI. Figure 104 reports the estimation error of the newly identified scheduled model. Obviously, no difference in performance with respect to Fig. 102 can be noted for the wind speeds included in the identification phase. Nevertheless, the performance tends to decrease for the remaining wind speeds. However, the maximum estimation error does not increase dramatically, and reaches a maximum of about 1.3 and 1.7° for horizontal and vertical misalignment respectively.

V [m/s]	Yaw demand [deg]								
	20	15	10	6	0	−6	−10	−15	−18
5	$\boxed{x}$		x		$\boxed{x}$	x			x
5.5	x		x		x	x			x
6		$\boxed{x}$	x	x	$\boxed{x}$	x	x	x	
7		x	x	x	x	x	x	x	
7.5		$\boxed{x}$		x	$\boxed{x}$	x		x	

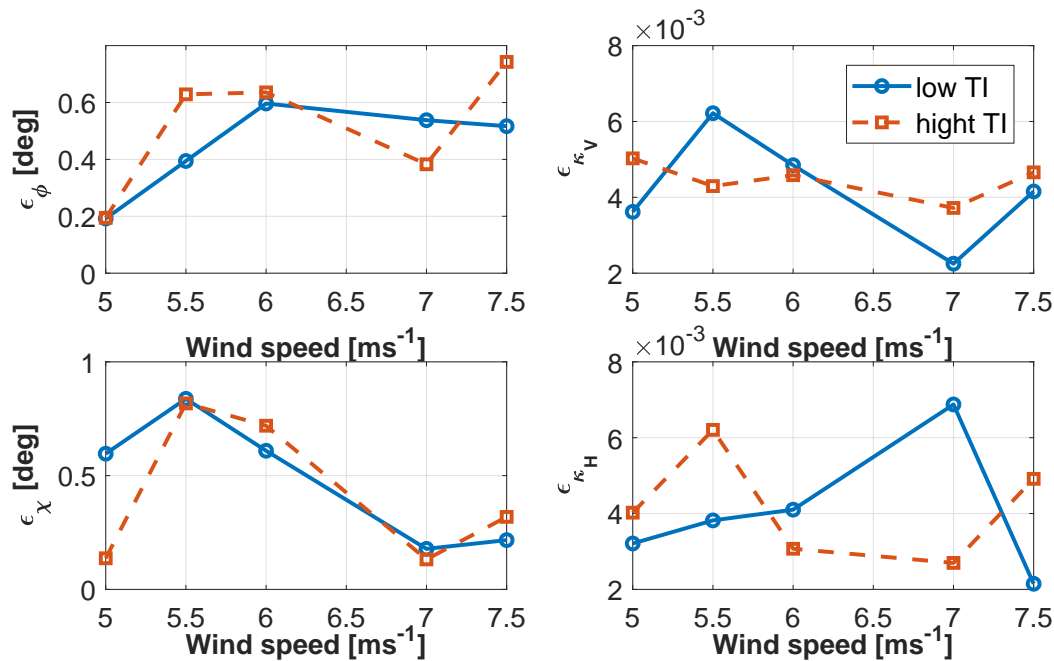**Figure 103. Test matrix for both TI: the marked tests belong to the identification set.**
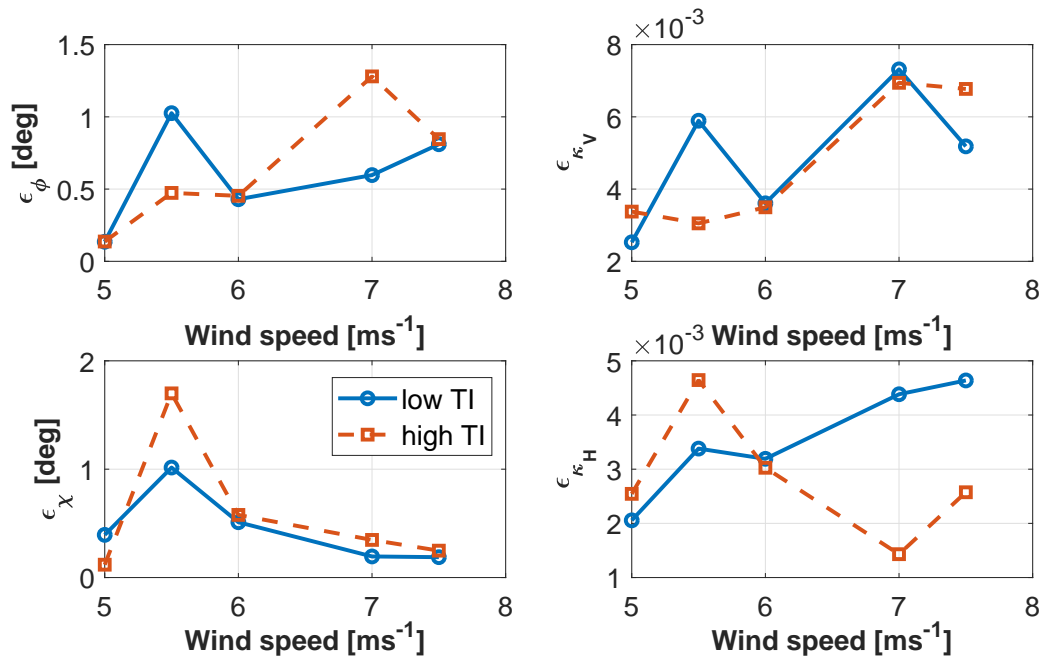
Figure 104. Estimation mean error for each parameter as a function of the wind speed for low (solid) and high (dashed) TI for the scheduled model: yaw angle (top left), vertical shear (top right), upflow angle (bottom left) and horizontal shear (bottom right).

8.4 Conclusions

In this chapter, the wind state observer described in deliverable 3.3 is further developed and validated with wind tunnel tests. Specifically, a new procedure was presented in order to simplify the model identification, drastically reducing the number of required tests. Such procedure was exploited in the wind tunnel to identify and directly use a wind state observer capable of estimating wind shears and misalignments starting from the measured 1P blade root bending loads. Tests were conducted at different wind speeds and turbulence intensity, (3.8 and 8.5% TI), varying both yaw angle and vertical shear while keeping upflow angle and horizontal shear constant. Additional tests, not included in the identification set but only used for validation, were performed placing the machine on a tilted ramp, therefore allowing for a change in upflow angle. From the presented results, the following conclusions can be drawn:

- The cosine and sine 1P harmonics of the out and in-plane blade root bending moments are indeed linearly dependent on the wind parameters. Each parameter leads to a specific variation in the machine response, allowing one to backward-estimate the proposed wind states.

- The assumption of rotational symmetry among the parameters, i.e. that the effect of an upflow angle is equivalent to the one of a similar yaw angle, only with a 90° phase delay, and the same holding for the shears, has been validated. Indeed, although only tests with constant upflow equal to 6° were used for the model identification, the model has been able to capture variations in the upflow angle.

- The wind observer is capable of accurately estimating the mean value of both shears and misalignment, no matter the turbulence levels. Indeed, the maximum mean error to be expected is less than 1° for both misalignments, and very low for both shears. These results were obtained using a model identified with the minimum amount of tests required for identification, thus in very harsh conditions.

- To simulate what could happen in the field, i.e. not a wide range of different wind speeds available in the dataset, an additional *scheduled* model was identified. Specifically, again four tests per wind speed were used for the identification, but now only 3 of the 5 wind speeds available were considered. The derived new model still proved to be capable of correctly estimating shears and misalignments, even at wind speeds which were not included in the identification set. The expected mean error slightly increases, but is nevertheless smaller than 1.7° for both misalignments. Such results suggest that the model can indeed be scheduled with respect to wind speed, or, in case of changes in density, dynamic pressure.

- The proposed and validated rotationally symmetric formulation allows one to drastically simplify the model identification: the minimum number of tests required is reduced to 4 per wind speed and, most importantly, the number of parameters the model depends on is reduced from 4 to two, i.e. one angle and one shear. This is fundamental for field-based identification, where parameters such as upflow and horizontal shear are not likely to change at a given site.

Further work will be performed to increase the robustness of the methodology whilst maintaining its simple approach. A Kalman filter will be applied to possibly improve the wind estimation, and the machine response will be further analyzed looking for other possible inputs to the formulation which could be more reliable and more easy to obtain than blade loads.

9   DELIVERABLE CONCLUSION

The wind tunnel testing activities performed in the first two years of the CL-Windcon project are the object of this deliverable. Hitherto, the experimentation has been focused on enabling supporting technologies for wind farm control and generating data to validate and tune simplified wake models. Closed-loop wind farm control will be part of a forthcoming deliverable (i.e. D3.6 Documentation of test campaigns).

From the experimentations already performed, the following conclusions can be derived:

- A detailed description of the flow within the wind tunnel of Politecnico di Milano was accomplished. The flow characterization mapped the speed and the turbulence intensity for different boundary layers at different tunnel longitudinal locations: 4 and 12 diameters upstream the position of the first turbine, at the inlet of the wind tunnel chamber and at each location where the the wind turbines are foreseen to be placed during further testing activities.

- The characteristics of the wake shed by a single wind turbine model and by a cluster of two wind turbine models were studied. The in-wake flow characterization considered a wide range of conditions, in terms of wind speed and turbulence intensity. The effects on the wake recovery, deficit and deflection of different wake control strategies, i.e de-rating and yawing out of the wind, were measured.

- The effect of IPC on both wake behavior and wind turbine loads was also considered. The effectiveness of IPC in reducing fixed-frame mean loads on wind turbines that are strongly misaligned with respect to the wind direction, or even partially impinged by the wake shed by an upstream wind turbine, has been proven experimentally. Moreover, it was assessed that the wake shed by a misaligned wind turbine is affected by IPC, a fact that could lead to modest increase, in order of few percent, of the downstream wind turbine power production.

- The capability of a wake state update method was tested. It was possible to prove the effectiveness of such algorithm to correctly identify and compensate wake model mismatches out of a suitable set of wind turbine measurements. It is expected that any wind farm controller may exploit the improved knowledge entailed by this wake state model update algorithm to optimize the total wind farm power output.

- An investigation on a fast wake recovery technique was accomplished. Thanks to experimentation, it was possible to verify that an increase of 4% and 2.4%, respectively for the high and low turbulence case, can be achieved in the case of three turbine wind farm layout.

- A wind inflow observer, able to estimate the wind states (i.e. yaw misalignment, upflow angle, vertical and horizontal shear layers) was tested. The observer proved effective in estimating the entire wind state. In particular, both shears can be estimated with high accuracy in a wide range of frequencies while the mean value of the yaw misalignment and upflow angle can be

captured with an error lower than 1 deg. It is expected that such improved knowledge of the yaw misalignment (and in general of the inflow) can be furthermore used in sophisticated wind farm control algorithms.

The data gathered in this first part of wind tunnel campaigns will be useful for a plethora of activities related to wind farm control. The obtained measurements will be used not only for the last part of the wind tunnel testing, related to closed-loop wind farm control, but also for other activities foreseen within the CL-Windcon project such as numerical-experimental comparison of wind farms and wind turbines dynamics, and tuning of wake models.

REFERENCES

[1]   M. Bastankhah and F. Porté-Agel. "Experimental and theoretical study of wind turbine wakes in yawed conditions." In: *Journal of Fluid Mechanics* 806 (2016), pp. 506–541.

[2]   M. Bertelè, C. L. Bottasso, S. Cacciola, F. Daher Adegas, and S. Delport. "Wind inflow observation from load harmonics." In: *Wind Energy Science* 2.2 (2017), pp. 615–640.

[3]   E. A. Bossanyi. "Individual blade pitch control for load reduction." In: *Wind Energy* 6.2 (2003), pp. 119–128.

[4]   C. L. Bottasso, F. Campagnolo, and V. Petrović. "Wind tunnel testing of scaled wind turbine models: Beyond aerodynamics." In: *Journal of wind engineering and industrial aerodynamics* 127 (2014), pp. 11–28.

[5]   T. Burton, N. Jenkins, D. Sharpe, and E. Bossanyi. "Aerodynamics of Horizontal Axis Wind Turbines." In: *Wind Energy Handbook*. John Wiley & Sons, Ltd, 2011, pp. 39–136. ISBN: 9781119992714.

[6]   S. Cacciola, M Bertelè, and C. L. Bottasso. "Simultaneous observation of wind shears and misalignments from rotor loads." In: *Journal of Physics: Conference Series*. Vol. 753. 5. IOP Publishing. 2016, p. 052002.

[7]   R. P. Coleman and A. M. Feingold. "Theory of self-excited mechanical oscillations of helicopter rotors with hinged blades. Technical Report, NACA TN 1351." In: (1957).

[8]   T. van Engelen. "Design Model and Load Reduction Assessment for Multi-rotational Mode Individual Pitch Control (Higher Harmonics Control)." In: *European Wind Energy Conference*. Athens, Greece, 2006.

[9]   W. Munters and J. Meyers. "An optimal control framework for dynamic induction control of wind farms and their interaction with the atmospheric boundary layer." In: *Phil. Trans. R. Soc. A* 375.2091 (2017), p. 20160100.

[10]   W. Munters and J. Meyers. "Towards practical dynamic induction control of wind farms: analysis of optimally controlled wind-farm boundary layers and sinusoidal induction control of first-row turbines." In: *Wind Energy Science* 3.1 (2018), pp. 409–425.

[11]   J. Wang, C. L. Bottasso, and F. Campagnolo. "Wake redirection: comparison of analytical, numerical and experimental models." In: *Journal of Physics: Conference Series*. Vol. 753. 3. IOP Publishing. 2016, p. 032064.